AD-A111 006 DREXEL UNIV PHILADELPHIA PA DEPT OF MECHANICAL ENGIN--ETC F/G 11/4
FRACTURE BEHAVIOR OF BORON ALUMINUM COMPOSITES AT ROOM AND ELEV--ETC(U)
SEP 80 J AWERBUCH AFOSR-79-0079

UNCLASSIFIED AFOSR-TR-82-0038 NL

1 OF 2
AD A
111006

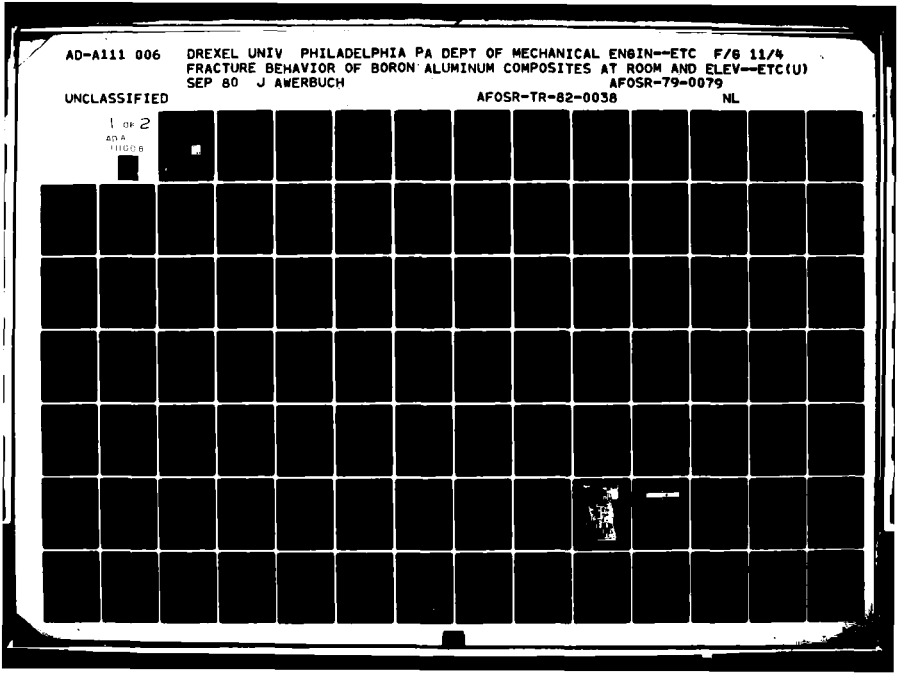

LEVEL II



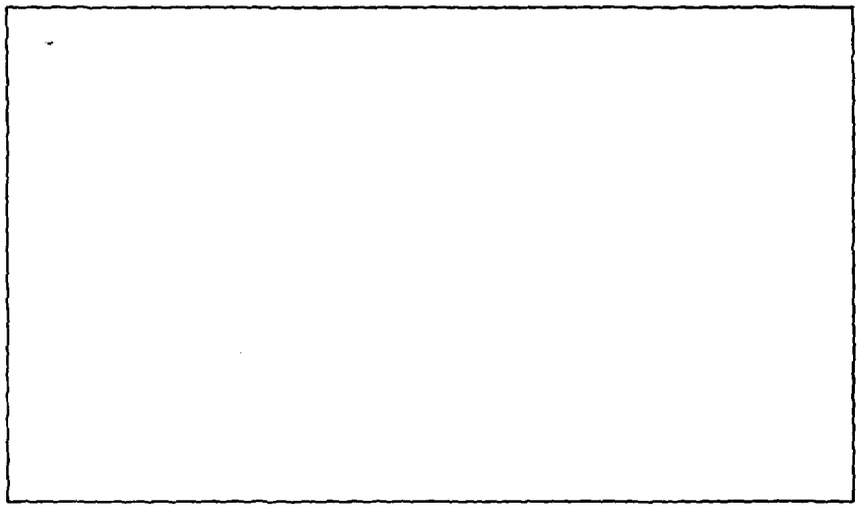

Drexel University

College of Engineering
Department of
Mechanical Engineering
and Mechanics
Philadelphia, PA 19104

(215) 895-2352-53

# FRACTURE BEHAVIOR OF BORON ALUMINUM COMPOSITES

# AT ROOM AND ELEVATED TEMPERATURES

PROGRESS REPORT

AFOSR 79-0079

PERIOD: APRIL 1, 1979 - MAY 31, 1980



Submitted by

Dr. Jonathan Awerbuch

Department of Mechanical Engineering and Mechanics
Drexel University
Philadelphia, PA 19104

UNCLASSIFIED

SECURITY CLASSIFICATION OF THIS PAGE (When Data Entered)

## REPORT DOCUMENTATION PAGE

READ INSTRUCTIONS BEFORE COMPLETING FORM

| | |
|---|---|
| 1 REPORT NUMBER: AFOSR-TR- 82-0038 | 2 GOVT ACCESSION NO.: AD-A111006 |
| 3 RECIPIENT'S CATALOG NUMBER | |
| 4 TITLE (and Subtitle): FRACTURE BEHAVIOR OF BORON ALUMINUM COMPOSITES AT ROOM AND ELEVATED TEMPERATURES | 5 TYPE OF REPORT & PERIOD COVERED: ANNUAL, 1 Apr 79 - 31 May 80 |
| | 6 PERFORMING ORG. REPORT NUMBER |
| 7 AUTHOR(s): JONATHAN AWERBUCH | 8 CONTRACT OR GRANT NUMBER(s): AFOSR 79-0079 |
| 9 PERFORMING ORGANIZATION NAME AND ADDRESS: DREXEL UNIVERSITY, DEPT OF MECHANICAL ENGR & MECHANICS, PHILADELPHIA, PA 19104 | 10 PROGRAM ELEMENT, PROJECT, TASK AREA & WORK UNIT NUMBERS: 61102F, 2307/B1 |
| 11 CONTROLLING OFFICE NAME AND ADDRESS: AIR FORCE OFFICE OF SCIENTIFIC RESEARCH/NA, BOLLING AIR FORCE BASE, DC 20332 | 12 REPORT DATE: September 1980 |
| | 13 NUMBER OF PAGES: 138 |
| 14 MONITORING AGENCY NAME & ADDRESS (if different from Controlling Office) | 15 SECURITY CLASS. (of this report): UNCLASSIFIED |
| | 15a DECLASSIFICATION DOWNGRADING SCHEDULE |

16 DISTRIBUTION STATEMENT (of this Report)

Approved for public release; distribution unlimited.

17 DISTRIBUTION STATEMENT (of the abstract entered in Block 20, if different from Report)

18 SUPPLEMENTARY NOTES

19 KEY WORDS (Continue on reverse side if necessary and identify by block number)

| | | |
|---|---|---|
| FRACTURE | ACOUSTIC EMISSION | FAILURE |
| BORON/ALUMINUM | COMPOSITE MATERIALS | FRACTOGRAPHY |
| FAILURE MODES | CRACK PROPAGATION | |
| NOTCH SENSITIVITY | NOTCHED STRENGTH | |
| FRACTURE STRENGTH | MECHANICAL PROPERTIES | |

20 ABSTRACT (Continue on reverse side if necessary and identify by block number)

This progress report describes the results of research work on the characterization of fracture behavior in boron/aluminum (B/Al) composites. Emphasis has been placed on the correlation between the observed failure modes and the deformation characteristics of center-notched B/Al composites, where particular attention has been given to the proper test procedure and analytical approach employed. The purpose of this work is not merely to generate and furnish quantitative data but also to discuss the appropriate methodology to be employed in characterizing a new composite material system. The investigation focused on the deformation

next page

DD FORM 1 JAN 73 1473 EDITION OF 1 NOV 65 IS OBSOLETE

UNCLASSIFIED

SECURITY CLASSIFICATION OF THIS PAGE (When Data Entered)

characteristics, crack tip damage growth, fracture strength and notch sensitivity and the associated characterization methods. Special attention has been given to nondestructive evaluation of internal damage and damage growth, techniques such as acoustic emission and X-ray radiography. Microstructural studies using scanning electron microscopy and photomicrography were employed as well. A description of all experimental procedures and techniques is given, e.g. mechanical and nondestructive testing, and a summary of representative results is presented. The report includes a comparison between the experimental results and several of the existing basic analytical approaches, a correlation between the various testing techniques, together with an assessment of the effect of the experimental technique on the characterization of failure.

## SUMMARY

This progress report describes the results of research work on the characterization of fracture behavior in boron/aluminum (B/Al) composites during the period April 1, 1979 to May 31, 1980. Emphasis has been placed on the correlation between the observed failure modes and the deformation characteristics of center-notched B/Al composites, where particular attention has been given to the proper test procedure and analytical approach employed.

The purpose of this work is not merely to generate and furnish quantitative data but also to discuss the appropriate methodology to be employed in characterizing a new composite material system. The investigation focused on the deformation characteristics, crack tip damage growth, fracture strength and notch sensitivity and the associated characterization methods. Special attention has also been given to nondestructive evaluation of internal damage and damage growth, techniques such as acoustic emission and X-ray radiography. Microstructural studies using scanning electron microscopy and photomicrography were employed as well.

A description of all experimental procedures and techniques is given, e.g. mechanical and nondestructive testing, and a summary of representative results is presented. The report includes a comparison between the experimental results and several of the existing basic analytical approaches, a correlation between the various testing techniques, together with an assessment of the effect of the experimental technique on the characterization of failure.

TABLE OF CONTENTS


| | | Page |
|---|---|---|
| SUMMARY | | i |
| I. | INTRODUCTION | 1 |
| | A. General | 1 |
| | B. Mechanical Behavior | 1 |
| | C. Fracture | 2 |
| | D. Objectives | 3 |
| II. | EXPERIMENTAL PROCEDURE | 5 |
| | A. Introduction | 5 |
| | B. Materials | 5 |
| | C. Laser Interferometric Displacement Gage (IDG) | 8 |
| | D. Compliance Gage | 10 |
| | E. Strain Gages | 11 |
| | F. Failure Modes | 13 |
| | G. Acoustic Emission | 13 |
| | H. X-ray Radiography | 13 |
| | I. Equipment Used | 14 |
| III. | ACOUSTIC EMISSION INSTRUMENTATION | 16 |
| | A. Introduction | 16 |
| | B. Instrumentation Capabilities | 17 |
| | C. Instrumentation | 19 |
| IV. | RESULTS AND ANALYSES | 20 |
| | A. Mechanical Properties | 20 |
| | B. Load-Crack Opening Displacement Curves | 20 |
| | C. Compliance Curves | 23 |
| | D. Elevated Temperature Load-COD Curves | 29 |
| | E. Fracture Strength | 30 |
| | F. Notch Sensitivity | 33 |
| | G. Acoustic Emission (AE) | 35 |
| | H. Failure Modes and Fracture Surfaces | 44 |
| | I. Elevated Temperature Tests | 47 |

Page

V. RESULTS AND CONCLUSIONS . . . . . 49

VI. RECOMMENDATIONS . . . . . 54

VII. RESEARCH PARTICIPANTS . . . . . 56

EXPENDITURE . . . . . 59

REFERENCES . . . . . 60

ILLUSTRATIONS (1-61) . . . . . .

LIST OF ILLUSTRATIONS


1. A general view of the testing facilities.

2. Photomicrograph of two indentations located at the center of the crack.

3. Schematic view of the laser interferometry displacement technique. Nominal value of d is 0.5 mm and $\alpha_o$ is typically 42°.

4. A schematic view of data reduction from the IDG records.

5. Block diagram of the Dunegan/Endevco 3000 acoustic emission system.

6. Schematics of location and amplitude distribution histograms and accumulative counts and events diagrams [920A Manual].

7. Schematics of pulse width distribution histograms, count rate and Cumulative Event Amplitude Distribution (CEAD) diagrams [920A Manual].

8. Stress-strain curves for $[0]_8$ and $[90]_8$ 5.6 mil B/Al-6061F.

9. Far-field load-displacement curves for unidirectional 5.6 mil B/Al-6061F specimens for various crack lengths obtained with the compliance gage.

10. Load-COD curves for unidirectional 5.6 mil B/Al-6061F specimens for various crack lengths obtained with the IDG.

11. Load-COD (loading-unloading) curves for unidirectional 5.6 mil B/Al-6061F specimens obtained with IDG (crack length = 7.56 mm).

12. Far-field load-displacement curves for $[90]_8$ 5.6 mil B/Al-6061F specimens for various crack lengths obtained with the compliance gage.

13. Load-COD curves for $[90]_8$ 5.6 mil B/Al-6061F specimens for various crack lengths obtained with the IDG.

14. Detail of far-field load-displacement curve for $[90]_8$ 5.6 mil B/Al-6061F obtained with the compliance gage (crack length = 12.94 mm).

15. Example of three load-COD curves at initial loading for unidirectional 5.6 mil B/Al-6061F specimens obtained with the IDG (crack length = 7.56 mm).

16. Global compliance versus crack length for unidirectional 5.6 mil B/Al-6061F .

17. Global compliance versus crack length for $[90]_8$ 5.6 mil B/Al-6061F .

18. Local compliance versus crack length for unidirectional 5.6 mil B/Al-6061F .

19. Local compliance versus crack length for $[90]_8$ 5.6 mil B/Al-6061F .

20. Comparison of experimental K-calibration factors with theoretical isotropic curve for unidirectional 5.6 mil B/Al-6061F .

21. Load-COD curves for unidirectional 5.6 mil B/Al-6061F at various temperatures, obtained with the IDG (crack length ≈ 7.60 mm) .

22. Initial load-COD curves for unidirectional 5.6 mil B/Al-6061F at various temperatures, obtained with the IDG (crack length ≈ 7.60 mm) .

23. Comparison of initial load-COD curves for unidirectional 5.6 mil B/Al-6061F at 21°C and 316°C, obtained with the IDG (crack length = 7.50 mm) .

24. Least squares fit for $c_o$ for unidirectional 5.6 mil B/Al-6061F.

25. Comparison of analytical (WEK model) and experimental results on notched strength for unidirectional 5.6 mil B/Al-6061F .

26. Notched strength versus crack length: comparison of ML model with experimental results for unidirectional 5.6 mil B/Al-6061F .

27. Notched strength versus crack length: comparison of WEK model with experimental results on logarithmic scale for unidirectional 5.6 mil B/Al-6061F .

28. Location distribution histograms for notched unidirectional 5.6 mil B/Al-6061F specimen at various load levels (crack length = 12.90 mm) .

29. Amplitude distribution histograms for unnotched unidirectional 5.6 mil B/Al-6061F specimen at various load levels (crack length = 12.90 mm) .

30. Cumulative Event Amplitude Distributions for nothced unidirectional 5.6 mil B/Al-6061 specimen at various load levels (crack length = 12.90 mm).

31. Location distribution histograms (in linear and logarithmic scales) for notched unidirectional 5.6 mil B/Al-6061F specimen after failure (crack length = 12.90 mm) .

32. Amplitude distribution histograms (in linear and logarithmic scales for notched unidirectional 5.6 mil B/Al-6061F specimen after failure (crack length = 12.90 mm) .

33. Location distribution histograms (in linear and logarithmic scales) for notched unidirectional 5.6 mil B/Al-6061F specimen loaded to 40% of expected ultimate load (crack length = 7.64 mm) .

34. Amplitude distribution histograms and Cumulative Event Amplitude Distribution for notched unidirectional 5.6 mil B/Al-6061F specimen loaded to 40% of expected ultimate load (crack length = 7.64 mm) .

35. Scanning electron microscope photographs of broken fibers at crack tip (after dissolving aluminum matrix) for unidirectional 5.6 mil B/Al-6061F specimen loaded to 40% of expected ultimate load (crack length = 7.64 mm): a. crack tip damage, broken fiber seen in third layer; b. detail of broken fiber.

36. Location distribution histograms for notched unidirectional 5.6 mil B/Al-6061F specimen at various load levels, clamped with sanding paper (crack length = 10.69 mm) .

37. Amplitude distribution histograms for notched unidirectional 5.6 mil B/Al-6061F specimen at various load levels, clamped with sanding paper (crack length = 10.69 mm) .

38. Cumulative Event Amplitude Distributions for notched unidirectional 5.6 mil B/Al-6061F specimen at various load-levels,clamped with sanding paper (crack length = 10.69 mm).

39. Location distribution histograms (in linear and logarithmic scales) for unnotched unidirectional 5.6 mil B/Al-6061F specimen after failure .

40. Amplitude distribution histograms (in linear and logarithmic scales) and Cumulative Event Amplitude Distribution for unnotched unidirectional 5.6 mil B/Al-6061F specimen after failure.

41. Cumulative Event Amplitude Distribution for unnotched unidirectional 5.6 mil B/Al-6061F specimen at various load levels .

42. Far-field load-displacement curve and accumulative events and counts as a function of load for notched unidirectional 5.6 mil B/Al-6061F specimen (crack length = 7.70 mm) .

43. Far-field load-displacement curve and count rate (per 1.0 second) as a function of load for notched unidirectional B/Al-6061F specimen (crack length = 7.70 mm) .

44. Accumulative counts per events for notched unidirectional 5.6 mil B/Al-6061F (crack length = 7.70 mm).

45. Location distribution histograms (in linear and logarithmic scales) for notched unidirectional 5.6 mil B/Al-6061F specimen after failure (crack length = 7.70 mm) .

46. Amplitude distribution histograms (in linear and logarithmic scales) for notched unidirectional 5.6 mil B/Al-6061F specimen after failure (crack length = 7.70 mm) .

47. Location distribution histograms (in linear and logarithmic scales for notched $[90]_8$ 5.6 mil B/Al-6061F specimens after failure (crack length = 7.63 mm) .

48. Amplitude distribution histograms (in linear and logarithmic scales) and Cumulative Event Amplitude Distribution for notched $[90]_8$ 5.6 mil B/Al-6061F specimens after failure (crack length = 7.63 mm) .

49. Far-field load-displacement curve and accumulative events and counts as a function of load for notched $[90]_8$ 5.6 mil B/Al-6061F specimen (crack length = 7.63 mm).

50. Far-field load-displacement curve and count rate (per 1.0 second) as a function of load for notched $[90]_8$ 5.6 mil B/Al-6061F speciemn (crack length = 7.63 mm) .

51. Accumulative counts per events for notched $[90]_8$ 5.6 mil B/Al-6061F specimen (crack length = 7.63 mm) .

52. Accumulative counts as a function of load during loading/unloading cycles for unidirectional 5.6 mil B/Al-6061F (crack length = 10.19 mm).

53. Accumulative number of events as a function of load for unnotched and notched unidirectional 5.6 mil B/Al-6061F specimens. Effect of clamping method and length of pre-set "window" is also shown .

54. Accumulative number of events as a function of percent of ultimate strength for notched and unnotched unidirectional 5.6 mil B/Al-6061F specimens .

55. Photographs of fracture specimens for: a. $[0]_8$ and b. $[90]_8$ notched and unnotched specimens.

56. Photomicrographs of unidirectional 5.6 mil B/Al-6061F specimen .

57. Scanning electron microscope micrographs of fracture surface. a. A stereo pair; b. General view of part of the fracture surface. (Ultimate strength = 1303 MPa.)

58. Scanning electron microscope micrographs of fracture surface. a. General view; b. Individual fiber for X-ray examination of fiber surface. (Ultimate strength = 1469 MPa.)

59. X-ray examination of fiber surface shown in Figure 58b using an energy dispersive X-ray analyzer on the SEM.

60. Crack tip damage in unnotched unidirectional 5.6 mil B/Al-6061F specimen after loading to 40% of expected ultimate load (crack length = 7.64 mm). a. General view; b. Detail of crack tip damage.

61. Scanning electron microscope micrographs of fracture surface of $[90]_8$ 5.6 mil B/Al-6061F. a. Unnotched specimen; b. Notched specimen (crack length = 7.62 mm).

LIST OF TABLES


| Table | | Page |
|---|---|---|
| I | List of Number of Specimens . . . . . | 7 |
| II | Mechanical Properties . . . . . | 21 |
| III | Experimental Values of Local ($C_\ell$) and Global ($C_g$) Compliance for 5.6 mil Boron/Aluminum-6061F . . . . . | 25 |
| IV | Notched Strength Data for 5.6 mil Boron/Aluminum-6061F. . . . | 31 |
| V | Notch Sensitivity . . . . . | 34 |

# I. INTRODUCTION

A. General - The mechanical behavior of advanced composite materials is heavily dependent upon the influence of environmental factors such as temperature, moisture, and load history. Metal matrix composites do demonstrate certain advantages over resin matrix composites, having larger operating temperature ranges, higher strength, better transverse and shear properties, better impact resistance, and no exposure to the potential problem of moisture absorption, to name only the most significant. Metal matrix composites have not been studied as intensively as resin matrix composites, and their applications were not as numerous, mainly because of cost effectiveness. However, recent advances in manufacturing-fabrication methods and technology of metal matrix composites, particularly boron/aluminum composites, e.g. [1,2,3], coupled with the recognized advantages in their mechanical properties, e.g. [2], make these materials increasingly strong candidates for future applications in aircraft and aerospace structures. Boron/Aluminum composites are now being considered for numerous applications, such as jet engine fan blades, landing gears, transmission housing, other aircraft structures, missiles,and aerospace vehicles. Additional applications are listed in Ref. [2]. In short, metal matrix composites are chosen when a combination of high strength, high stiffness, light weight, and high operating temperatures is required.

B. Mechanical Behavior - Boron/aluminum composites have received most of the attention, among a variety of metal matrix composites, in the research activity and applications studies of recent years. The mechanical behavior has been studied extensively and results published in many reports and publications. Data on the axial and transverse tensile properties of boron/aluminum composites using different matrix alloys, different temper conditions and fibers are given in [4,5]. Tensile, fatigue, creep, and stress-rupture behavior of uniaxial

and biaxial laminates at different temperatures are given in [6,7]. Fatigue behavior and failure mechanisms have also been studied [8] as well as the non-linear behavior in tension and compression of different laminates [9,10]. This is only a sample of the numerous studies and publications in which the various parameters influencing the mechanical behavior of boron/aluminum composites were investigated, all of which provide a good understanding of the behavior and potential application of these materials.

C. Fracture - A subject of extreme concern is the fracture behavior of B/Al composites which exhibit extremely low elongation up to fracture, and several studies have addressed this issue [11-17]. The applicability of linear elastic fracture mechanics (LEFM) to unidirectional B/Al has been discussed [11-13] with varying conclusions. For example, Kreider and Dardi [11], and Mar [12] concluded that the correlation between fracture strength $\sigma_f$ and half crack length a is best described by an equation of the form $\sigma_f a^m$ = const. However, contrary to LEFM predictions, the exponent m was found to be less than one half. Wright [13] concluded that LEFM can be applied, provided that the crack extension prior to failure is added to the initial crack length. With this assumption, the data of [13] as well as [11] agree with predictions based on LEFM. This assumption follows, in fact, the analytical models proposed in [14,15] for notched strength predictions of composites. Hancock and Swanson [16] concluded that the conventional concepts of fracture toughness can be useful in characterizing the toughness of unidirectional B/Al. Sun and Prewo [17] showed that the fracture toughness of B/Al can be described by LEFM provided the crack extension is colinear with the initial pre-machined notch, as is the case for [90°] or [0°/90°] laminates of compact tension specimen geometry. For unidirectional B/Al, such an approach is not relevant [17] due to the large amount of plastic deformation of the matrix parallel to the filaments. Similar damage growth and

modes of failure under static and fatigue loadings have been observed and discussed in [11,18,19,20]. In general, it has been shown that the failure of unidirectional B/Al is preceded by longitudinal plastic deformation at the crack tip which eventually leads to matrix cracking and crack tip blunting, all of which contribute to the crack arresting mechanism. The incipient matrix cracking has been described by the elastic stress intensity factor [18]. Obviously when different analytical approaches and experimental techniques are employed to define fracture toughness, the resulting toughness values vary significantly. Nevertheless, the majority of the values are still very promising in comparison with other metal or resin matrix composites.

With regard to mechanical properties, attention has been directed primarily toward unidirectional 5.6 mil B/Al-6061F. However with the more demanding requirements for toughness, recent attention has been given to other material systems, e.g. unidirectional 8.0 mil B/Al-1100F, primarily for jet engine fan blade applications. For such applications, better impact resistant and less notch sensitive material systems are being sought. Charpy test results [21-23] have shown that 8.0 mil B/Al-1100F does demonstrate certain advantages over the more common 5.6 mil B/Al-6061F. The choice of low shear strength matrices such as 1100 aluminum combined with high strength fibers provides a material system capable of dissipating high levels of energy upon impact loading [21]. Limited studies have also been directed toward the use of B/Al laminates [21-23].

D. Objectives - The bulk of the research on B/Al composites has explored the mechanical behavior, notch sensitivity, fracture behavior and failure modes at room temperature. Very little research on the fracture behavior of B/Al systems at elevated temperatures has been conducted so far, e.g. [24,25], despite the recognized and established advantages of B/Al under larger operating temperature ranges. Studies on the fracture behavior of specific B/Al systems such as unidirectional 8.0 mil B/Al-1100F [26,27], B/Al laminates [27,28], or the

effects of constituents on fracture behavior are even more limited, both at room and elevated temperatures.

The objective of the current research work has been to conduct a detailed and comprehensive study on the fracture behavior of B/Al composites at room and elevated temperatures with emphasis on the deformation behavior, load-time flaw growth, and the associated characterization methods. Special attention is also being given to nondestructive evaluation of damage growth, such as acoustic emission, X-ray radiography, ultrasonic C-scan techniques, and microstructural studies using scanning electron microscope (SEM) and photomicrography.

The effect of elevated temperatures on damage progression, notch sensitivity, and deformation characteristics is being investigated through a variety of experimental techniques and the results are being compared with their associated analyses.

In this study, five laminates of 5.6 mil B/Al-6061F are being investigated: $[0]_3$, $[90]_3$, $[\pm45]_{2s}$, $[0/\pm45/90]_s$ and $[0_2/\pm45]_s$. In addition, the effect of constituents on the fracture behavior of unidirectional and transverse composites is being studied, and the experimental work includes studies with 8.0 mil B/Al-1100F and all combinations of fiber diameter and matrix alloy, at both room and elevated temperatures.

This report summarizes results obtained to date on the fracture behavior of unidirectional and transverse 5.6 mil B/Al-6061F. The experimental results are presented and correlated with a number of existing analytical approaches. The experimental techniques are fully described and a discussion of the results obtained is presented. Currently, we are engaged in a more detailed study of the fracture behavior of these systems at elevated temperatures, and the work on the effect of constituents and of laminates has commenced.

## II. EXPERIMENTAL PROCEDURE

A. Introduction - The experimental procedure employed in this program included a variety of techniques from which the material mechanical properties, fracture behavior, deformation characteristics, and failure modes were examined. These techniques include: a laser interferometry displacement gage for obtaining local load-crack opening displacement (COD) curves at room and elevated temperatures from which local compliance curves and the K-calibration factor are obtained; a standard compliance gage for obtaining far-field load-displacement curves together with global compliance curves; and standard strain-gages for characterizing the material elastic properties at room and elevated temperatures. In addition, nondestructive inspection techniques were employed, including acoustic emission and X-ray radiography for characterizing the internal damage prior to, during, and after failure of the composite laminates. Post-failure examination of the fracture surfaces was carried out as well using scanning electron microscopy and optical microscopy techniques.

All mechanical testing was performed on a closed-loop servo hydraulic Instron testing machine (Model 1331) at a displacement rate of 0.127 mm/min (0.005 inch/min).

Implementation of these techniques required the purchasing of a wide range of instrumentation, the details of which are given at the end of this Section. A general view of part of our testing facility is shown in Figure 1.

B. Materials - The material tested in this program is 5.6 mil B/Al-6061F, manufactuerd by DWA Composite Specialties. Two types of specimen were used: center-notched specimens with dimensions of 216 mm (8.5 inch) long x 25.4 mm (1.0 inch) wide; and unnotched specimens, from which basic mechanical properties are obtained, with dimensions of 216 mm (8.5 inch) long x 12.7 mm (0.5 inch) wide. Center notches of about 0.25, 1.27, 2.54, 5.1, 7.6, 10.2 and 12.7 mm (0.01, 0.05,

0.1, 0.2, 0.3, 0.4 and 0.5 inch, respectively) long and 0.37 mm (0.015 inch) wide were introduced by Electrical Discharge Machining (EDM) technique. All specimens were cut from approximately 216 x 216 mm (8.5 x 8.5 inch) plates by EDM, with minimum damage along the specimen edges. A list of specimens purchased is given in Table I.

In order to obtain maximum information and reliable data, the experimental program calls for one to three tests (data points) per crack length at each temperature and for each laminate. The exact number of tests is to be decided during the work when the reproducibility of the data is verified. The exact number of temperatures used in the testing program is to be determined according to the actual test results and the degree to which the temperatures effect the variables tested.

Each of the 300 specimens has been carefully measured at three locations along the length to ensure a minimum acceptable uniformity in specimen dimensions. The location of each specimen on the plate has also been recorded so that designation of specimens according to crack size and test temperature could be made randomly to ensure reliable test results.

The specimens were initially tested without using the standard end tabs. Instead, a piece of 0.1 mm (0.004 inch) thick plastic sheet was attached to the specimen surface on both sides of the specimen ends, backed by a 400 grit sanding paper. For all practical purposes this procedure successfully eliminated grip slippage. However, during the course of our acoustic emission studies we found that this gripping technique produces a large amount of acoustic emission, and in fact causes the recording of erroneous data. To avoid this unwanted emission, end tabs were used for many of the specimens tested for acoustic emission. The introduction of end tabs also improved the recording of crack opening displacement measured with the laser interferometric displacement gage (see Section II-C).

The end tabs were made of aluminum doublers, 25.4 mm (.10 inch) square, cut

TABLE I: LIST OF NUMBER OF SPECIMENS

| Material | No. of Spec. purchased | | No. of Spec. Machined | |
|---|---|---|---|---|
| | Notched | Unnotched | Notched | Unnotched |
| $[0]_8$ 5.6 mil - 6061F | 204 | 56 | 159 | 46 |
| $[90]_8$ 5.6 mil - 6061F | 67 | 27 | 67 | 27 |
| $[\pm 45]_{2s}$ 5.6 mil - 6061F | 68 | 36 | 68* | 127* |
| $[0/90]_{2s}$ 5.6 mil - 6061F | 68 | 36 | 68* | 127* |
| $[0]_8$ 8.0 mil - 1100F | 48 | 27 | 48* | 92* |
| $[0]_8$ 8.0 mil - 6061F | 48 | 27 | 48* | 92* |
| $[0]_8$ 5.6 mil - 1100F | 48 | 27 | 48* | 92* |
| Aluminum matrix 6061F | - | 30 | - | 30 |
| Aluminum matrix 1100F | - | 30 | - | 30 |

The machining of the B/Al material is done most effectively by Electrical Discharge Machining (EDM). This process is difficult and expensive, therefore those specimens which have not yet been machined and slotted will be machined under the second phase of this program.

* To be machined during the second year program of study.

from 1.27 mm (0.05 inch) 2024-T6 sheets, and glued with epoxy onto the specimen ends. Two types of adhesive material were used: the first consisted of aluminum matrix epoxy containing 90% aluminum by weight, and the second consisted of neat epoxy resin regularly used in tabbing resin matrix composites. In regard to both acoustic emission and crack-opening-displacement measurements, no difference between these two techniques was detected. Thus the second technique which is more simple to apply has been adopted.

C. Laser Interferometric Displacement Gage (IDG) - The laser interferometric technique has been successfully employed to measure the crack-opening-displacement (COD) of the center notched unidirectional metal matrix composite [29]. This technique enables measuring the COD very close to the crack surfaces (gage length of 500 μm) and was found to be highly sensitive in detecting crack tip damage, very accurate in the submicron scale, and simple to utilize. Moreover, this technique can be used in a large range of environmental temperatures [30]. Since a major effort in the experimental program involved utilizing the IDG for COD measurement, and since this technique has not been employed in fracture studies of composite materials, a detailed description of this technique is presented here.

The crack opening displacement (COD) was measured by means of laser interferometry technique which enables measuring displacement over a very short gage length. When a coherent monochromatic light from a laser source impinges upon two closely adjacent, reflecting indentations on the sample, it is reflected (diffracted) back at an agnle $\alpha_o$ with respect to the incident beam. The diffracted beams overlap, generating interference fringe patterns on either side of the incident laser beam. As the distance (d) between the indentations changes, due to the applied load, the two fringe patterns move. As this movement is observed from a fixed position, at an angle $\alpha_o$, it can be related to the change in distance ($\delta$d) between the indentations.

The equation locating the bright intereference fringes is [31]

$$d \sin \alpha_o = m\lambda \qquad (1)$$

where m is the fringe order (m = 0, ±1, ±2, ±3 ...), $\lambda$ is the wave length of the laser beam, d is the spacing between indentations and $\alpha_o$ is the angle between the incident and reflected beams.

The change in distance between indentations, i.e. the displacement $\delta d$, is related to the change in fringe order, $\delta m$, at the fixed observation point by:

$$\delta d = \frac{\lambda \delta m}{\sin \alpha_o} \qquad (2)$$

where $\delta m$ is the number of fringes (or fraction of fringes) passing the fixed observation position.

Using a laser beam wavelength ($\lambda$) of 0.6328 μm (He-Ne laser) and $\alpha_o = 45°$ the calibration constant $\lambda/\sin \alpha_o$ in Equation (2) is approximately 0.95 μm. Thus, a fringe motion of $\delta m = 1$ corresponds to a displacement of about one micron. Since a shift of one half fringe movement is easily detectable, a resolution of the measurement easily reduces to a submicron scale. The displacement range in this technique is limited and depends on the spacing between indentations, dimensions of the indentations, and the power of the recording system. However, a displacement range of up to 300 μm is easily obtained in our experiments.

In order to obtain clear fringe patterns, the specimens should have a fairly flat, smooth and reflective surface. A shallow reflective indentation of a pyramidal shape was applied to the specimen surface on either side of the center of the crack with a Lietz microhardness tester. The dimensions of the indentations are approximately 50 x 50 μm. The original distance between the two indentations is about 500 μm, with edges normal and parallel to the crack surfaces, as shown in Figure 2.

The instrumentation system for measuring the crack opening displacement is simple and economical and consists of a Spectra Physics Model 120, 15 mW He-Ne laser, two photoresistor detectors, two signal amplifiers with d-c voltage output, and a three-channel stripchart recorder, as shown schematically in Figure 3. The sensing elements were two CdS bulk effect photoresistors. The active face of each of them was masked, leaving a 0.1 mm slit which was narrower than the fringe spacing so that the photoresistors responded to well defined maximum and minimum values of intensity. The output signals of the photoresistors were recorded on a stripchart recorder through a d-c amplifier. This recording technique is essentially similar to the one described in Reference [32]. A comprehensive description of the laser interferometric technique is given in Reference [33].

Figure 4 shows a typical intensity plot obtained on the stripchart recorder as the fringe patterns pass by the two stationary photoresistors. This particular plot (Figure 4) is for a boron/aluminum specimen having a 12.85 mm (0.5 inch) long crack. The data reduction of these signals is fairly easy, although very time consuming. Correlating the time at which various maxima and minima occur ($\delta m$ = 0, 1/2, 1, 1 1/2...) with the load-time plot obtained from the Instron chart recorder output yields the required load-COD curve, Figure 4. Fringe motion occurs with any rigid body motion of the sample. However, rigid body motion can be eliminated by averaging the displacement obtained from the upper and lower (Figure 3) photoresistors [33].

It should be noted that the IDG technique has been successfully employed for metal matrix composites [26,27,29,34,35] as well as for resin matrix composites [36,37].

D. Compliance Gage - A standard Compliance Gage of 25.4 mm (1.0 inch) gage length was used to test for the basic material properties of the unnotched specimens and to obtain the far-field load-displacement curves for the center-

notched laminates. For the latter, the compliance gage was positioned so that the crack was at the center of the gage section. The far-field load-displacement curves and their resulting global compliance curves are compared with the load-COD curves obtained by means of the IDG technique and with its resulting local compliance curves.

E. Strain Gage - Selected specimens were strain-gaged for room and elevated temperature testing. Since all strain gages, strain gage instrumentation and tools were purchased from Micro-Measurements (M.M.), the techniques used in bonding the strain gages follows M.M. Instruction Bulletins (I.B.).

1. Room Temperature Strain Gages: Surface preparation followed the procedures described in I.B. B-129. The bond system used was M-Bond 200 (Eastman 910) and was applied according to I.B. B-127-5. Three types of strain gage systems were applied:

a. For axial measurements: M.M. EA-06-125AC-350 (gage length = 3.18 mm, grid width = 3.18 mm).

b. For Poisson's ratio measurements: a 90° rosette composed of two separate gages, M.M. EA-06-062TT-350 (gage length = 1.57 mm, grid width = 1.91 mm).

c. In-plane shear modulus measurements: two types of 90° rosettes will be applied on $[\pm 45]_{2s}$ B/Al laminate* following Rosen [38] procedure for measuring in-plane shear modulus:

1) a 90° rosette type M.M. WK-06-062TT-350 (gage length = 1.57 mm, grid width - 1.91 mm). This rosette has a common electrical connection between the gages, resulting in a direct measurement of $(\varepsilon_x - \varepsilon_y)$ in the recording system.

* To be conducted in the second phase of this program.

2) Same 90° rosette that was used for the Poisson's ratio as described above. It should be noted that both techniques have resulted in very similar results for the in-plane shear modulus.

The bridge amplifier system used was a six-channel Vishay Instruments 2100 System. Bridge excitation voltage was set at one volt to minimize zero drift due to heat build-up on the gage grid. All strain readings were corrected for errors due to transverse deformation of the strain gage according to the M.M. Technical Note TN-137.

2. Crack Propagation Gage: For notched unidirectional and transverse B/Al, crack propagation gages were used to measure the initiation of axial plastic deformation and splitting of the matrix. Two M.M. TK-09-CPB02-005 gages were employed at both crack tips at a distance of 0.76 mm (0.03 inch) from the crack surface. This gage includes ten grid lines with a spacing of 0.254 mm (0.01 inch). The circuitry used for the crack propagation gage is described in M.M. PB-110-2. Test results obtained to date with this gage indicate the early occurance of crack tip damage growth, however they are inconclusive and are not reported here.

3. Elevated Temperature Strain Gages: For elevated temperature strain-gaging the specimen surfaces were prepared according to the M.M./I.B. B-129. The M.M. M-BOND 610 was used and applied according to M.M./I.B. B-130-6. The glue was cured at 350°F for one hour, making sure that the heating rate did not exceed 20°F/min. Silver solder was applied as described in M.M. TN-129. This procedure requires special care and experience to avoid breaking the strain-gage leads. For the elevated temperature axial gage, type M.M. WK-06-125AD-350 (gage length = 3.18 mm, grid width = 3.18 mm) series was used. The strain gage circuitry includes a dummy specimen to compensate for thermal

strains (two-arm bridge) and signals were conditioned by the Vishay 2100 Model Signal Conditioner.

F. Failure Modes - In addition to the procedures described above for monitoring damage, the fracture surfaces were examined after failure using Scanning Electron Microscope (SEM). In order to obtain a better view of the fracture surfaces and so better understand the different modes of failure, a successful attempt has been made to obtain stereo (three-dimensional) views of the fracture surface.

Photomicrographs were prepared as well to monitor internal damage at various locations along the specimens both before and after failure.

G. Acoustic Emission - A Dunegan/Endevco 3000 series acoustic emission monitor was used to monitor damage initiation and propagation in $[0]_8$ and $[90]_8$ B/Al speicmens. Acoustic emission has been monitored for each specimen tested and the results are described in Section IV. The data recorded include accumulative events and counts and count-rate as a function of load, line-location of events, and amplitude distribution histograms of events occurring within a pre-set area of interest along the specimens, as well as the Cumulative Events Amplitude Distributions (CEAD) and number of counts per event. All these data were recorded on X-Y recorders.

A major effort of this research program was to monitor damage initiation and progression through acoustic emission for the different B/Al laminates at room and elevated temperatures, notched and unnotched specimens. Because of the importance of this part of the overall program, a more detailed description of the significance of monitoring acoustic emission and the instrumentation used is given in Section III.

H. X-ray Radiography - This nondestructive test technique has been employed for three major purposes: 1) to detect internal damage and monitor crack tip damage growth, 2) to compare X-ray radiography results with other nondestructive techniques such as ultrasonic C-scan, 3) to attempt a correlation between

monitoring damage growth through acoustic emission and X-ray radiography.

A Hewlett-Packard Faxitron model 43804N X-ray cabinet with a 3 mA continuous current and beryllium window (0.63 mm thick) was used with a focal distance of 6.45 mm. The specimens were X-rayed at 20 kV and exposed for 10 minutes. All photographs used Polaroid Type 57 film.

Monitoring damage through X-ray radiography has not revealed any conclusive results at this stage, therefore the results are not reported here. Additional studies are warranted before any useful information can be presented.

I. Equipment Used - As described above, the experimental program of this research work entailed the use of a variety of equipment and instrumentation. The following is a list of all equipment purchased for and/or built in our Composites Laboratory during this program period and which has been used in this research activity.

1. Spectra Physics Model 120 Helium Neon Laser Unit 15 mW
2. Soltec Model 330 3-Pen Strip Chart Recorder
3. Photocell amplifier*
4. Laser unit bench*
5. IDG oven*
6. Omega Digital Thermometer Model 2166A (Ten thermocouples)
7. Omega Dual Set-Point Temperature Controller Model 4002
8. Vishay Instruments Strain Gage Conditioner and Amplifier System (Six Channels) Model 2100
9. Vishay Instruments Gage Installation Tester Model 1300
10. Vishay Instruments Strain Indicator Model P-350A
11. Vishay Instruments Multi-purpose Digital Strain Indicator Model V/E-20A
12. Vishay Instruments Auxiliary Digital Strain Indicator Model V/E-13
13. Hewlett-Packard X-Y-Y' Recorder Model 7042A (Two Units)

---

* Home-made units

14. Data Acquisition System PDP 1103 Model MINC-11 (supported in part by the Air Force Office of Scientific Research)

15. Dunegan/Endevco 3000 Series Acoustic Emission Instrumentation (supported in part by NASA Langley Research Center)

16. Hewlett-Packard X-Ray Cabinet, Faxitron Model 43804N.

17. Wassco Glo-Melt Resistance Soldering Unit.

## III. ACOUSTIC EMISSION INSTRUMENTATION

A. Introduction - A wide range of non-destructive inspection (NDI) techniques are used to detect internal damage and damage growth in composite systems. Ultrasonic pulse echo, brittle casting, Moiré, X-ray and neutron radiography photoelastic coating, thermography, laser holography, acoustic emission and others are used to study those types of damage which are of principle concern, namely, delamination, matrix crazing and fiber failure. Monitoring acoustic emission appears to offer the most practical procedure for detecting damage and damage growth because it is more readily used in actual service as well as in the laboratory. This is crucial for composite systems since the composite material is fabricated during the manufacturing of the composite structure, thus some means of nondestructive testing of the complete component including data analyses in real-time is required. Therefore, it is not surprising that numerous works have focused on the applicability of acoustic emission to damage detection and monitoring in various composite systems (e.g. [39-47]).

Significant improvements and modifications have been made on acoustic emission instrumentation, including features for the detection and location of defects, amplitude analysis, frequency analysis, RMS, spatial discrimination, and voltage controlled gating, among others, which are coupled with data acquisition systems to display the information in real-time. The more modern systems enable determination, not only of the existence of damage, but of the type and extent of damage. From the information obtained, conclusions can be drawn as to location of specimen failure and the probable mechanism of failure.

In this current study, application of acoustic emission is an important tool in detecting damage progression. The tests are carried out using notched specimens for which damage progresses outwards from the notched area, i.e.

from the crack tip. The damaged area should be the primary source of acoustic emission signals. The rest of the material should be relatively "silent". Thus, the results will demonstrate whether the source locations technique can be used to locate damage, track damage progression and identify potential fracture sites in B/Al structures.

These tests were carried out for various crack length-to-width ratios from 0.05 to 0.5, as well as for unnotched specimens for $[0]_8$ and $[90]_8$ laminates. It is expected that the results of the study will reveal the relationship between the manifested acoustic emission characteristics and factors such as damage size and material degradation. In other words, the acoustic emission characteristics should define the damage size and material degradation.

B. Instrumentation Capabilities - As mentioned above, the new modern and sophisticated acoustic emission instrumentation enables us to define the various failure mechanisms within the composite system and to track the location of activity. This failure characterization and the tracking procedures are achieved by analyzing certain characteristics of each acoustic emission event, such as peak amplitude distributions, rise time, counts, pulse duration, arrival time, etc. The selected instrumentation provides spatial discrimination, spatial filtering, and voltage controlled gating to eliminate unwanted background signals. The acoustic emission information is obtained by means of amplitude analysis and plotting of location.

Location plotting: Linear location of defects is obtained using two transducers, one at each end of the specimen. The source of the event is located by measuring the difference in the time of arrival of the signal at the sensors. This location data is stored in memory and simultaneously displayed as a histogram on a monitor oscilloscope and reproduced on an X-Y recorder. Thus, a history of activities and location can be obtained.

Amplitude Analysis: This analysis provides amplitude distribution histograms of the various events. From such histograms the various failure mechanisms can be identified. Damage mechanisms which yield low amplitude emissions are characteristic of matrix crazing. The medium peak amplitudes are characteristic of delamination, while the higher peak amplitudes represent fiber fracture. The spectrum of amplitude values ranges between 30dB to 100dB. The spectrum of amplitude distribution is displayed on the monitor oscilloscope and reproduced with an X-Y recorder.

Spatial Discrimination: This technique separates unwanted background noise from valid data and is based on blocking signals from the ends of the specimen. Machine noise, grip noise and tab debonding are all screened from valid data. A four transducer set-up is used. Two inside data transducers are needed for the linear location plotting. Two guard transducers which are placed outside each data transducer function to discriminate machine and other unwanted noise from valid data. The spatial discrimination can be responsible for lowering the threshold amplitude down to 30 dB.

Voltage Controlled Gating: The operation of the linear location and amplitude data instruments can be controlled by an external analog signal such as the outputs of a load-cell, strain gage, etc. The VCG allows the system to operate only during a preselected portion of the load cycle, determined by a high and/or low limit pre-setting on the VCG. This procedure is particularly useful during cyclical test situations such as fatigue tests because it can deactivate the data-taking systems when the load drops below a predetermined value, and thus eliminate the recording of unwanted information.

Counts and Events: An independent counting function is possible, displaying the number of counts from 0-999,999 in real time. It is possible either to accumulate total counts or to obtain count rate. The total number of accumulative events can also be obtained up to 999,999 events in real-time. Both counts and events can be obtained from the entire specimen length or from a pre-set specific

area of interest, the so-called "window" in the specimen which serves as a spatial filter. The Dunegan/Endevco 3000 acoustic emission system used in this study is shown in the block diagram of Figure 5. Schematics of some of the available information obtained from the AE measurements are shown in Figures 6 and 7.

C. Instrumentation - The list of modules used by our Composite Laboratory is shown in the block diagram in Figure 5. In this section some of the most pertinent operating parameters are listed.

1. Threshold level used in Model 921 Amplitude Detector is 40 dB.
2. A fixed gain of 40 dB on Model 1801-170B preamplifier was used.
3. Voltage gain on Model 302A Dual Signal Conditioner is 40 dB. Therefore, the total system gain is 80 dB.
4. Envelope on Model 90A Amplitude Analyzer was set at 1 m sec.
5. Model 920A Amplitude Analyzer was set at "Locate" mode of test, to provide a location distribution histogram of events.
6. Amplitude distribution histograms were recorded from Model 922 External Memory.
7. Dead Time on Model 922 External Memory was set at 1 m sec.
8. Spatial filtering was achieved by setting the "window" on Model 920A Amplitude Analyzer at 20 ÷ 80. In a few cases a "window" range of 30 ÷ 70 was used.
9. Accumulative Events within the "window" were obtained from Model 920A Amplitude Analyzer.
10. Accumulative counts within the "window" were obtained from channel A of Model 303 Dual Counter.
11. Count Rate within the "window" was obtained from channel B of Model 303 Dual Counter.
12. Wherever Guard transducers were used, a voltage gain of 40 dB was set on the second available Model 302A Dual Signal Conditioner.
13. Wherever spatial discrimination was used, the Event Envelope Selector was set at 10 m sec on Model 420 Spatial Discriminator.

## IV. RESULTS AND ANALYSES

A. Mechanical Properties - The experimental results on elastic stiffness and strength for $[0]_8$ and $[90]_8$ 5.6 mil B/Al-6061F are listed in Table II. A limited amount of data at elevated temperatures has been recorded so far, and it is reported later.

The values of the axial and transverse stiffness were obtained either with an extensometer of 25.4 mm (1.0 inch) gage length or with strain gages. Both techniques yielded similar results, verifying that the accuracy of the extensometer reading is satisfactory. The Poisson's ratio has been obtained with the strain gages described in Section II. The in-plane shear modulus data will be obtained during the second phase of this study when the $[\pm 45]_{2s}$ laminates are available.

Regarding the average axial strength data (of 11 specimens) a surprisingly low value of 1337 MPa (194 ksi) has been recorded. The data shown in the literature gives values of 1520-1655 MPa (220-240 ksi), even reaching values as high as 2004 MPa (290.7 ksi) [34]. Moreover, a very large scatter in the data has been observed; values range between 1187 and 1473 MPa (172.2 ÷ 213.7 ksi) with a standard deviation of 87.6 MPa (12.7 ksi). Examination of the fracture surface morphology (see Section IV-H) did not reveal the reason for either the low strength values or the large scatter. We are still in the midst of addressing this issue. The axial and transverse stiffness and the transverse strength recorded in our study (Table II) agree with data appearing in the literature. Typical stress-strain curves obtained with the strain gages are shown in Figure 8.

B. Load-Crack Opening Displacement Curves - As mentioned in section II, two methods were used to obtain load-displacement curves for the center-notched specimens. The far-field load-displacement curves were obtained using the 25.4 mm (1.0 inch) compliance gage, while the load-COD curves were obtained

TABLE II. MECHANICAL PROPERTIES

I. Unidirectional $[0]_8$

$E_L$ = 197.32 GPa (28.62 x $10^3$ ksi)

$\nu_{LT}$ = 0.230

$\sigma_f$ = 1337.5 MPa (193.99 ksi)

$G_{LT}$ = Unavailable

II. Transverse $[90]_8$

$E_T$ = 133.27 GPa (19.33 x $10^3$ ksi)

$\sigma_f$ = 105.3 MPa (15.28 ksi)

using the IDG technique. An example of the far-field load-displacement curves for six different crack lengths for unidirectional B/Al is shown in Figure 9. The load-COD curves for similar crack lengths are shown in Figure 10. A comparison between compliance gage load-displacement curves and IDG load-COD curves reveals the latter to be considerably more nonlinear as the load approaches its ultimate values. Moreover, from the initial slope of both curves, Figures 9 and 10, it is clear that the initial slopes of the load-COD curves (IDG) are more sensitive to the size of the damage. A detailed examination of the load-COD curves also shows rapid increases in COD at the higher load levels. For the unidirectional specimens and for the larger crack sizes, the actual crack opening is slightly larger than indicated in Figure 10. However, no details are shown here because the fringe patterns of the IDG are practically lost as the load approaches approximately 98% of its ultimate value and, for all practical purposes, no data reduction is possible. The loss of the fringe patterns at this load range has been attributed primarily to the very large crack opening displacement, causing the indentations to move out of the focal point of the laser beam. The large COD for unidirectional B/Al is not surprising, being itself attributed to the considerable longitudinal plastic deformation of the matrix at the crack tip which is associated with crack tip damage growth [34]. It should be noted, however, that at this load range the load-COD curve has already approached a plateau.

Figure 11 shows a loading-unloading-COD curve obtained with the IDG for a unidirectional specimen having a crack length of 7.56 mm (0.298 inch). Again, when the IDG is used, the crack tip damage is manifested in a highly nonlinear load-COD curve and in large permanent COD remaining upon unloading. This permanent COD is indicative of crack tip damage which appears primarily in the form of matrix plastic deformation and fiber failure at the crack tip. Further discussions on crack tip damage and failure modes is given in section IV-H.

Similar results were obtained for transverse $[90]_8$ specimens for the far-field load-displacement curves, Figure 12, and load-COD curves, Figure 13, for three crack lengths. It is interesting to note that both curves are initially linear, followed by very large deformation as the load approaches its ultimate values. Also note that these curves do not follow the expected behavior of having larger compliance and lower ultimate strength with increased crack size. In other words, there is insignificant notch sensitivity and large scatter.

As indicated in Figures 12 and 13, the actual deformation prior to failure is, in fact, much higher than that indicated by the load-displacement curves. It should be noted that, as the load approaches its ultimate value, a sudden drop in load occurs, about 20%-50% of its previous maximum value, Figure 14. Recalling that tests were conducted under stroke control, a sudden increase in crack tip damage, causing a large crack opening, may cause such a drop in load. As loading proceeds, additional slow crack opening is observed until an additional drop in load occurs. This process may repeat itself several times as shown in Figure 14. Thus, under stroke control conditions, a step-wise crack tip damage growth is observed.

For transverse specimens the load-COD curves are more complicated. As the crack tip damage extends, a sudden drop in load occurs, identical to that described above. This drop in load may in turn cause a potential crack closure. Because the IDG employed in this program cannot distinguish between crack opening and crack closure, the plots of the load-COD curves have been terminated just prior to the drop in load.

C. Compliance Curves - From both test procedures (IDG and Compliance gage), the compliance calibration as a function of the initial crack length has been

calculated. Since two different displacements were measured the appropriate compliances were defined accordingly: the local compliance, $C_\ell$, is based on COD obtained from the IDG, and the global compliance, $C_g$, is based on the far-field displacement.

In order to obtain accurate data on the local compliance, each specimen was loaded to a predetermined load (about 10% of the expected failure load) and then unloaded. This procedure was repeated three times. An examination of the load-COD curve reveals that the unloading curves as well as the subsequent loading curves are linear. In some instances, the first unloading revealed a very small amount of permanent crack opening, approximately 1-2μm, which indicates a small amount of crack-tip damage. However, this damage is sub-critical and practically does not affect the compliance measurements. Figure 15 represents three initial loading curves together with the local compliance values, $C_\ell$. It can be seen that the three values of $C_\ell$ are very close to each other, having a very small standard deviation (S.D.). The local compliance values given in Table III are the average values of the three loading curves. The global compliance values listed in Table III were obtained directly from the initial slope of the complete load-displacement curves when the recording system was set on high sensitivity to obtain good resolution.

The application of the energy release rate approach can predict the global compliance. The formulation is well established in the literature, e.g. [29], and will not be repeated here. The expression used for $C_g$ prediction is:

$$C_g = \frac{\alpha}{E_L B}\left[1.566(2a/W)^2 + 0.268(2a/W)^3 - 0.438(2a/W)^4 + 1.865(2a/W)^5 + 0.247(2a/W)^6 - 0.393(2a/W)^7 + 0.911(2a/W)^8\right] + \frac{L}{BWE_L} \quad (3)$$

TABLE III: EXPERIMENTAL VALUES OF LOCAL ($C_\ell$) AND GLOBAL ($C_g$) COMPLIANCES FOR 5.6 mil BORON/ALUMINUM-6061F

I. Unidirectional

| Crack - Length | | $C_\ell$ | Crack - Length | | $C_g$ |
|---|---|---|---|---|---|
| mm | (inch) | $10^{-3}$ μ/N | mm | (inch) | $10^{-3}$ μ/N |
| 1.29 | (0.051) | 0.94 | 1.29 | (0.051) | 3.07 |
| - | - | - | 1.29 | (0.051) | 3.31 |
| - | - | - | 2.57 | (0.101) | 2.96 |
| - | - | - | 2.57 | (0.101) | 3.20 |
| 2.67 | (0.105) | 1.12 | - | - | - |
| 5.03 | (0.198) | 1.73 | 5.03 | (0.198) | 3.47 |
| - | - | - | 5.08 | (0.200) | 3.54 |
| 7.50 | (0.295)* | 2.43 | - | - | - |
| 7.57 | (0.298)* | 2.39 | 7.57 | (0.298) | 3.85 |
| 7.57 | (0.298) | 2.72 | - | - | - |
| - | - | - | 7.65 | (0.301) | 4.12 |
| 7.72 | (0.304)* | 2.47 | - | - | - |
| 10.11 | (0.398) | 3.60 | - | - | - |
| - | - | - | 10.21 | (0.402) | 4.08 |
| 10.24 | (0.403) | 3.56 | 10.24 | (0.403) | 5.09 |
| 12.88 | (0.507) | 4.69 | 12.88 | (0.507) | 4.81 |
| - | - | - | 12.90 | (0.508) | 4.61 |

Elevated Temperature:

| Temperature | | Crack Length | | $C_\ell$ |
|---|---|---|---|---|
| °C | (°F) | mm | (inch) | $10^{-3}$ μ/N |
| 93 | (200) | 7.57 | (0.298) | 2.31 |
| 204 | (400) | 7.72 | (0.304) | 2.36 |
| 316 | (600) | 7.50 | (0.295) | 2.97 |

* Tested at room and elevated temperatures.

II. Transverse

| Crack - Length | | $C_\ell$ | Crack - Length | | $C_g$ |
|---|---|---|---|---|---|
| mm | (inch) | $10^{-3}$μ/N | mm | (inch) | $10^{-3}$ μ/N |
| 2.57 | (0.101) | 3.88 | 2.57 | (0.101) | 6.42 |
| - | - | - | 2.59 | (0.102) | 3.34 |
| 7.62 | (0.300) | 3.36 | 7.62 | (0.300) | 6.19 |
| - | - | - | 7.65 | (0.301) | 5.46 |
| 7.65 | (0.301) | 3.46 | - | - | - |
| 12.96 | (0.510) | 5.80 | 12.96 | (0.510) | 9.57 |

where W and B are the specimen width and thickness, respectively, L is the gage length of the compliance gage, and $E_L$ is the longitudinal stiffness of the laminate.

The orthotropic correction factor, $\alpha$, is given by

$$\alpha = \frac{1}{\sqrt{2}} \left[ \left( \frac{E_L}{E_T} \right)^{1/2} - \nu_{LT} + \frac{E_L}{2G_{LT}} \right]^{1/2} \tag{4}$$

where $E_L$ and $E_T$ are the longitudinal and transverse moduli, respectively, $\nu_{LT}$ the major Poisson's ratio, and $G_{LT}$ the longitudinal shear modulus. Equation (3) used the width correction factor Y given by [48]:

$$Y = 1 + 0.1282(2a/W) - 0.2881(2a/W)^2 + 1.5254(2a/W)^3 \tag{5}$$

Note that Equation (5) uses the isotropic width correction factor. It has been shown previously, e.g. [29], that this expression of Y is applicable for composites. Further discussion on the applicability of the isotropic width correction factor to B/Al composites will appear later in this section.

A comparison between the experimental results for the global compliance and prediction (Equation (3)) is shown in Figures 16 and 17 for unidirectional and transverse B/Al, respectively.

As shown in Figure 16, the agreement is not as good as that previously obtained for unidirectional B/Al [29]. No explanation for the discrepancy between experiment and prediction can be given at this stage and it appears that additional tests should be performed. It should be noted, however, that the longitudinal shear modulus has not yet been measured for the material system tested in this program. Therefore, the value of the orthotropic correction factor $\alpha$ (Eq. 4) has been estimated to be 1.2, as compared with a value of 1.303 used in [29].

The experimental results of the global compliance for the transverse specimens show relatively large scatter, Figure 17, and thus the comparison with prediction (Equation (3)) is inconclusive (the value of $\alpha = 1.05$). However, the experiments follow the trend of the predicted global compliance values which, as expected, are much higher than those obtained for the unidirectional specimens, Figure 16.

The actual crack opening displacement (COD) can be predicted from elastic stress analysis, and the local compliance curve can be calculated and compared with the experimental COD (and compliance) obtained with the IDG. Since the COD was practically measured at the crack surfaces (gage length of 0.02 inch) and at the center of the crack, the predicted displacement v in the loading direction of the top crack surface is given by [49-51]:

$$v = \frac{2\sigma a \alpha}{E_L} Y \qquad (6)$$

Since the COD is the relative displacement at the center of the crack, which is equal to 2v, the local compliance becomes:

$$C_\ell = \frac{COD}{BW} = \frac{2\alpha}{E_L B} \frac{2\alpha}{W} Y \qquad (7)$$

The predicted local compliance curve (Equation (7)), based on the isotropic Y, was compared with the experimental results given in Table III. For the unidirectional B/Al an excellent agreement was established, as shown in Figure 18. Note that the present results agree very well with those previously obtained [29] for a similar material system. The slight discrepancy between prediction and experiments is attributable primarily to the fact that the COD is not measured exactly at the crack surfaces, i.e. the gage length of 0.02 inch is slightly larger than the average crack width of 0.015 inch. The smaller the crack length, the larger the effect of the gage length will be. The comparison between prediction and experiments for the $[90]_8$ specimens, Figure 19, is not conclusive as yet

because of the large scatter in the experimental results. Additional testing will be required here to demonstrate the applicability of both test procedure and analysis to this material.

It is of interest to note that the local compliance curve (Figures 18 and 19) is much more sensitive to changes in crack length, i.e. damage size, than the global compliance curve, Figures 16 and 17. Therefore, the local compliance curve can also serve as a more accurate tool for calculating the crack growth resistance curve:

$$K_R = Y \sigma \sqrt{\pi a_e} \tag{8}$$

where $a_e$ is the <u>effective</u> crack half-length obtained from the local compliance calibration curve.

The experimental local compliance can also serve for calculating the width correction factor Y by rewriting Equation (7) as follows:

$$Y = \frac{E_L B}{2\alpha} \frac{C_\ell}{2a/W} \tag{9}$$

The term $C_\ell$ (2a/W) is the secant slope to each experimental value of the compliance in Figure 18. Thus Y is proportional to this slope. A comparison between the experimental results for Y(together with results obtained previously [29]) and Equation (9) is shown in Figure 20, evincing quite a good correlation for the larger crack lengths. For the smaller crack lengths the scatter is quite high, but it must be remembered that any experimental scatter in compliance measurements causes a larger error in the slope, $C_\ell/(2a/W)$, for small crack lengths. Also, the analtyical equations formulated for sharp cracks will no longer apply to real cracks of a smaller length, since the crack width-to-length ratio becomes larger. In addition, any crack-tip damage will have a more significant effect on the elastic compliance so that the initial slope of the subsequent loading-unloading curve may not accurately represent the compliance. However,

analytically, the deviation of Y from the isotropic values is negligible as the crack length gets smaller [52], and no K-calibration is needed for small cracks. Y is smaller than 1.001 for cracks having 2a/W less than 0.1, thus poor correlation for small cracks is of little significance.

D. Elevated Temperature Load-COD Curves - Elevated temperature load-COD curves and local compliances were obtained for unidirectional B/Al specimens as well. A comparison between room temperature (21°C) and elevated temperature (93°C, 204°C and 316°C) load-COD curves for a crack length of approximately 7.60 mm (0.30 inch) is shown in Figure 21. The results indicate that at least up to 93°C (200°F), temperature has practically no effect on the deformation characteristics and crack tip damage growth. Load-COD curves at both temperatures are very similar. A further increase of temperature, up to 204°C (400°F), already reveals a larger nonlinearity in the load-COD curve, resulting also in a larger COD at failure. When the operating temperature is again increased up to 316°C (600°F), a significant effect is observed, Figure 21. Both the nonlinearity in load-COD curve and the large COD at failure are primarily attributable to the greater ductility of the aluminum matrix at elevated temperatures. Note that the typical failure mode at the crack tip is matrix shear plastic deformation along the fibers and in the loading direction. In other words, differences between the curves indicates much larger crack tip damage growth at elevated temperatures which results from the elevated temperature properties of the matrix material.

The effect of elevated temperatures on the deformation characteristics of notched unidirectional B/Al composites is already significant, even at low load levels, Figure 22. A comparison between local compliances recorded at room and elevated temperatures shows the elevated temperature (316°C) compliances to be increased by about 25% over the room temperature compliance. A minimal effect on local compliance is observed at temperatures up to 204°C (400°F), however,

above this temperature the effect is significant, Figure 22. These results indicate the influence of matrix yield shear strength on the load-COD curves even at low load levels [34]. A more detailed study covering the temperature range 200°C - 350°C (400°F - 660°F) is warranted.

To eliminate variations in local compliance due to differences in properties and/or crack size, the same specimen was used to obtain the local compliance at both room temperature (21°C) and elevated temperature (316°C), Figure 23. Again, there is an increase of about 22% in local compliance, Table III.

E. Fracture Strength - Fracture strength results are listed in Table IV for various crack lengths. These data are compared with an existing model suggested by Waddoups, Eisenman and Kaminski (WEK) [53], who assumed the existence of intense energy regions at the edges of the notch which are modeled as edge cracks of size $c_o$. With this in mind, the linear elastic fracture mechanics is applied, and the fracture strength can be predicted according to:

$$Y \frac{\sigma_f}{\sigma_o} = \left( \frac{c_o}{a + c_o} \right)^{1/2} \qquad (10)$$

where $\sigma_f$ and $\sigma_o$ are the notched and unnotched strength, respectively. It should be noted that $c_o$ can only be obtained experimentally by performing at least one fracture test, and must be determined for each composite system independently. A similar model has been mathematically formulated by Whitney and Nuismer [15,54], called the "average stress criterion", and which assumes that failure occurs when the average stress over a certain distance ahead of the crack-tip equals the unnotched strength. Both of these models have been widely used in recent years for predicting laminates' notch sensitivity, e.g. [55-57]. However, this is a semi-empirical approach because $c_o$ must be determined experimentally.

Since $c_o$ is assumed to be a material property, i.e. a quantity independent of crack size, rearranging Equation (10) will give $c_o$ as the slope of the following equation:

TABLE IV. NOTCHED STRENGTH DATA FOR 5.6 mil BORON/ALUMINUM-6061F

I. Unidirectional

| Crack-Length mm | (inch) | Notched Strength MPa | (ksi) |
|---|---|---|---|
| 1.29 | 0.051 | 977 | 141.75 |
| 1.29 | 0.051 | 1216 | 176.36 |
| 1.32 | 0.052 | 1217 | 176.58 |
| 2.57 | 0.101 | 1013 | 146.99 |
| 2.57 | 0.101 | 869 | 126.08 |
| 2.59 | 0.102 | 1123 | 162.83 |
| 2.67 | 0.105 | 1114 | 161.59 |
| 5.03 | 0.198 | 877 | 127.26 |
| 5.06 | 0.199 | 894 | 129.66 |
| 5.08 | 0.200 | 977 | 142.10 |
| 7.57 | 0.298 | 713 | 103.46 |
| 7.57 | 0.298* | 808 | 117.22 |
| 7.62 | 0.300 | 788 | 114.29 |
| 7.65 | 0.301 | 725 | 105.20 |
| 7.72 | 0.304** | 811 | 117.62 |
| 10.19 | 0.401 | 672 | 97.44 |
| 10.19 | 0.401 | 579 | 84.05 |
| 10.21 | 0.402 | 652 | 94.56 |
| 10.24 | 0.403 | 651 | 94.37 |
| 10.24 | 0.403 | 625 | 90.65 |
| 10.67 | 0.420 | 615 | 89.27 |
| 12.88 | 0.507 | 549 | 79.57 |
| 12.88 | 0.508 | 547 | 79.36 |
| 12.90 | 0.508 | 502 | 72.84 |

* Tested at 93°C (200°F)
** Tested at 204°C (400°F)

II. Transverse

| Crack Length mm | (inch) | Notched Strength MPa | (ksi) |
|---|---|---|---|
| 2.59 | 0.102 | 90 | 13.07 |
| 2.59 | 0.102 | 86 | 12.50 |
| 7.62 | 0.300 | 76 | 11.09 |
| 7.65 | 0.301 | 92 | 13.38 |
| 7.65 | 0.301 | 115 | 16.75 |
| 12.95 | 0.510 | 48 | 6.97 |

$$a = c_o \left[ \left( \frac{\sigma_o}{Y\sigma_f} \right)^2 - 1 \right] \qquad (11)$$

Figure 24 shows the experimental results plotted according to the format of Equation (11). The solid lines represent a least squares fit of $c_o$ which was found to be 1.86 mm (0.073 inch). As seen in Figure 24, the use of a constant value for $c_o$ for different crack lengths appears to be justified. Figure 24 also shows the results obtained previously [34] for a similar material system. Comparing the results of the present work with those obtained in [34], it is seen that the latter has a much smaller $c_o$, indicating a higher notch sensitivity. Whereas the higher value of $K_c$ in [34] arises from the fact that the material studied here has only 68% of the unnotched strength of the material tested in [34]. It should be emphasized that the primary differences between the material systems studied in [34] and in the present work are the fabrication procedures and parameters employed. Their effect on notch sensitivity has also been discussed in [34]. Although we expected similar results for both material systems, the differences in slope, as shown in Figure 24, are striking.

Using the value of $c_o$ from Figure 24, the fracture strength can be predicted from Equation (10), Figure 25, and a good correlation has been established. Quite a significant notch sensitivity is observed for the material system tested in this program, however the B/Al results of [34] show even higher notch sensitivity, by about 25% for the medium crack sizes.

Values of the critical stress intensity factor, $K_c$, obtained from the equation:

$$K_c = Y\sigma_f \sqrt{\pi(a + c_o)} = \sigma_o \sqrt{\pi c_o} \qquad (12)$$

are also given in Figure 25, and listed in Table V.

Another approach to analyzing the fracture strength data, suggested by Mar and Lin (ML-model) [12,58,59], is to assume:

$$\sigma_f = M(2a)^{-m} \tag{13}$$

where M and m are determined so as to best fit the data. This model interprets m to be "the order of singularity of a crack lying in the matrix with its tip at the interface of matrix and filament."

The data obtained in this program are plotted on a log ($Y\ \sigma_f/\sigma_o$) versus log (2a/W) format, Figure 26. A least squares fit yields the values of the slope m, of the coefficient M, and of the coefficient of correlation (c.c.), as shown in Figure 26 and as listed in Table V. It can be seen from Figure 26 that Equation (13) represents the data quite closely. Similar agreement has been established for several other composite systems, Table V [26-28,34-37]. In order to compare these two approaches, Equations (10) and (13), the WEK model has also been plotted on a logarithmic format in Figure 27. A comparison between Figures 26 and 27 reveals that the first model, Equation (10), does more accurately represent the notch sensitivity of B/Al. A few tests were also conducted on the notched strength of $[90]_8$ B/Al for three crack sizes, Table IV. Although some degree of notch sensitivity is observed, there is too much scatter in the data to obtain any meaningful comparison with analytical prediction. Additional testing will be performed in the second program phase.

F. Notch Sensitivity - In studying the notch sensitivity of the different material systems it is customary to use the critical stress intensity factor, $K_c$, as a parameter indicative of notch sensitivity. Values of the critical stress intensity factor, Equation (12), are listed in Table V for thirteen different material systems (including the present results on B/Al), along with the values of the unnotched strength, $\sigma_o$, and the crack-tip damage size, $c_o$. The actual changes in $Y(\sigma_f/\sigma_o)$, representing the actual notch sensitivity, are also displayed in Table V for the values 2a/W = 0.3 and 0.5.

TABLE V: NOTCH SENSITIVITY*

| Material | Average Unnotched Strength MPA | (ksi) | (Equation (12)) $K_c$ MPa$\sqrt{m}$ | (ksi$\sqrt{in}$) | (Equation (11)) $c_o$ mm | (inch) | (Equation(13)) m | M | $Y\frac{\sigma_f}{\sigma_o}$ ($\frac{2a}{W}$ =0.3) | $Y\frac{\sigma_f}{\sigma_o}$ ($\frac{2a}{W}$ =0.5) |
|---|---|---|---|---|---|---|---|---|---|---|
| 5.6 mil B/Al-6061F [present] | 1338 | (194.0) | 102.0 | (93.3) | 1.87 | (0.0736) | 0.259 | 0.420 | 0.5843 | 0.4739 |
| 5.6 mil B/Al-6061F [34] | 2004 | (290.7) | 112.7 | (102.6) | 1.00 | (0.0396) | 0.321 | 0.313 | 0.3942 | 0.3653 |
| 8.0 mil B/Al-1100F [26,27] | 1273 | (184.6) | 108.4 | (98.7) | 2.31 | (0.0910) | 0.227 | 0.466 | 0.6207 | 0.5136 |
| 5.6 mil B/Al-6061F $[0/\pm22/0]_s$ [27,28] | 1335 | (193.7) | 56.1 | (51.0) | 0.56 | (0.0221) | 0.371 | 0.226 | 0.3597 | 0.2835 |
| BSiC/Ti-A [35] | 837 | (121.4) | 69.7 | (63.1) | 2.20 | (0.0868) | 0.258 | 0.449 | 0.6287 | 0.4858 |
| BSiC/Ti-B [35] | 807 | (117.4) | 69.4 | (63.1) | 2.35 | (0.0925) | 0.277 | 0.452 | 0.6798 | 0.5125 |
| 5.6 mil B/Al-6061F, Type I [34] | 1290 | (187.1) | 107.3 | (97.6) | 1.15 | (0.0455) | - | - | 0.6304 | 0.4901 |
| 5.6 mil B/Al-6061F, Type II [34] | 1432 | (207.7) | 91.8 | (83.5) | 1.31 | (0.0515) | - | - | 0.5117 | 0.4077 |
| 5.6 mil B/Al-6061F, Type III [34] | 1526 | (221.3) | 91.9 | (83.7) | 2.20 | (0.0867) | - | - | 0.5136 | 0.3938 |
| Gr/Ep AS/3501-5A $[0/90/+45/-45]_s$ [37] | 609 | (88.32) | 34.5 | (31.4) | 1.02 | (0.0401) | 0.415 | 0.286 | 0.4718 | 0.3588 |
| Gr/Ep AS/3501-5A $[0/\pm45]_s$ [37] | 660 | (95.69) | 35.4 | (32.2) | 0.91 | (0.0360) | 0.322 | 0.299 | 0.4069 | 0.3810 |
| Gr/Ep AS/3501-5A $[90/\pm45]_s$ [37] | 197 | (28.58) | 23.5 | (21.4) | 4.54 | (0.1787) | 0.288 | 0.537 | 0.7753 | 0.6268 |
| Gr/PI Celion 6000/PMR-16 $[0/+45/90/-45]_{2s}$ [36] | 433 | (62.74) | 39.1 | (35.5) | 2.59 | (0.102) | 0.207 | 0.459 | 0.5280 | 0.4061 |

* All specimens are 25.4 mm (1.0 inch) wide. Only Gr/PI is 50.8 mm (2.0 inch) wide.

Comparison of the $K_c$ values with the values of $Y(\sigma_f/\sigma_o)$, Table V, shows that the $K_c$ used in the two-parameter model, Equation (10), is not actually the proper indicator for notch sensitivity since it depends also on the unnotched strength. In other words, for high unnotched strength, $K_c$ may be as high as 100 MPa $\sqrt{m}$ while values of $Y(\sigma_f/\sigma_o)$ indicate high notch sensitivity. Conversely, the trend in the values of $c_o$ does follow the notch sensitivity characteristics as indicated experimentally by curve fitting Equation (10) with the experimental results. As long as this model, Equation (10), is accepted for predicting notched strength of composites, values of $c_o$ can serve as a proper indicator of notch sensitivity.

Although Equation (13) is applied through a curve fitting procedure to determine the constants M and m, it is of interest to note that these constants can also serve as an indication of the notch sensitivity as determined in terms of changes in $Y(\sigma_f/\sigma_o)$. Smaller values of m and higher values of M indicate a lesser degree of notch sensitivity. As seen in Table V, both m and M values consistently follow the notch sensitivity of the various composite systems.

G. Acoustic Emission (AE) - For all specimens tested in this program, acoustic emission was monitored using Dunegan/Endevco 3000 series AE instrumentation and results were recorded as explained in Section II-G and Section III. Some representative results are presented here including results for notched and unnotched unidirectional and transverse specimens.

Figures 28 and 29 show (on linear scales) location and amplitude distribution histograms of events, respectively, obtained at different loading levels for a unidirectional notched specimen (crack length = 12.90 mm). In order to avoid any accumulation of events during the data recording process, these distributions (and all those in the AE tests) were obtained while loading was in progress. It is of interest that the major activity occurred at the middle of the specimen (at about location "50") where the center notch was located. Initially, however, emission occurred evenly throughout the specimen length and only at higher load levels is it concentrated at the crack location.

The amplitude distribution histograms, Figure 29, indicate that events occur primarily in three amplitude ranges: 40dB - 55dB, 75dB - 85dB, and 92dB - 95dB. Assuming that the shape of the amplitude distribution histogram can be correlated with specific failure mechanisms, it seems that the occurrance of events in the high amplitude levels (90dB - 95dB) indicates fiber failure. It is interesting to note that such fiber failure is already observed at relatively low load levels (9.65 KN, 2170 lbs), or at approximately 50% of the ultimate load. This can be seen even more clearly in Figure 30, which shows the Cumulative Event Amplitude Distribution (CEAD) on a logarithmic scale for the same specimen. From the CEAD it seems that fiber failure occurred at load levels as low as 35% of the ultimate load.

Location or amplitude distribution histograms displayed on a logarithmic scale are advantageous whenever a low number of events is occurring at specific amplitude levels, but they may conceal information whenever a large number of events occurs. For this reason we used both linear and logarithmic scales for these distributions. Figures 31 and 32 show location and amplitude distribution histograms, respectively, on both scales for the same specimen, and they are obtained from data accumulated throughout the loading range up to failure. Figure 31 indicates that AE activity occurs practically throughout the specimen length, while the data on the logarithmic scale of Figure 32 shows more clearly the occurrance of a larger number of events at the three separate amplitude levels. The appearance of events at the two lower amplitude ranges can be attributed to several failure mechanisms such as matrix plastic deformation, fiber pull-out, or even internal friction between newly created surfaces. At this stage we cannot as yet identify which of the actual failure mechanisms is dominant. Additional studies would be required to correlate the specific failure mechanisms with the amplitude distribution characteristics.

The "b slope" of the Cumulative Event Amplitude Distribution (CEAD) can be indicative of failure progression. This CEAD can be represented as [60]:

$$F(V) = F(V_o) \left(\frac{V}{V_o}\right)^{-b} \tag{14}$$

where $V_o$ is the threshold value, V is the peak amplitude and "F(V) is defined as the number of events whose amplitude exceed V" [60] and is the CEAD. The constant b should be determined for each material system and deformation mechanism. More details can be found in [60]. Such a CEAD plot is shown in Figure 30 for six different load levels. No attempt has been made at this stage to correlate the "b slope" with failure, and more testing is required before any conclusions can be made. However, it is interesting to note that as the load increases, the value of $V_{max}$ (the peak amplitude of the largest emission) increases from about 87dB up to 97dB just prior to failure. In other words, high amplitude levels occur at relatively low load levels.

The fact that the AE data indicate fiber failure at low load levels has been addressed in more detail for the purpose of validating such AE data. The test results described above have been repeated for a similar unidirectional specimen with a crack length of 7.64 mm. The specimen was loaded up to 10.68 KN, approximately 40% of the expected ultimate load, and then unloaded. The AE data shown in Figures 33 and 34 are the accumulated data during the loading stage only. Again we see that events occur throughout the specimen length, Figure 33. The amplitude distribution histogram shown in Figure 34 is for those events occurring at locations "45" to "55", i.e. only those data occurring within a 13 mm long section at the center of which the crack is located. It can be seen clearly from Figure 34 that a relatively large amount of events occurred at amplitude levels of 85dB - 95dB (26 out of 60 events analyzed), indicating again the occurrance of fiber failure.

In order to compare these indications of fiber failure from the AE data with the actual crack tip damage, the specimen was removed from the testing machine, the outer foil of the aluminum matrix was dissolved, and the first layer of fibers was exposed and examined in the SEM. Broken fibers were seen in all four crack tips (on both sides of the etched specimen), as shown in Figure 35. The general shape of the failed fibers (note the broken fiber in the third layer of Figure 35a) is identical to that of fibers failed under load [35]: all broken fibers have multiple cracks; fibers are fragmented into wedge-shaped particles, Figure 35b; and the apexes of the wedge-shaped fragments point toward the original crack. It is possible that those broken fibers were slightly damaged during the machining (EDM) of the slit, causing premature fiber breakage, however a careful examination of those fibers at magnifications up to 3000X was not conclusive. Although the causes of premature fiber failure are not being addressed in this report, the SEM results do seem to indicate that fiber failure can be monitored through acoustic emission. Additional detailed studies are certainly warranted, and the second phase of this program will include AE studies of single filaments, neat matrices, single filaments embedded in aluminum matrices, and others.

As mentioned in Section II, two methods for clamping were employed in this program: a sandwiching of the specimen ends between pieces of 400 grit sanding paper, and the use of aluminum doublers as end tabs. Although the first method is simpler to utilize and has been satisfactory regarding grip slippage, the results of the AE studies indicate that this method distorts the AE data and may lead to erroneous conclusions. An example of location distribution histograms for a unidirectional B/Al specimen (crack length = 10.69 mm) clamped with the sanding paper is shown in Figure 36. The overall shape of this location distribution histogram is totally different from that obtained for a specimen having aluminum doublers as end tabs, Figure 28. First, no AE activity at the

crack location can be detected; second, large activity seems to occur around locations "30" and "70". The primary reason for this is that the sanding paper clamp causes acoustic emissions from both ends of the specimen at very high rates (almost continuously) which interact and reflect somewhere along the specimen. This interaction is picked up by both transducers and events are analyzed and located by the AE system, yielding the appearance of damage which does not actually exist. The localizing of these events at locations "30" and "70" is insignificant, being the result of the particular specimen geometry and the distance between the transducers used in this study. It should also be noted that the AE instrumentation has been set at a "Dead-time" of 3 msec and an "Envelope" of 10 msec. Thus, a considerable amount of real data may have been masked by the continuous emission from the specimen ends, accounting for the relatively small amount of emissions (compared with the data shown in Figure 28) recorded at the center of the specimen.

It is also of interest to compare the total number of events and counts recorded under both clamping methods, Figures 28 and 36. (Note that Figures 36 are presented in two different scales.) While using aluminum doublers as end tabs, only 1360 events were recorded, compared to 4896 events recorded for the specimen clamped with sanding paper. The number of counts is also much higher. Although the actual number of events and counts is not of importance since not all events and counts can be recorded by the AE instrumentation, the qualitative comparison is striking.

The amplitude distribution histogram for the specimen clamped with the sanding paper is shown in Figure 37 and is again strikingly different than that obtained for the specimen using aluminum doublers as end tabs, Figure 29. A larger difference is also observed in the Cumulative Event Amplitude Distribution (CEAD), Figures 38 and 30, which is much less steep at the higher amplitude levels under the sanding paper method. All of these AE results demonstrate

the importance of applying the proper clamping method to obtain AE information as reliably as possible.

The AE results obtained for unnotched unidirectional B/Al are shown in Figures 39 to 41. Generally, the distributions are the same as those obtained for unidirectional notched specimens, Figures 28 to 32; the amplitude distributions in particular indicate the appearance of similar failure mechanisms. However, it should be emphasized again that no definite conclusions can be drawn regarding a direct correlation between AE information and actual failure mechanisms until specific studies are conducted on "basic" systems such as single fibers, neat matrices, etc. for obtaining base-line calibration information.

The concentration of events at locations "30" and "70", Figure 39, is also observed for the unnotched specimens. Attempts to eliminate this by changing the clamping method were only partially successful, as seen from a comparison between Figure 39 and Figure 36.

In addition to the location and amplitude distributions described above, additional AE information was obtained in the form of accumulative events and counts and count rate, all as a function of load, and these have been correlated with far-field load-displacement curves (obtained from Figure 9), as shown in Figures 42 to 44 for a notched unidirectional B/Al specimen. The location and amplitude distribution histograms for this crack size, Figures 45 and 46, are very similar to those obtained for other crack sizes, e.g. Figures 31 and 32. In other words, the AE data are quite reproducible. Comparing the load-displacement curves with the AE data, Figures 42 and 43, it seems that there generally exists a qualitative correlation between the deformation characteristics and AE, i.e. jumps in displacement can be associated with increased AE activity. As the number of events (and counts) increases more rapidly with load, a higher nonlinearity in the load-displacement curve is observed.

In regards to the monitoring of counts and events, a large amount of counts is generally being recorded for notched B/Al composites, in the order of $10^5$, as compared with the total number of events, in the order of $10^2$, Figure 44. The number of counts per event may vary depending upon the load level and the amount of damage. Initially, about 100 counts accompany each event, but with increasing load the count per event can be 200 or higher, and may become as high as 300 counts per event just prior to failure. This phenomenon might be attributed to one of the following two reasons or a combination of both: 1) As damage progresses and the number of events increases, it may happen that two or more events interfere, depending also upon the duration of "Dead-Time" set in the instrumentation. When several events interfere, the system will register all of them as one event which includes some combination of the counts of the individual events; 2) As damage increases, higher amplitude events occur, possibly due to fiber failure, and thus a larger number of counts above the threshold level set in the system may be recorded.

Therefore the variation in counts per event with load might be attributed either to instrumentation setting or to variation in failure mechanism or to a combination thereof. In any case, the absolute number of events or counts recorded does not necessarily represent the actual degree of damage. The recorded data are a random representation of the total amount of emission.

Similar AE studies were carried out for notched $[90]_8$ specimens as well, with results shown in Figures 47 to 51 (crack size = 7.63 mm). Again, events are detected throughout the specimen length with minor additional AE activity at the crack location. Amplitude levels, Figure 48, are in the range of 40dB - 60dB and 72dB - 85dB with, surprisingly, a few events at higher amplitude levels of 95dB. It would seem that fiber failure also occurs in transverse specimens, and it will be shown later that some fiber splitting has been

observed in the SEM studies.

The total number of events (277) and counts (20,700) occurring prior to failure is much smaller than that observed in unidirectional B/Al (803 and 264,750, respectively). Since matrix deformation is the dominant failure mechanism, the fewer number of events occurring at lower amplitude levels was expected. Plots of events, counts and count-rate as a function of load were obtained and correlated with the far-field load-displacement curves obtained from Figure 12. As expected, no jumps in load-displacement curves were observed, however, the nonlinearity can be qualitatively correlated with increased AE activity with increasing load, Figures 49 and 50. Also, the number of counts per event, Figure 51, is relatively constant and smaller than that of unidirectional B/Al, Figure 44.

In the detection of damage growth through monitoring acoustic emission, it has been demonstrated for many isotropic materials that acoustic emissions occur only when the material is loaded beyond a previously applied load level, referred to as the Kaiser Effect [61]. Composite materials, however, behave somewhat differently, with emissions occurring below the previous load level. This phenomenon in composites is called the "Felicity Effect" [46,47], and the ratio of the load at onset of emission to the maximum previous load is defined as the "Felicity Ratio" [47]. This effect has been studied in the current work for various unidirectional B/Al specimens.

Several unidirectional B/Al specimens were loaded to a predetermined load and then unloaded. This procedure was repeated incrementally up to failure. During the tests, events, counts, count rate, location and amplitude distribution histograms, and CEAD were recorded.

A schematic representation of counts versus load during the unloading/reloading cycles is shown in Figure 52. Deviation from the Kaiser Effect is clearly seen, i.e. emissions occur prior to the previous load level. In other

words, the phenomenon referred to as the Felicity Effect has been verified. However, it was also found that emissions occurred during the early stages of unloading. Only upon further unloading does the material become acoustically "silent". More important, as shown in Figure 52, three to four load cycles were performed for a predetermined load level, and then repeated at several higher load levels. It is interesting to note that emissions occurred at each of the repeated loading cycles, decreasing with each cycle. Amplitude distribution histograms indicate low amplitude activity, within the 40dB to 60dB range. Therefore, it seems that this additional AE activity is primarily attributable to internal friction between newly created surfaces, ore even between fibers which are in direct contact with each other (see Section IV-G).

An attempt has also been made to determine the potential of the AE technique as an indicator of material strength, e.g. an acceptance-rejection criterion or an indicator of allowable load. For this purpose the AE tests also monitored the number of recorded events and counts as a function of load. A summary of representative results is shown in Figure 53, in which the accumulative number of events versus load is plotted for unidirectional notched and unnotched specimens. Although somewhat different curves are obtained for each of the six crack sizes, no consistent trend can be seen. Only the unnotched specimen is distinct; however, it should be noted that the width of the unnotched specimen is half that of the notched specimen. Figure 53 also demonstrates two additional effects which will be discussed later.

The results shown in Figure 53 have been replotted in Figure 54 with events presented as a function of the percentage of ultimate strength. Presenting the results in this form still shows no significant effect of crack length (or specimen expected strength) on AE activity, either in initiation of emissions or in slope or general shape of the curve. Note that the unnotched specimen data are no longer distinguishable from the notched specimen data. Other attempts to determine the desired correlation have not yielded any conclusive

information at this stage.

Returning to Figure 53, two additional aspects of the AE results are presented. First, a comparison of curves #6 and #3, obtained for specimens of similar crack size gripped with aluminum doublers as end tabs and with sanding paper, respectively, indicates that the latter clamping method produces substantially larger emission. This effect was discussed earlier in this Section. All specimens except #8 were tested using aluminum doublers as end tabs. Second, comparing curves #6 and #9, obtained for specimens of similar crack size with two different pre-set "windows" of "20" to "80" and "40" to "60", respectively, it can be seen that a fewer number of events is recorded with the narrower window, which is as expected. All test results except #9 were obtained with a pre-set "window" of "20" to "80".

In summary, the preliminary results presented here indicate that there is a potential for monitoring failure mechanisms through acoustic emission. The possibilities for application of this NDI technique as an indicator of material strength, e.g. an acceptance-rejection criterion, are inconclusive. However, the additional studies planned for the second phase of this program will hopefully clarify many aspects associated with the monitoring of acoustic emission in composite materials.

H. Failure Modes and Fracture Surfaces - As mentioned previously, the rapid changes in COD in the notched unidirectional B/Al specimen are due to fiber failure at the crack tip, which subsequently causes longitudinal plastic deformation and occasional splitting in the matrix. The final fracture surface is therefore fairly irregular, Figure 55a. A detailed description of this failure mechanism in unidirectional B/Al composites is given in [27,34]. No apparent difference between notched and unnotched specimens could be distinguished in terms of the general failure pattern, Figure 55a.

The failure process of the $[90]_8$ specimen is much simpler; in fact, a self-similar crack extension is observed, Figure 55b. The fracture surface appears to be fairly regular and coplanar for both notched and unnotched specimens. Matrix dominated failure is observed, as expected.

It was previously discussed in Section IV-A that the ultimate strength of unidirectional B/Al tested in this program is relatively low, and that a relatively large scatter in data has been observed. An attempt has been made to account for this low strength. The photomicrographs shown in Figure 56 reveal that the fiber volume fraction is approximately 48%. However, fiber distribution throughout the cross-section is not uniform. In some cases the fibers are in contact with each other and in other cases large spacing exists, up to half of a fiber diameter. The cross-sections shown in Figure 56 are typical of several specimens examined. These photomicrographs are, however, quite similar to others shown in the literature, therefore it is unlikely that the lack of uniformity in fiber distribution can be the source of the low strength values obtained in this work.

Scanning electron microscope (SEM) photographs were also taken. In order to obtain a better view of the fracture surfaces and better understand the different failure mechanisms, three-dimensional (stereo) views were obtained for both $[0]_8$ and $[90]_8$ notched and unnotched specimens. Stereo scanning electron micrographs of an unnotched unidreictional B/Al specimen (ultimate strength = 1303 MPa), Figure 57, indicate a very good fiber-matrix bond. The single fiber protruding from the matrix is coated with a substantial residue of aluminum, i.e. the shear strength of the bond exceeds that of the aluminum matrix. The good fiber-matrix bond is also manifested by the fact that many of the wedge-shaped fragments of shattered fibers, shown also in Figure 57a, are still embedded in the aluminum matrix despite the shock and sudden release of elastic energy during fracture. Very little fiber pull-out has been observed.

The few protruding fibers in Figure 57a (and in subsequent Figures) are exceptional and are shown here only to demonstrate the quality of the fiber-matrix bond. No matrix-matrix debonding has been observed, and the large amount of microvoid formation (local yielding of the aluminum matrix) appears to exemplify the increased degree of triaxial restraint which occurs as the matrix-matrix bonding is enhanced [62]. The substantial shattering of the fibers, Figure 57a, and breaking of the tungsten core seems to be limited to a few fiber-diameters along the length of the fibers. Figure 57b shows an overall view of a small section of the fracture surface, The small amount of fiber pull-out and the irergular pattern of the fracture surface (discussed earlier) are apparent.

The SEM photgraphs shown in Figure 58 were obtained from a similar unnotched specimen having an ultimate strength of 1469 MPa. Generally, no difference in the fracture surface morphology between the two specimens has been observed and the features described above appear for both the "weaker" and "stronger" specimens. The only difference is that the fracture surface of the "stronger" specimen is more regular. Figure 58 again demonstrates the good fiber-matrix bond; however, to examine the interfacial bond more accurately, an X-ray examination was performed on the fiber surface shown in Figure 58b using an energy dispersive X-ray analyzer on the SEM. The result of this examination, shown in Figure 59, demonstrates the presence of aluminum 6061 on the fiber surface, e.g. Al,Si,Mg lines.

As mentioned in Section IV-G, a notched unidirectional B/Al specimen was loaded to a predetermined level, approximately 40% of its expected ultimate strength, then unloaded and examined under the SEM after dissolving the outer foil of the aluminum matrix, Figure 60. (Photographs of the same specimen are also shown in Figure 35a. The crack tip is located at the left side of the photograph in both Figures.) Figure 60a shows a general view of the front layer of fibers, demonstrating again the nonuniformity of fiber distribution in the matrix. The broken fiber in the second layer is clearly seen, a detail of which

is shown in Figure 60b. Note the typical pattern of wedge-shaped fragments with their apexes pointing toward the original crack tip. The uppermost left fiber on the front layer shown in Figure 60a is broken due to the burn-out resulting from the electrical discharge machining process of the slit, and is also detailed in Figure 60b.

SEM photographs of notched and unnotched $[90]_8$ B/Al specimens are shown in Figure 61. Careful examination of the fracture surface of both specimens shows some irregularity in the specimen thickness direction, however it is limited to no more than one fiber diameter. The fibers shown in Figure 61a are practically clean of aluminum residue. Throughout the fracture surface only one split fiber has been found, and this was at the edge of the specimen where a complex state of stress exists just prior to failure. The split fiber shown in the photograph for the unnotched specimen, Figure 61b, is also the only one found throughout the fracture surface.

From the results obtained so far, no clear answer can be given in regards to the low strength values obtained for the material system studied in this program. The manufacturing process of this material seems to be adequate. The important aspect which has not yet been studied is the strength and scatter in strength of individual fibers. The fibers are already available and designated as to the plates for which they were used, and those tests will be performed in the second phase of this program.

I. Elevated Temperature Tests - In addition to the elevated temperature tests described in Section IV-D, a few tests were conducted to obtain the variation in stiffness and strength with temperature. In order to eliminate the effect of inherent material scatter, each of the specimens was first tested at room temperature for stiffness measurements, unloaded, heated to a predetermined temperature, and retested to failure. The results indicate that for unidirectional specimens, neither stiffness nor ultimate strength depend significantly on

temperature. These results do not agree with those reported elsewhere [63]. The results given in [63] indicate a 20% reduction in ultimate strength at 316°C (600°F). However, different failure modes have been observed in [63] which can be due to different material fabrication procedures and parameters, or different filament diameter, volume fraction, etc. The few tests results for notched strength at elevated temperatures also show no temperature dependency up to 204°C (400°F), Table IV. In any event, additional mechanical tests at elevated temperatures and a vigorous study of the basic failure modes will be necessary before reaching any firm conclusions.

The elevated temperature test results for the $[90]_8$ specimens indicate quite a strong dependency on temperature. At temperatures up to 204°C (400°F), stiffness is reduced by approximately 10% and strength by 20%. At 316°C (600°F) a significant reduction in both values has been recorded, i.e. 80% and 65% for stiffness and strength, respectively. These results agree well with the observations from the load-COD curves, Figure 21, and the local compliances, Figures 22 and 23, all of which indicate a variation in matrix properties at elevated temperatures. Thus, additional studies on this effect should be conducted.

# V. RESULTS AND CONCLUSIONS

In this progress report we have presented and analyzed experimental results on various aspects of the fracture behavior, deformation characteristics and failure modes of boron/aluminum composites. It has been demonstrated that the testing methodology employed in this program, namely the use of a variety of experimental techniques, is pertinent and even necessary to the study of a composite material system. A summary of the results presented in this report is given below:

1. Compliance curves: good correlation with predictions (energy release rate and COD) for unidirectional material. For the $[90]_8$ specimens, additional testing is required.

2. Calibration curves: isotropic width correction factor can be applied.

3. Fracture strength: results indicate relatively low unnotched strength for unidirectional material, while the $[90]_8$ specimens have the expected strength values.

4. Notched strength: concept of critical damage zone size can be applied.

5. Notch sensitivity: somewhat better than that obtained elsewhere for the same unidirectional boron/aluminum system. Very little notch sensitivity observed for $[90]_8$ specimens.

6. Elevated temperature tests: load-COD curves successfully obtained. Good control in applying high temperature strain gages.

7. Effects of elevated temperatures:

   a. very little effect on global properties of unidirectional specimens up to 600°F.

   b. significant effect on strength and stiffness of $[90]_8$ specimens.

   c. significant effect on local compliance curve of unidirectional material.

   d. significant effect on load-COD curves of unidirectional material.

   e. effects matrix-controlled failure mechanisms and crack tip damage growth in both laminates.

8. Fracture surface and crack tip damage:

   a. in unidirectional material, crack tip damage appears in the form of plastic deformation of the ductile matrix in the longitudinal direction. Prior to failure, multiple longitudinal plastic zones appear, accompanied by fiber failure, both of which result in irregular fracture surfaces for both notched and unnotched specimens.

   b. in $[90]_8$ specimens self-similar crack extension is observed; fracture surface is fairly regular and coplanar.

9. Failure modes:

   a. fracture surface morphology of unidirectional boron/aluminum does not reveal any dominant differences between "weak" specimens and "strong" specimens.

   b. a strong fiber-matrix interfacial bond exists with no fiber-matrix debonding in the unidirectional material.

c. the degree of fiber shattering indicates high elastic energy release at failure, and therefore high fiber loading.

d. no significant fiber pull-out is observed.

e. very good matrix-matrix bond is observed.

f. the fabrication process seems to be adequate, providing for good fiber-matrix bond, however, the irregular fiber spacing may be the cause of repeated acoustic emission during loading/unloading cycles.

g. the transverse strength is dominated by the matrix, with ductile failure of the 6061 alloy.

h. the irregular fiber spacing may be the cause of the irregular fracture surface in the specimen thickness direction for $[90]_8$ specimens.

i. practically no fiber splitting is observed in either unidirectional or transverse specimens.

j. fiber surfaces in the $[90]_8$ specimens are clean of any aluminum matrix residue.

10. Acoustic emission (AE) information obtained includes accumulative counts and events, count rate, location and amplitude distribution histograms, Cumulative Event Amplitude Distribution (CEAD) and counts per event, all in real-time.

11. Acoustic emission results include:

    a. potential for distinguishing between various failure mechanisms by means of AE characteristics.

    b. detection of initiation and progression of damage and of the failure site.

    c. a qualitative correlation between acoustic emission events (and counts) and deformation characteristics as detected in the load-displacement curves.

    d. during unloading/reloading cycles emission occurs in the early phase of unloading, and initiates again in the reloading stage prior to the previous load level.

    e. this early initiation of emission does not necessarily mean additional damage; existing damage is most probably the cause.

    f. attempts to use AE data for screening weak specimens have been inconclusive.

    g. significant effect of specimen gripping method on AE results is noted.

    h. data on accumulative counts are insufficient for determining material susceptibility to failure.

12. Acoustic emission potential exists as an NDI tool, however expectations will remain too high, encouraging skepticism, unless:

    a. basic studies are conducted on constituents and "simple" composite structures;

b. standardized laboratory test methodology is employed;

c. instrumentation is interfaced with data acquisition systems.

# VI. RECOMMENDATIONS

The results of this work indicate that elevated temperatures do possibly have an effect on the fracture behavior, deformation characteristics, failure modes, and microstructure of boron/aluminum composites. Also, the constituents (filament diameter and aluminum matrix alloy) may effect the local and global composite properties, fracture behavior, and notch sensitivity at room and elevated temperatures. The potential of some of the testing methods and concepts employed in this program deserve to be investigated in more detail. It is therefore our intent to pursue the following general subjects and directions during the second phase of this program.

1. A detailed study on the effect(s) of elevated temperatures on crack tip damage, damage growth, notch sensitivity, failure modes, damage mechanisms, etc.

2. All the described testing methodologies will continue to be applied.

3. In addition to the NDI test methods applied in this program, the potential application of other NDI techniques such as X-ray radiography and ultrasonic C-scan will also be explored.

4. Basic material properties at elevated temperatures will be included.

5. Basic constituent properties of different boron filament diameters and aluminum matrix alloys will be obtained.

6. Effect(s) of constituents on fracture behavior, notch sensitivity and failure modes will be included.

7. A study of various unidirectional boron/aluminum systems and boron/aluminum laminates will be included.

8. Investigation into the potential application of acoustic emission to damage detection will be continued:

   a. studies would be carried out on the constituents and "simple" composite structures to obtain "base-line" data.

   b. acoustic emission results will be compared with results from other NDI techniques such as X-ray radiography and ultrasonic C-scan, and correlated with load-displacement curves and failure mode examinations.

   c. the validity of the Kaiser and Felicity effects will be investigated.

   d. the potential of specific acoustic emission acceptance-rejection criteria will be explored.

   e. an attempt will be made to interface the acoustic emission instrumentation with the available data acquisition system to provide parametric analyses capabilities.

9. The effect of heat treatment, i.e. solution treatment and aging, of the aluminum alloy will be assessed with regard to notch sensitivity and transverse properties. This part of the program will be conducted at both room and elevated temperatures.

10. The microstructural variations in matrix, fiber, and interfacial failure with regard to test temperature, heat treatment, and various combinations of constituents will be examined via optical and electron microscopy techniques.

## VII. RESEARCH PARTICIPANTS

A. Participants - This research has been performed in the Department of Mechanical Engineering and Mechanics and in the Department of Materials Engineering. Dr. J. Awerbuch was the principal investigator, and collaborated with Dr. M. J. Koczak as research investigator, assisted by Mr. H. E. Perkinson, a graduate student in our department, as well as by three undergraduates (co-op and part-time students).

1. Principal Investigator - Dr. J. Awerbuch: Dr. J. Awerbuch was responsible for the overall execution of the research study in all phases of the program, including initial planning, experiments, analyses and reporting.

2. Research Investigator - Dr. M. J. Koczak: Dr. M. J. Koczak was responsible for the microstructural studies, primarily on the microscope and SEM examinations of failure mechanisms.

3. Graduate Assistant - Mr. H. E. Perkinson: Mr. H. E. Perkinson, after familiarizing himself with all aspects of the laboratory activities and organizing the laboratory for this project, conducted the actual experimental program in all its phases, including data reduction and analyses.

4. Student Assistants: The assistance of four undergraduate students, two as co-op (G. Kushnir and H. Rostami) and two as part-time students (W. Clark and S. Ellis) was required for the time-consuming processes of specimen preparation and data reduction schemes.

5. Technical Assistance provided by: J. Steinman, laboratory technical assistance; A. Seneca, laboratory supervision; D. Weber, illustration graphics; J. Trachtman, manuscript preparation.

B. Publications, Presentations and Research Activity:

1. J. Awerbuch

"Off-Axis Fatigue of Graphite/Epoxy Composites", (with H. T. Hahn). presented in the symposium on "Fatigue of Fibrous Composite Materials", sponsored by the ASTM D-30/E-9, May 22-23 1979, San Francisco, California. To appear in the Special Technical Publication.

"Effect of Constituents on Fracture Behavior of Unidirectional Boron/ Aluminum Composites", presented in the Symposium on "Fracture Modes in Metal Matrix Composites" in the 1980 annual meeting of the American Institute of Mining, Metallurgical and Petroleum Engineers (AIME), 24-28 February, 1980, Las Vegas, Nevada.

"Crack-Tip Damage and Fracture Toughness of BSiC/Ti Composites", (with H. T. Hahn), presented in the 1979 Spring meeting of the SESA, 20-25 May, 1979, San Francisco, California. To be published in Experimental Mechanics, October 1980.

"Deformation Characteristics and Failure Modes in Composite Materials", a seminar given in the Deutche Forschungs - und Versuchsanstalt für Luft-und Raumfahrt E.V. (DFVLR), Institute für Strukturmechanik, Braunschweig, Federal Republic of Germany, December 11, 1979.

"Fatigue Behavior of Unidirectional (On-Axis and Off-Axis) Graphite/Epoxy Composites", a seminar given in the Deutche Forschungs - un Versuchsanstalt für Luft - und Raumfahrt E.V. (DFVLR), Institute für Strukturmechanik, Braunschweig, Federal Republic of Germany, December 16, 1979.
Also presented in Laboratorium für Betribsfestigkeit (LBF), Darmstadt, Federal Republic of Germany, December 18, 1979.

"Impact Damage, Notch Sensitivity and Fracture Behavior of Composites", seminar given in Texas A & M University, November 28, 1979.
Also presented in DFVLR, Institute für Strukturmechanik, Braunschweig, Federal Republic of Germany, December 18, 1979.

"Impact Damage in Composites", in workshop on Principles of Fracture in Composite Materials, Deutche Forschungs - und Versuchanstalt für Luft - und Raumfahrt E.V. (DFVLR), Institute für Strukturmechanik, Braunschweig, Federal Republic of Germany, June 9-13, 1980.

Informal visits to Celanese, United Technology Research Center and DuPont Co. for Acoustic Emission Testing and Demonstrations.

Research Grant: "Deformation Characteristics and Failure Modes of Notched Graphite Polyimide Composites at Room and Elevated Temperatures", NASA Langley Research Center.

2. M. J. Koczak

Kim, W. H., Koczak, M. J. and Lawley, A.: "Effects of Isothermal and Cyclic Exposures on Interface Structure and Mechanical Properties of FP*-$\alpha$-$Al_2O_3$/Aluminum Composites in "New Developments and Applications in Composites", AIME, 1980.

Metal Matrix Composites, presented in Carpenter Technology, Reading, Pennsylvania, August 17, 1979.

Kim, W. H., Koczak, M. J. and Lawley, A.: Effects of Isothermal and Cyclic Exposures on Interface Structure and Mechanical Properties of FP*-$\alpha$-$Al_2O_3$/ Aluminum Composites in "New Developments and Applications in Composites", AIME Fall Meeting.

Pattnaik, A., Koczak, M. J. and Rogers, H. C.: Compressive Failure Behavior of FP*-$\alpha$-$Al_2O_3$/Aluminum Composites in "New Developments and Applications in Composites", AIME, 1980.

Skinner, A., Koczak, M. J. and Lawley, A.: "A Work of Fracture Study in Aluminum Matrix Composites", 1980 AIME Meeting, Las Vegas, February 1980, submitted to Met. Trans.

Research activity: other research activities based upon sponsorships from NASA and NRL contracts.

3. H. E. Perkinson

"Servo Hydraulic Equipment" a 5-day workshop conducted by Instron Corp., August 20-25, 1979, Canton, Mass.

"Strain Gage Principles and Applications", a 2-day workshop conducted by Measurement Group, September 26-27, 1979, Raleigh, N. C.

"Modern Strain Gage Instrumentation", a one-day workshop conducted by Measurement Group, September 28, 1979, Raleigh, N. C.

Informal visit to Celanese Corp., N. J. for Acoustic Emission Testing and Demonstration.

Research on Fracture Behavior, Failure modes, monitoring damage growth through acoustic emission and effect of constituents on fracture of boron aluminum composites at room and elevated temperatures.

EXPENDITURE

# AIR FORCE OFFICE OF SCIENTIFIC RESEARCH
## GRANT FISCAL REPORT

Submit in duplicate. Interim reports are required each year for grants of more than one year's duration. Submit final report as soon as possible but not more than 90 days after the end of the grant period.

| FROM: | TO: | REPORT DATE | GRANT NO. |
|---|---|---|---|
| Drexel University<br>32nd and Chestnut Streets<br>Philadelphia, PA 19104 | AFOSR/ PKD<br>Bldg 410<br>Bolling AFB, D.C. 20332 | 10/12/80 | AFOSR-<br>79-0079 |

| TYPE OF REPORT | REPORT PERIOD |
|---|---|
| [ ] FINAL [X] INTERIM | FROM: INCEPTION TO: May 31, 1980 |

| TOTAL PROJECT COST NEGOTIATED | TOTAL GRANT AMOUNT | AGREED PERCENT OF TOTAL PROJECT COST REPRESENTED BY GRANT AMOUNT |
|---|---|---|
| $ 73,232.32 | $ 72,500 | 99 % |

| DIRECT COSTS | [2]GRANT FUNDS EXPENDED |
|---|---|
| [1]SALARIES AND WAGES | |
| PRINCIPAL INVESTIGATOR | 2,626.00 |
| SENIOR SCIENTIFIC | 1,832.00 |
| OTHER | 15,544.36 |
| PERMANENT EQUIPMENT | -0- |
| EXPENDABLE SUPPLIES AND MATERIALS | 21,881.47 |
| TRAVEL | 2,058.44 |
| PUBLICATION COSTS | 451.04 |
| COMPUTER COSTS | -0- |
| EMPLOYEE BENEFITS | 757.86 |
| OTHER (Specify) | 681.70 |
| TOTAL DIRECT COSTS | 45,832.87 |
| INDIRECT COSTS: 43.7 % OF 20,760.22 | 9,072.22 |
| TOTAL GRANT FUNDS EXPENDED | 54,905.09 |
| I CERTIFY THAT THE PRINCIPAL INVESTIGATOR(S) HAS (HAVE) DEVOTED APPROXIMATELY _____ % OF HIS (THEIR) TIME TO PERFORMANCE OF THE RESEARCH UNDER THE GRANT. I FURTHER CERTIFY THAT THIS FISCAL REPORT IS CORRECT; THAT ALL EXPENDITURES REPORTED WERE FOR APPROPRIATE PURPOSES; AND THAT THE GRANTEE HAS EXPENDED FROM NON-FEDERAL FUNDS IN THE COST CATEGORIES LISTED ABOVE, IN PERFORMANCE OF THE RESEARCH UNDER THIS GRANT, THE AMOUNT OF | -0- |
| TOTAL ACTUAL PROJECT COST FOR REPORT PERIOD | 54,905.09 |
| ON FINAL FISCAL REPORT ONLY:<br>IF ACTUAL TOTAL PROJECT COST IS LESS THAN NEGOTIATED TOTAL PROJECT COST, MULTIPLY THE ACTUAL TOTAL PROJECT COST BY THE AGREED PERCENTAGE REPRESENTED BY THE GRANT AMOUNT AND ENTER RESULT HERE. *(NOTE: Regardless of the above computation, any unexpended or uncommitted grant funds must be returned to AFOSR in accordance with the paragraph of the Grants Brochure "Unexpended Funds and Earned Interest")* | |
| DEDUCT THIS AMOUNT FROM TOTAL GRANT AMOUNT | |
| ADD INTEREST EARNED | |
| REFUND DUE *(return this amount with the final report by check made payable to the Treasurer of the United States)*<br>AFOSR EOSR, NPO, BOLLING AFB | |

| SIGNED | TITLE |
|---|---|
| | Joseph J. Ragg<br>Comptroller |

[1] If the actual cost in this category varies more than 10% from the estimate, provide an explanation of the variance on the reverse of this form.

[2] Firm outstanding commitments are considered as costs.

AFOSR FORM MAR 75 2

AFM [illegible] 410 Mar 1975

## REFERENCES


1. K. M. Prewo, "Exploratory Development of Low-Cost Primary Fabrication Processes for Boron-Aluminum Composites," AFML-TR-74-40 Air Force Materials Laboratory, March 1974.

2. E. L. Foster, Jr., "Technology Development of Metal Matrix Composites for DOD Application Requirements," proceedings of First MMC Workshop, Institute of Defense Analysis, Paper P-1144, September 1975.

3. A. R. Robertson, "Manufacturing Methods for Metal Matrix Structural Components," AFML-TR-76-140 Air Force Materials Laboratory, August 1976.

4. K. M. Prewo and K. G. Kreider, "High Strength Boron and Borsic Fiber Reinforced Aluminum Composites," J. Composite Materials, Vol. 6, July 1972, pp. 338-357.

5. K. M. Prewo and K. G. Kreider, "The Transverse Tensile Properties of Boron Fiber Reinforced Aluminum Matrix Composites," Metallurgical Transactions, Vol. 3, 1972, pp. 2201-2211.

6. I. J. Toth, "An Exploratory Investigation of the Time Dependent Mechanical Behavior of Composite Materials," AFML-TR-69-9, Air Force Materials Laboratory, April 1969.

7. G. D. Menke and I. J. Toth, "The Time Dependent Mechanical Behavior of Metal Matrix Composites," AFML-TR-71-102, Air Force Materials Laboratory, Sept. 1971.

8. K. M. Prewo and K. G. Kreider, "Fatigue Failure Mechanism in Boron Aluminum," Failure Modes in Composites, I. J. Toth Edt., The Metallurgical Society of the AIME, Vol. I, New York, New York, 1972, pp. 395-413.

9. C. T. Herakovich, J. G. Davis, Jr. and C. N. Viswanatharns, "Tensile and Compressive Behavior of Borsic/Aluminum," Composite Materials: Testing and Design (Fourth Conference), ASTM STP 617, American Society for Testing and Materials, 1977, pp. 344-357.

10. C. T. Herakovich, J. M. Kennedy and D. R. Tenney, "Effect of Cyclic Loading and Temper Condition on the Tensile Behavior of Boron-Aluminum," Proceedings of Conference: Environmental Degradation of Engineering Materials, College of Engineering, Virginia Tech., 1977, pp. 331-343.

11. K. G. Kreider and L. Dardi, "Fracture Toughness of Composites," Failure Modes in Composites, I. J. Toth Edt., The Metallurgical Society of the AIME, Vol. I, New York, New York, 1972, pp. 193-220.

12. J. W. Mar and K. Y. Lin, "Fracture Mechanics Correlation for Tensile Failure of Filamentary Composites with Holes," J. of Aircraft, Vol. 14, No. 7, July 1977, pp. 703-704.

13. M. A. Wright and F. A. Iannuzzi, "The Failure of Notched Specimens of Boron-Fiber Reinforced 6061 Aluminum Alloy," Failure Modes in Composites, Vol. II, New York, New York, 1974, pp. 68-94.

14. M. E. Waddoups, J. R. Eisenmann and B. E. Kaminski, "Macroscopic Fracture Mechanics of Advanced Composite Materials," J. Composite Materials, Vol. 5, 1971, pp. 446-454.

15. J. M. Whitney and R. J. Nuismer, "Stress Fracture Criteria for Laminated Composites Containing Stress Concentrations", J. Composite Materials, Vol. 8, 1974, pp. 253-265.

16. J. R. Hancock and G. D. Swanson, "Toughness of Filamentary Boron/Aluminum Composites," Composite Materials: Testing and Design (Second Conference), ASTM STP 497, American Society for Testing and Materials, 1972, pp. 299-310.

17. C. T. Sun and K. M. Prewo, "The Fracture Toughness of Boron Aluminum Composites," J. Composite Materials, Vol. II, 1977, pp. 164-175.

18. W. R. Hoover and R. E. Allred, "The Toughness of Borsic-Aluminum Composites With Weak Fiber Matrix Bonds," Failure Modes in Composites, I. J. Toth Edt., The Metallurgical Society of the AIME, Vol. I, New York, New York, 1972, pp. 311-326.

19. K. M. Prewo and K. G. Kreider, "Fatigue Failure Mechanism in Boron Aluminum," Failure Modes in Composites, I. J. Toth Edt., The Metallurgical Society of the AIME, Vol. I, New York, New York, 1972, pp. 395-413.

20. J. H. Underwood, "Crack-Tip Deformation Measurements Accompanying Fracture in Fibrous and Laminar Composites," Composite Materials Testing and Design (Third Conference), ASTM STP 546, American Society for Testing and Materials, 1974, pp. 376-394.

21. D. L. McDanels and R. A. Signorelli, "Effect of Fiber Diameter and Matrix Alloys on Impact-Resistant Boron/Aluminum Composites," NASA-TN D-8204.

22. K. M. Prewo, "Development of Impact Resistant Metal Matrix Composites," AFML-TR-216, Air Force Materials Laboratory, March, 1976.

23. D. L. McDanels and R. A. Signorelli, "Effect of Angle Plying and Matrix Enhancement on Impact-Resistant Boron/Aluminum Composites," NASA TN D-8205 October 1976.

24. J. E. Alexander and R. G. Carlson, "Failure Processes in Metal Matrix Composites," AFML-TR-73-290, Air Force Materials Laboratory, 1973.

25. M. A. Wright and F. A. Iannuzzi, "The Failure of Notched Specimens of Boron-Fiber Reinforced 6061 Aluminum Alloy," Failure Modes in Composites, J. N. Fleck and R. L. Mehan, Eds., The Metallurgical Society of the AIME, Vol. II, New York, New York, 1974, pp. 68-94.

26. J. Awerbuch, "Effect of Constituents on Fracture Behavior of Unidirectional Boron Aluminum Composites," presented in the symposium on "Fracture Modes in Metal Matrix Composites," the 1980 Annual Meeting of the AIME Las Vegas, Nevada, February 24-28, 1980, to be published.

27. J. Awerbuch, "Fracture Behavior of Boron Aluminum and Borsic Titanium Composites," to appear as Air Force Materials Laboratory Technical Report, 1981, also is an AFOSR Progress Report under Grant No. 79-0079, April 1980.

28. J. Awerbuch, "Notch Sensitivity of Boron Laminate," to be published.

29. J. Awerbuch and H. T. Hahn, "K Calibration of Unidirectional Metal Matrix Composites," J. Composite Materials, Vol. 12, 1978, pp. 222-237.

30. W. N. Sharpe, Jr., "Preliminary Development of an Interferometric Strain Gage for Use on Nosetip Materials Subjected to Thermal Shock," AFML-TR-76-63 Air Force Materials Laboratory, 1976.

31. F. A. Jenkins and H. E. White, Fundamentals of Optics, McGraw-Hill, New York, 1957.

32. D. E. Macha, W. N. Sharpe, Jr. and A. F. Grant, Jr., "A Saser Interferometry Method for Experimental Stress Intensity Factor Calibration," ASTM STP 601, American Society for Testing and Materials, 1976, p. 490.

33. W. N. Sharpe, Jr., "Interferometric Surface Strain Measurement," International Journal of Nondestructive Testing, Vol. 3, 1971, p. 56.

34. J. Awerbuch and H. T. Hahn, "Crack Tip Damage and Fracture Toughness of Boron/Aluminum Composites," J. Composite Materials, Vol. 13, 1979, pp. 82-107.

35. J. Awerbuch and H. T. Hahn, "Crack Tip Damage and Fracture Tougness of Borsic/Titanium Composites," Experimental Mechanics, October 1980, pp. 334-344.

36. J. Awerbuch, "Deformation Characteristics and Failure Modes of Graphite/Polyimide Composites at Room and Elevated Temperatures," Progress Report, NASA Langley Research Center, October 1980.

37. J. Awerbuch, "Deformation Characteristics and Failure Modes of Center Notched Graphite/Epoxy Laminates," to be published.

38. B. W. Rosen, "A Simple Procedure for Experimental Determination of the Longitudinal Shear Modulus of Unidirectional Composites," J. Composite Materials, Vol. 6, 1972, pp. 552-554.

39. C. D. Bailey, J. M. Hamilton, Jr., and W. M. Pless, "Acoustic Emission of Impact-Damaged Graphite-Epoxy Composites," Materials Evaluation, pp. 43-54, May 1979.

40. J. T. Ryder and J. R. Wadin, "Acoustic Emission Monitoring of a Quasi-Isotropic Graphite/Epoxy Laminate Under Fatigue Loading," Lockheed-California and Dunegan/Endevco Companies, Internal Report.

41. M. A. Hamstad,"Variabilities Detected by Acoustic Emission from Filament-Wound Aramid Fiber/Epoxy Composite Pressure Vessels," International Instrumentation Symposium, Vol. 24, pp. 419-431, 1978.

42. J. M. Carlyle, "Imminent Fracture Detection in Graphite/Epoxy Using Acoustic Emission," Experimental Mechanics, pp. 191-195, May 1978.

43. R. L. Randall and L. J. Graham, "Acoustic Emission Characterization Systems," International Instrumentation Symposium, pp. 439-444, 1978.

44. A. Arora and K. Tangeri, "On Methods of Structural Integrity Evaluation by Acoustic Emission," Int. J. of Fracture, Vol. 15, 1979.

45. R. G. White and H. Tretout, "Acoustic Emission Detection Using a Piezoelectric Strain Gauge for Failure Mechanism Identification in CFRP," Composites, pp. 101-109, 1979.

46. T. J. Fowler, "Acoustic Emission Testing of Fiber Reinforced Plastic Equipment," ASME Design Engineering Conference, Chicago, May 1979.

47. T. J. Fowler and E. Gray, "Development of an Acoustic Emiss n Test for FRP Equipment," ASCE Winter Convention, Boston, April 2-6, 1979, preprint 3583.

48. W. F. Brown and J. E. Srawley, in "Plane Strain Crack Toughness of High Strength Metallic Materials," ASTM STP 410, American Society of Testing and Materials, 1966, p. 11.

49. G. C. Sih and H. Liebowitz, "Mathematical Theories of Brittle Fracture," in Fracture, Vol. 2, 3d. H. Liebowitz, Academic Press, N. Y., 1968.

50. S. G. Lekhnitskii, Theory of Elasticity of an Anisotropic Elastic Body, Translated by P. Fern, Holden-Day Inc., 1963.

51. S. G. Lekhnitskii, Anisotropic Plates, Translated by S. W. Tsai and T. Cheron, Gordon and Breach Science Publishers, N. Y., 1968.

52. I. M. Daniel, R. E. Rowlands and J. B. Whiteside, "Deformation and Failure of Boron/Epoxy Plate with Circular Holes," The Test Methods for High Modulus Fibers and Composites, ASTM STP 521, American Society for Testing and Materials, 1973, p. 143.

53. M. E. Waddoups, J. R. Eisenmann and B. E. Kaminski, "Macroscopic Fracture Mechanics of Advanced Composite Materials," J. Composite Materials, Vol. 5 1971, p. 446-454.

54. R. J. Nuismer and J. M. Whitney, "Uniaxial Failure of Composite Laminates Containing Stress Concentrations," in Fracture Mechanics of Composites, ASTM STP 593, American Society of Testing and Materials, 1975 pp. 117-142.

55. Y. T. Yeow, D. H. Morris and H. F. Brimson, "A Correlation Study Between Analysis and Experiments on the Fracture Behavior of Graphite/Epoxy Laminates," Virginia Polytechnic Institute and State University, VPI-E-77-20, 1977.

56. Y. T. Yeow, D. H. Morris, H. F. Brinson, "A Study of Damage Zones or Characteristic Lengths Related to the Fracture Behavior of Graphite/Epoxy Laminates," Virginia Polytechnic Institute and State University, VPI-E-77-15, 1977.

57. R. B. Pipes, J. W. Gillespie, Jr., and R. C. Wetherhold, "Superposition of the Notched Strength of Composite Laminates," Polymer Engineering and Science, Vol. 19, No. 16, 1979, pp. 1151-1155.

58. J. W. Mar, "Fracture and Fatigue of B-Materials," Mechanics of Composite Review, Air Force Materials Laboratory, Dayton, Ohio, Oct. 1976, p. 117.

59. J. W. Mar and K. Y. Lin, "Fracture of Boron/Aluminum Composites with Discontinuities," J. Composite Materials, Vol. 11, 1977, pp. 405-421.

60. "Measuring the Slope of Amplitude Distributions," Dunegan/Endevco Product Information Note, PIN-4, 1978.

61. J. Kaiser, "Undersuchungen Uber das Auftreten von Gerauschen beim Zugversuch," Dr.-Ing. Thesis, Technische Hochschule, Munich, 1950.

62. R. C. Jones, "Fractography of Aluminum-Boron Composites," Composite Materials: Testing and Design (Second Conference), ASTM STP 497, American Society for Testing and Materials, 1972, pp. 439-468.

63. G. D. Menke, I. J. Toth, "The Time Dependent Mechanical Behavior of Metal Matrix Composites," AFML-TR-71-102, Air Force Materials Laboratory, September 1971.

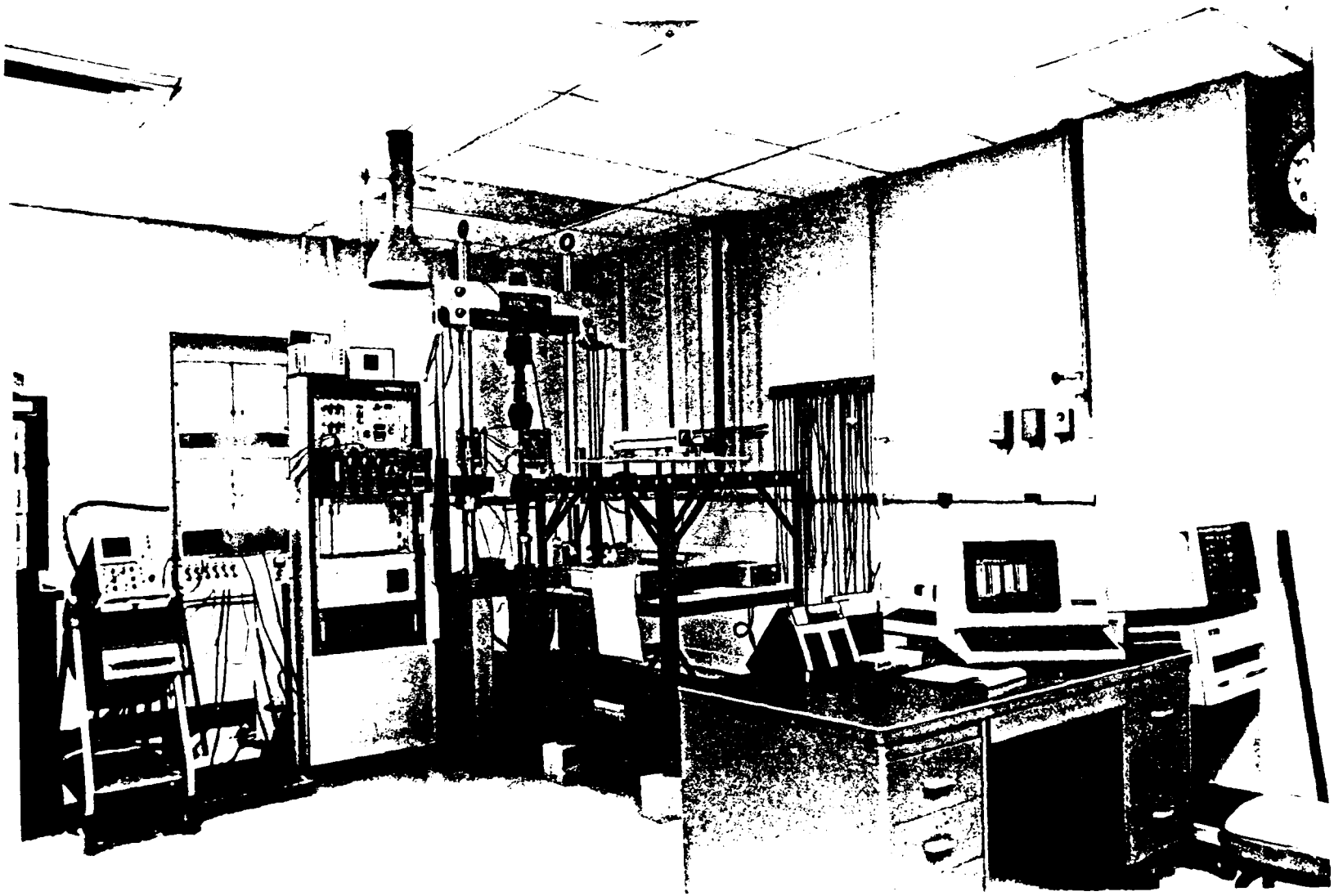

Figure 1. A general view of the testing facilities.

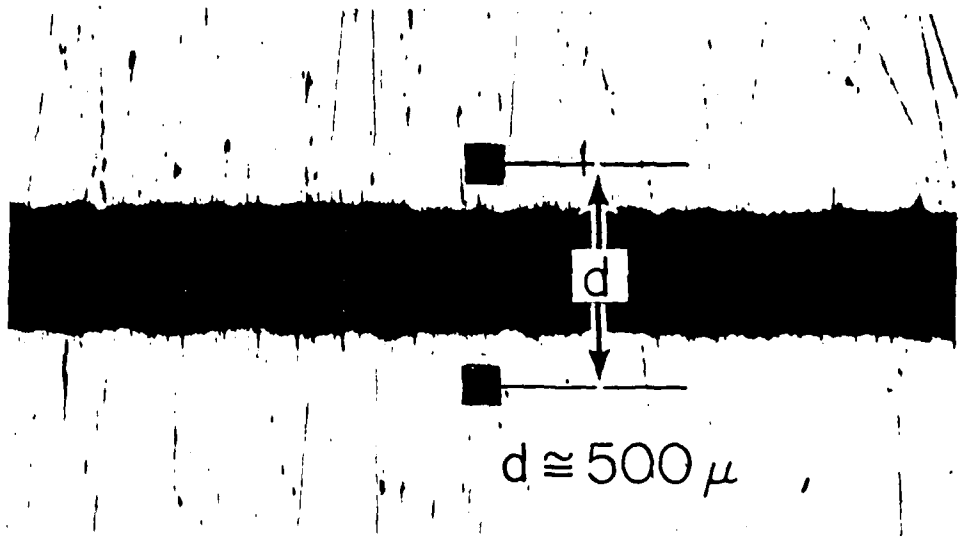


Figure 2. Photomicrograph of two indentations located at the center of the crack.

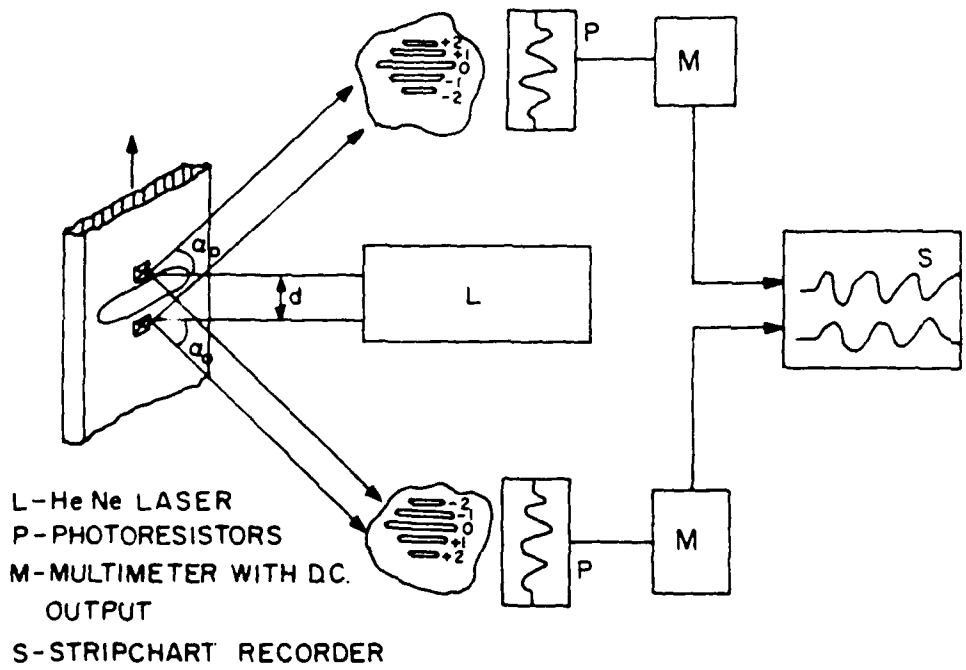


Figure 3. Schematic view of the laser interferometry displacement technique. Nominal value of d is 0.5 mm and $\alpha_o$ is typically 42°.

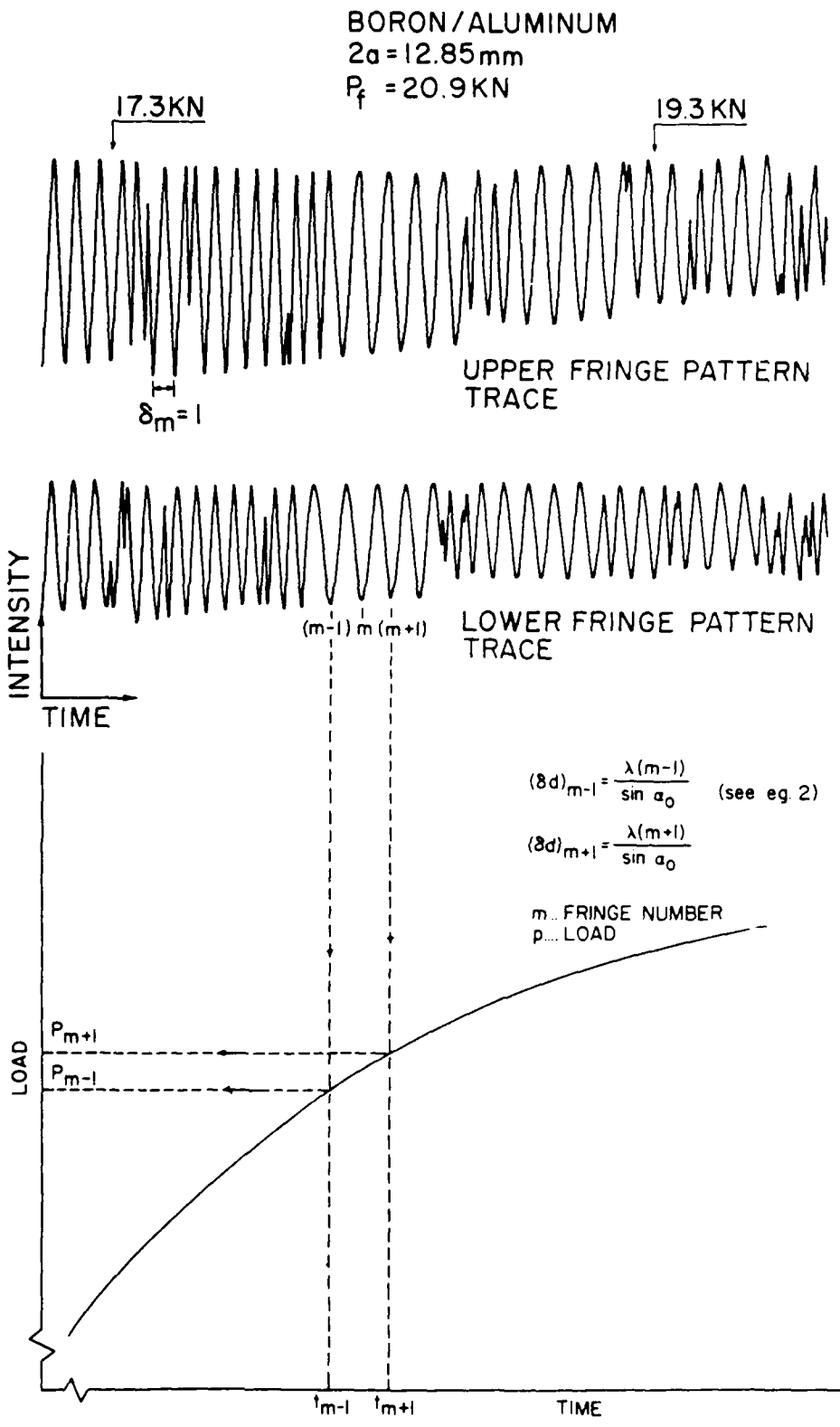


Figure 4. A schematic view of data reduction from the IDG records.

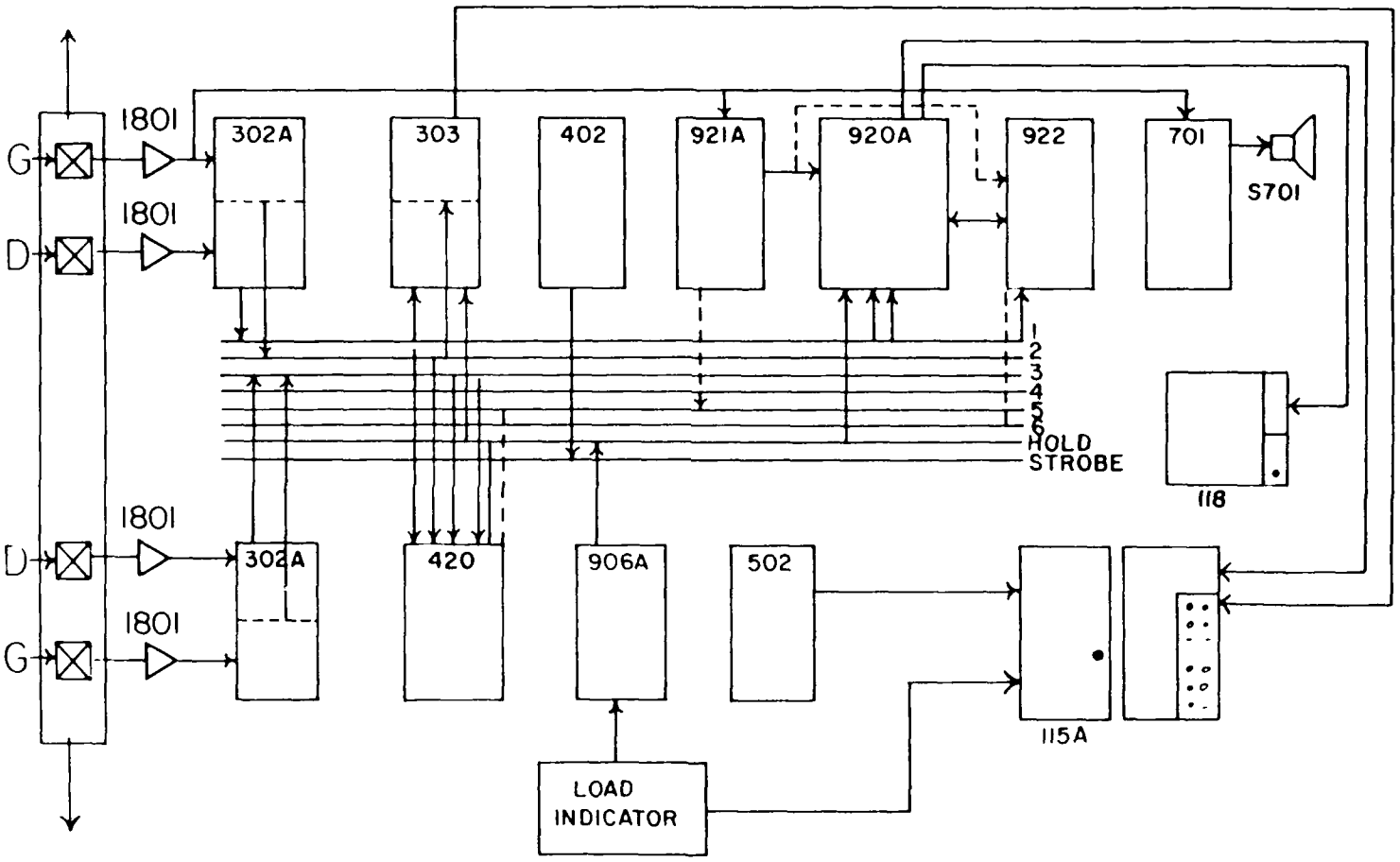


Figure 5. Block diagram of the Dunegan/Endevco 3000 acoustic emission system.

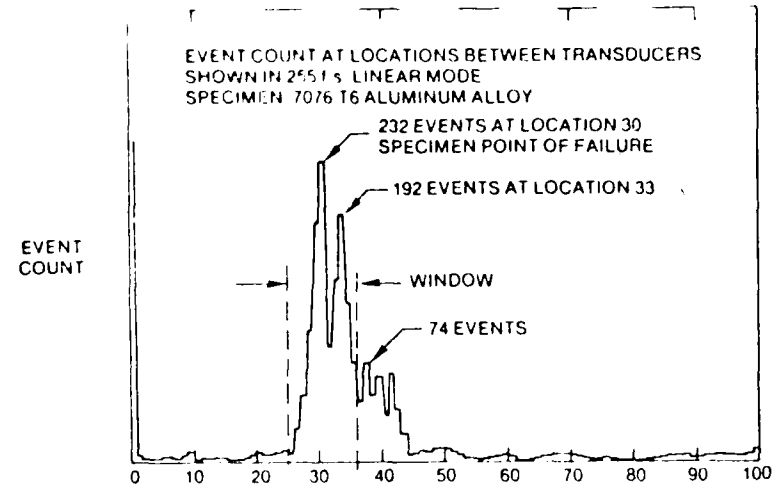


Spatial Distribution of Events

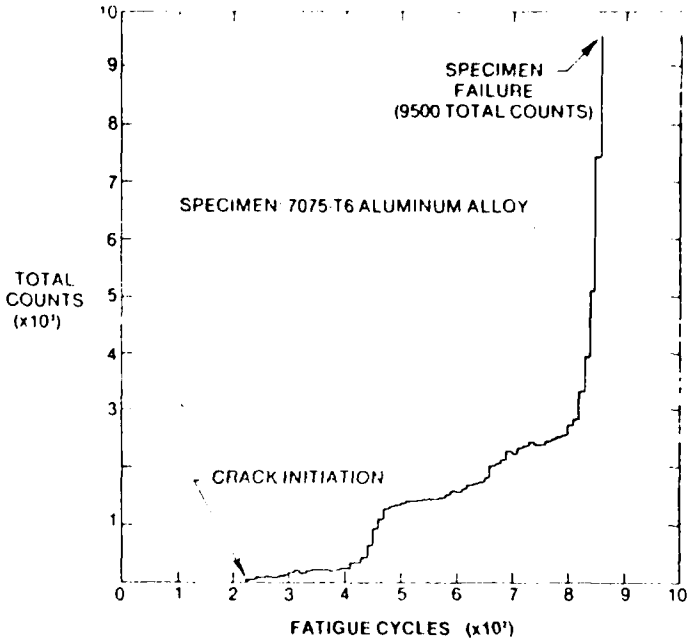


Total Counts as a Function of Fatigue Cycles

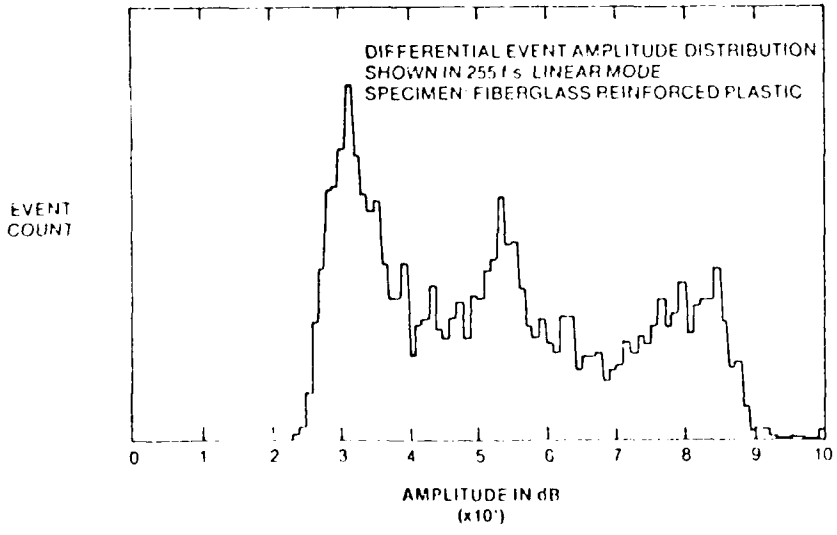


Amplitude Distribution

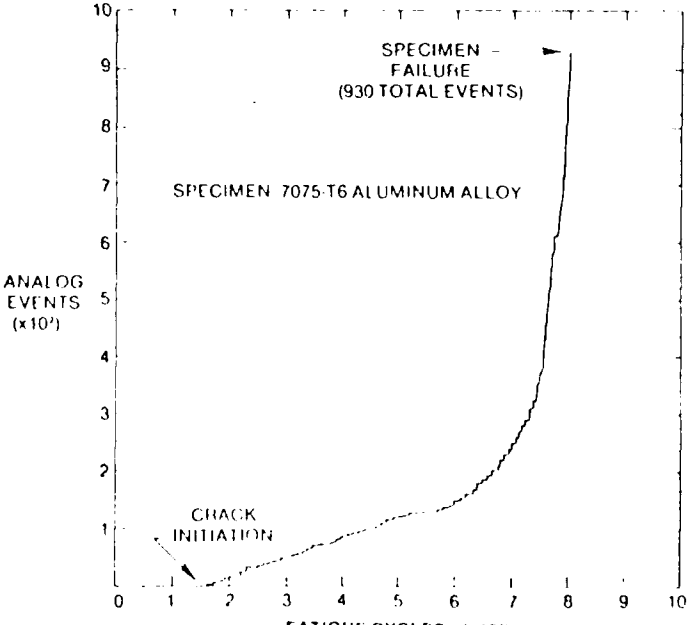


Analog Events as a Function of Fatigue Cycles

Figure 6. Schematics of location and amplitude distribution histograms and accumulative counts and events diagrams [920A Manual].

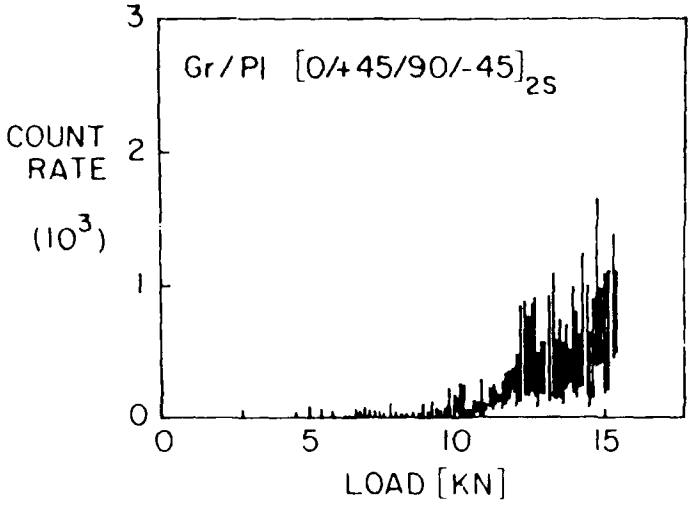


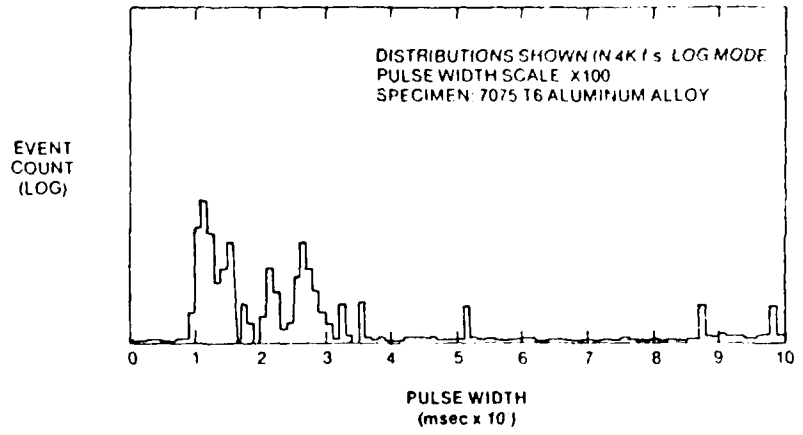


Pulse Width Distribution

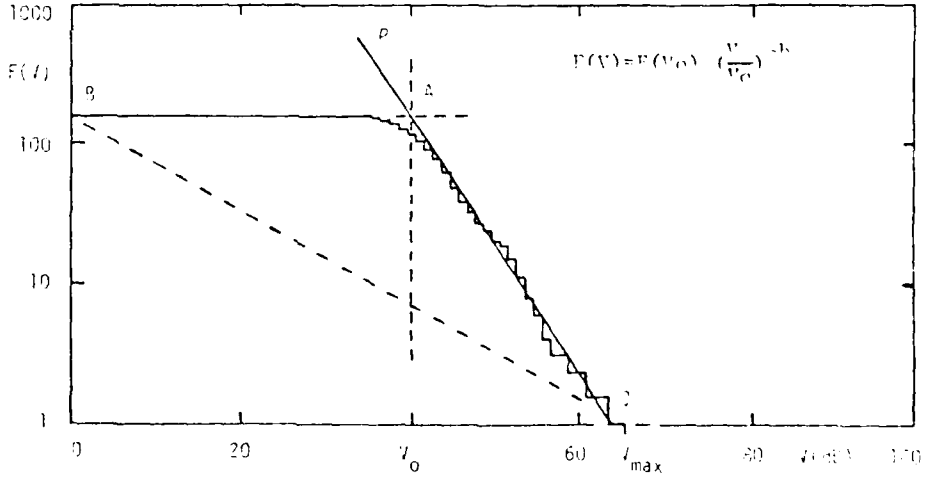


Cumulative Event Amlitude Distribution

Figure 7. Schematics of pulse width distribution histograms, count rate and Cumulative Event Amplitude Distribution (CEAD) diagrams [920A Manual].

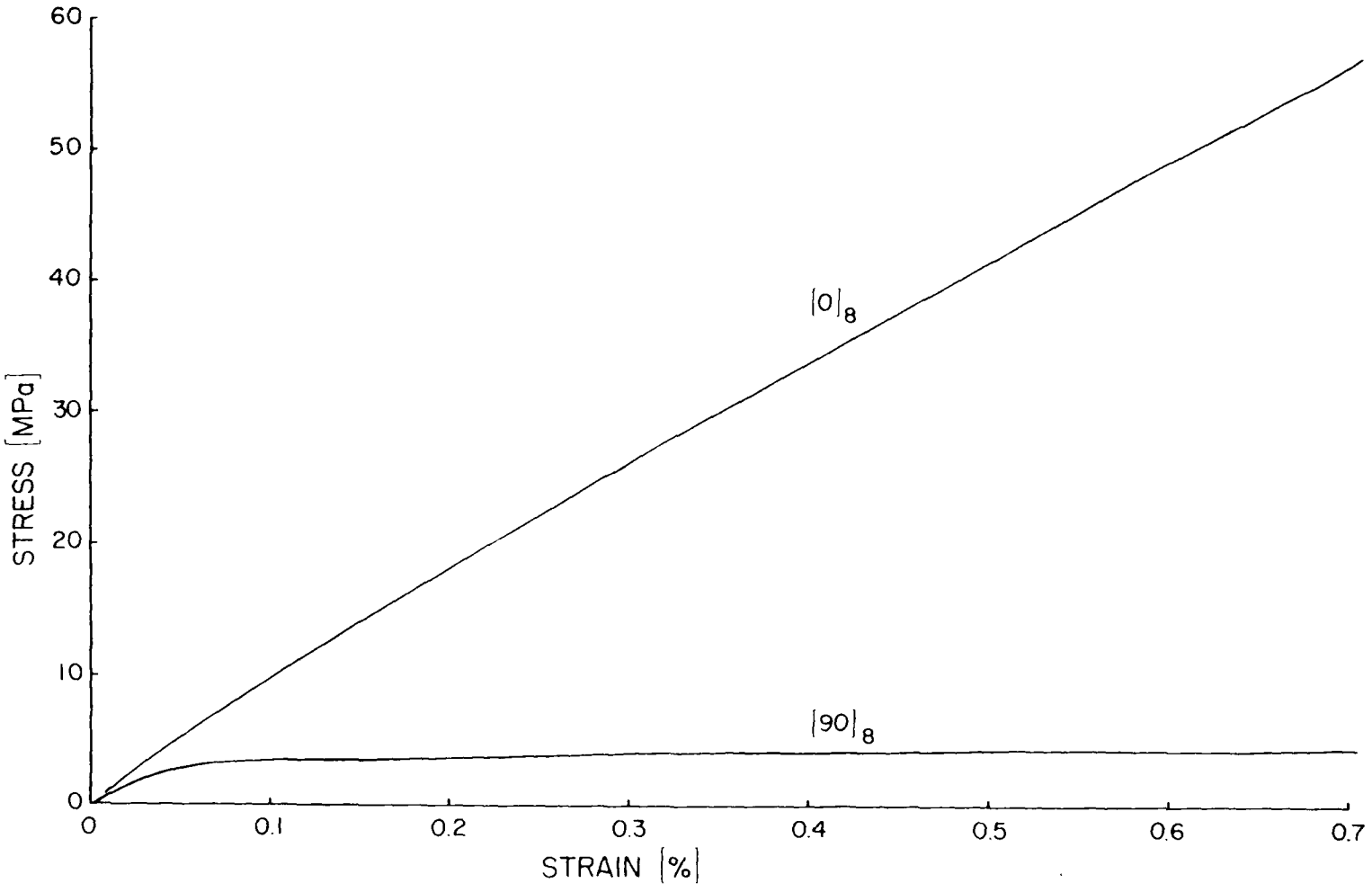


Figure 8. Stress-strain curves for $[0]_8$ and $[90]_8$ 5.6 mil. B/Al 6061F.

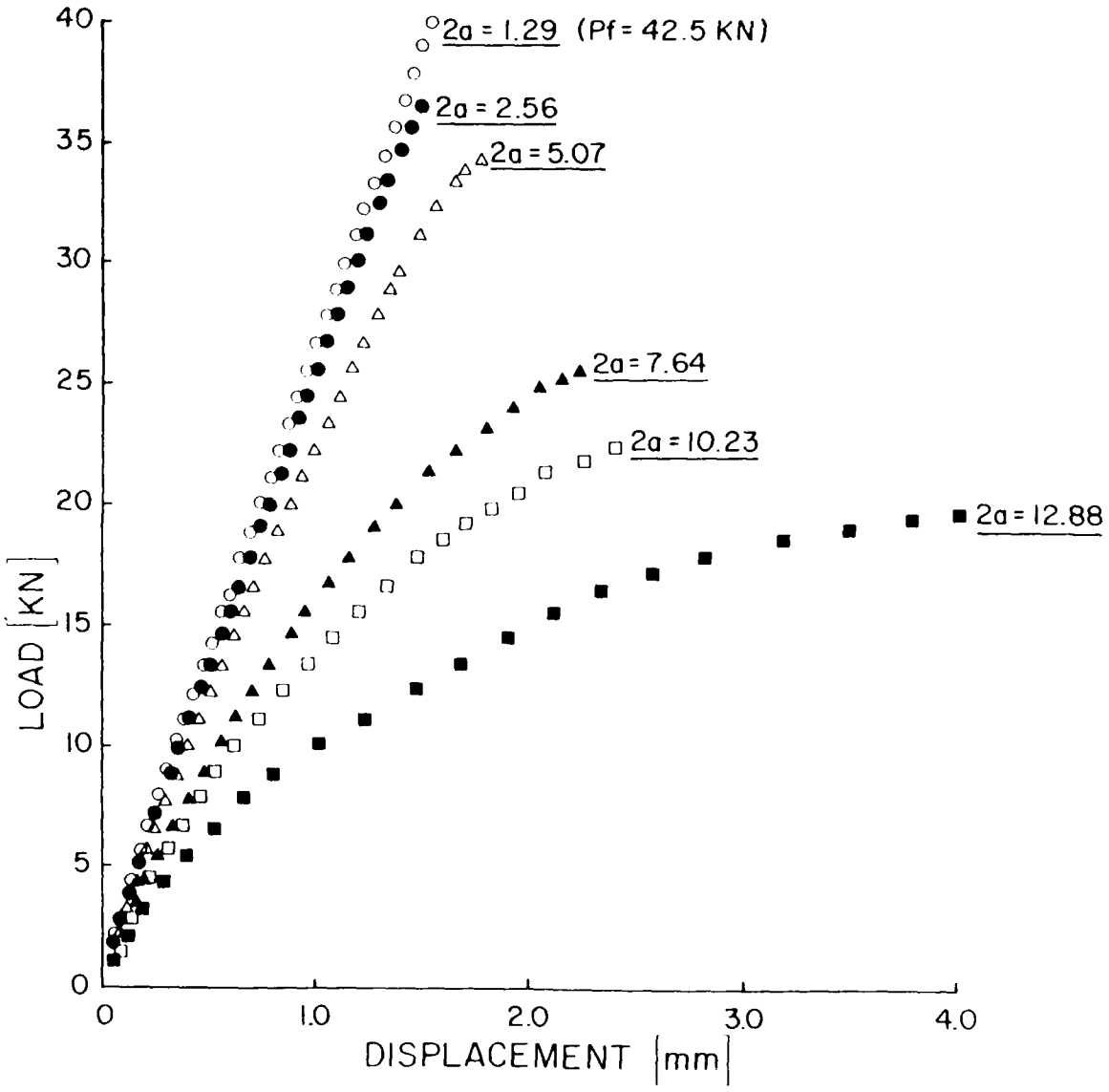


Figure 9. Far-field load-displacement curves for unidirectional 5.6 mil B/Al 6061F specimens for various crack lengths obtained with the compliance gage.

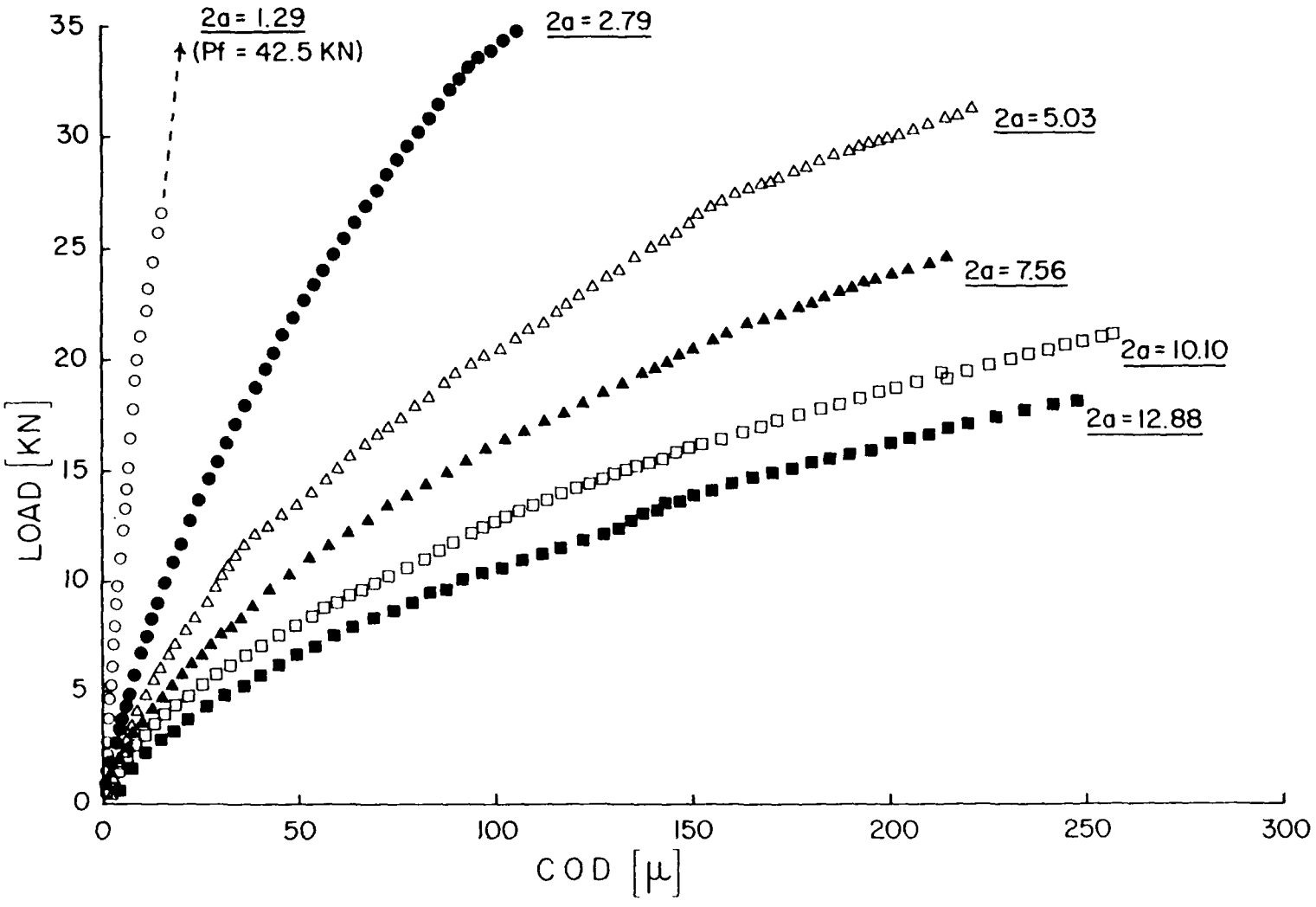


Figure 10. Load-COD curves for unidirectional 5.6 mil B/Al-6061F specimens for various crack lengths obtained with the IDG.

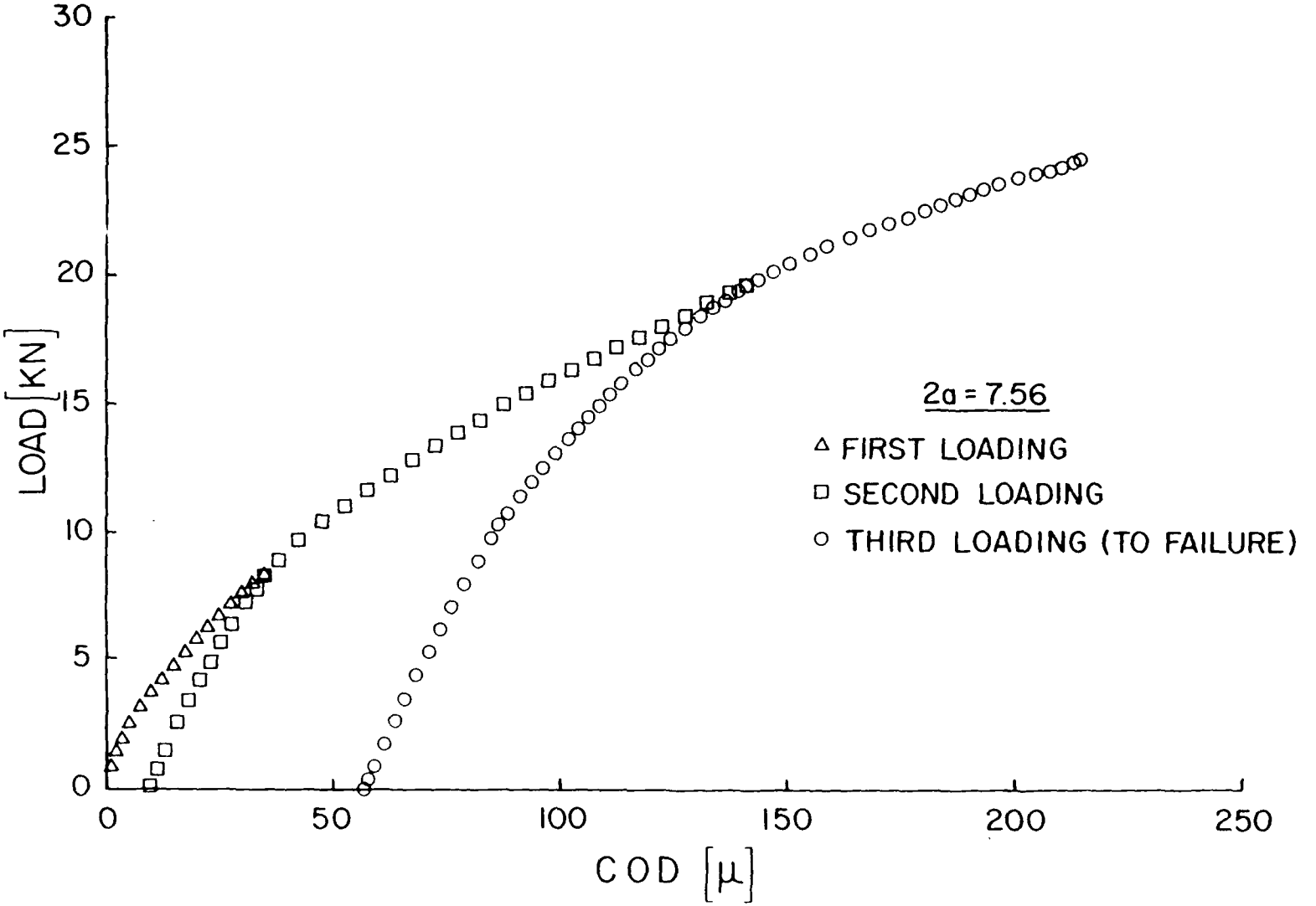


Figure 11. *Load-COD (loading-unloading) curves for unidirectional 5.6 mil B/Al-6061F specimens obtained with IDG (crack length = 7.56 mm).*

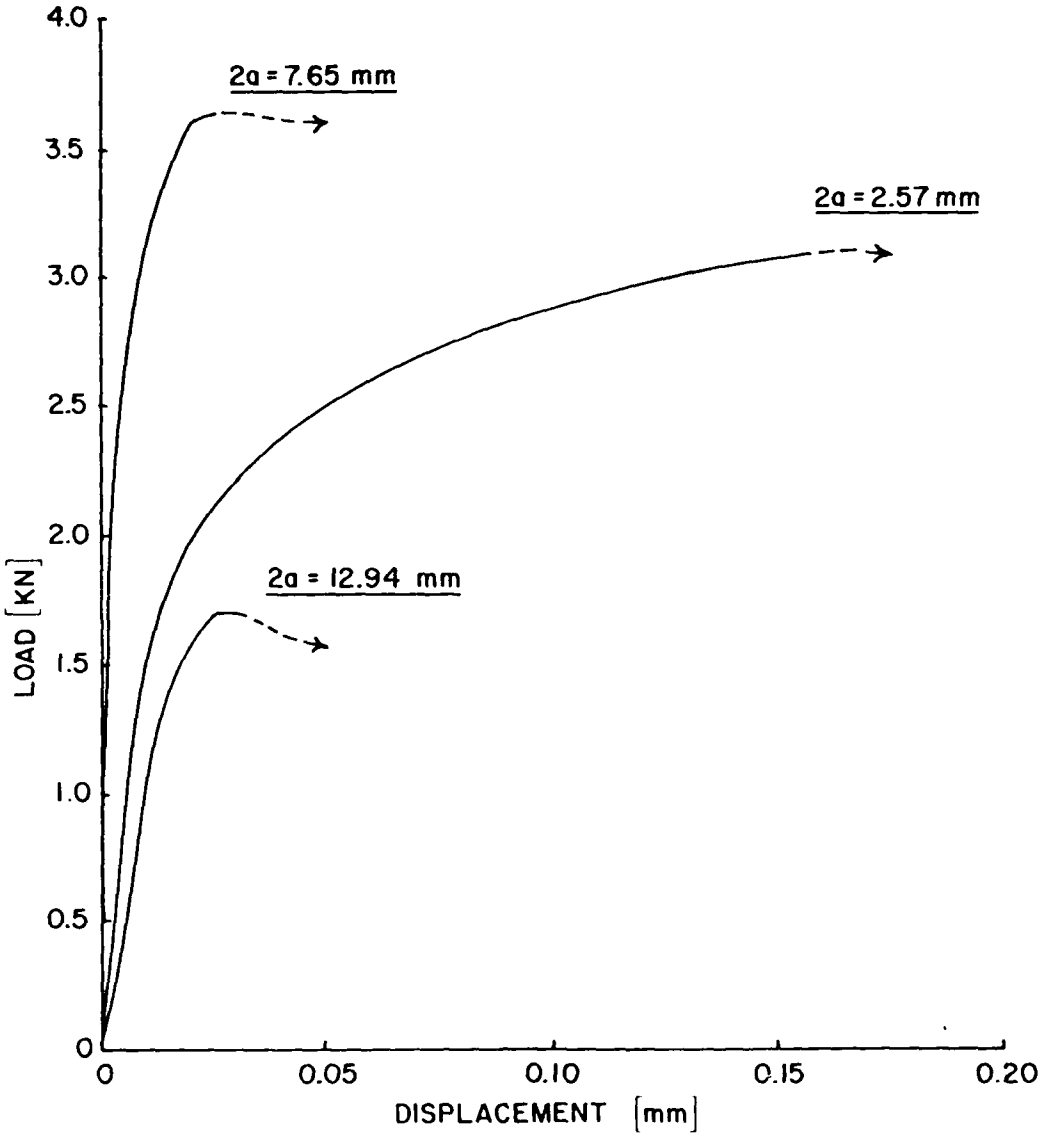


Figure 12. Far-field load-displacement curves for $[90]_8$ 5.6 mil B/Al-6061F specimens for various crack lengths obtained with the compliance gage.

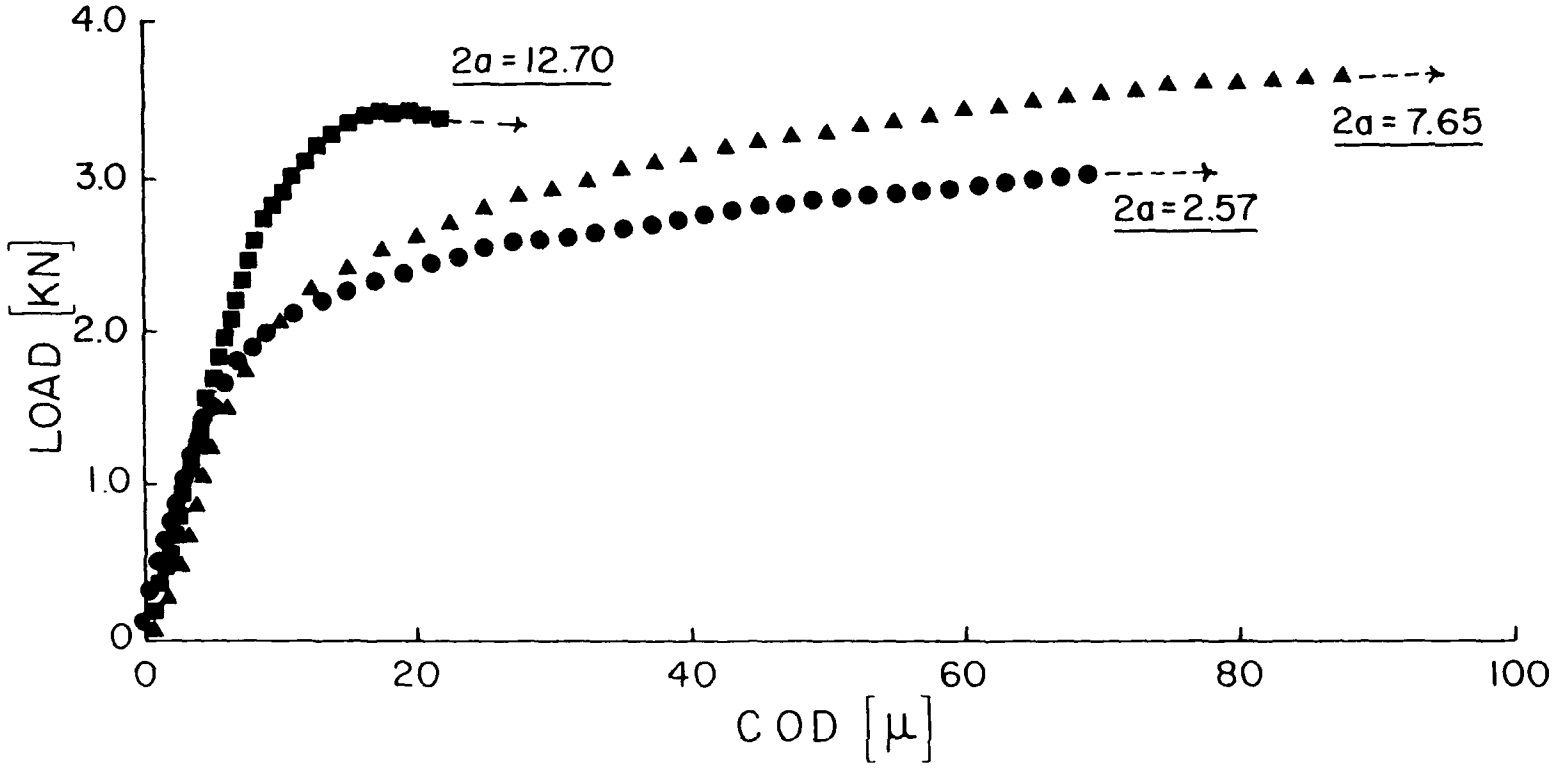


Figure 13. Load-COD curves for $[90]_8$ 5.6 mil B/Al-6061F specimens for various crack lengths obtained with the IDG.

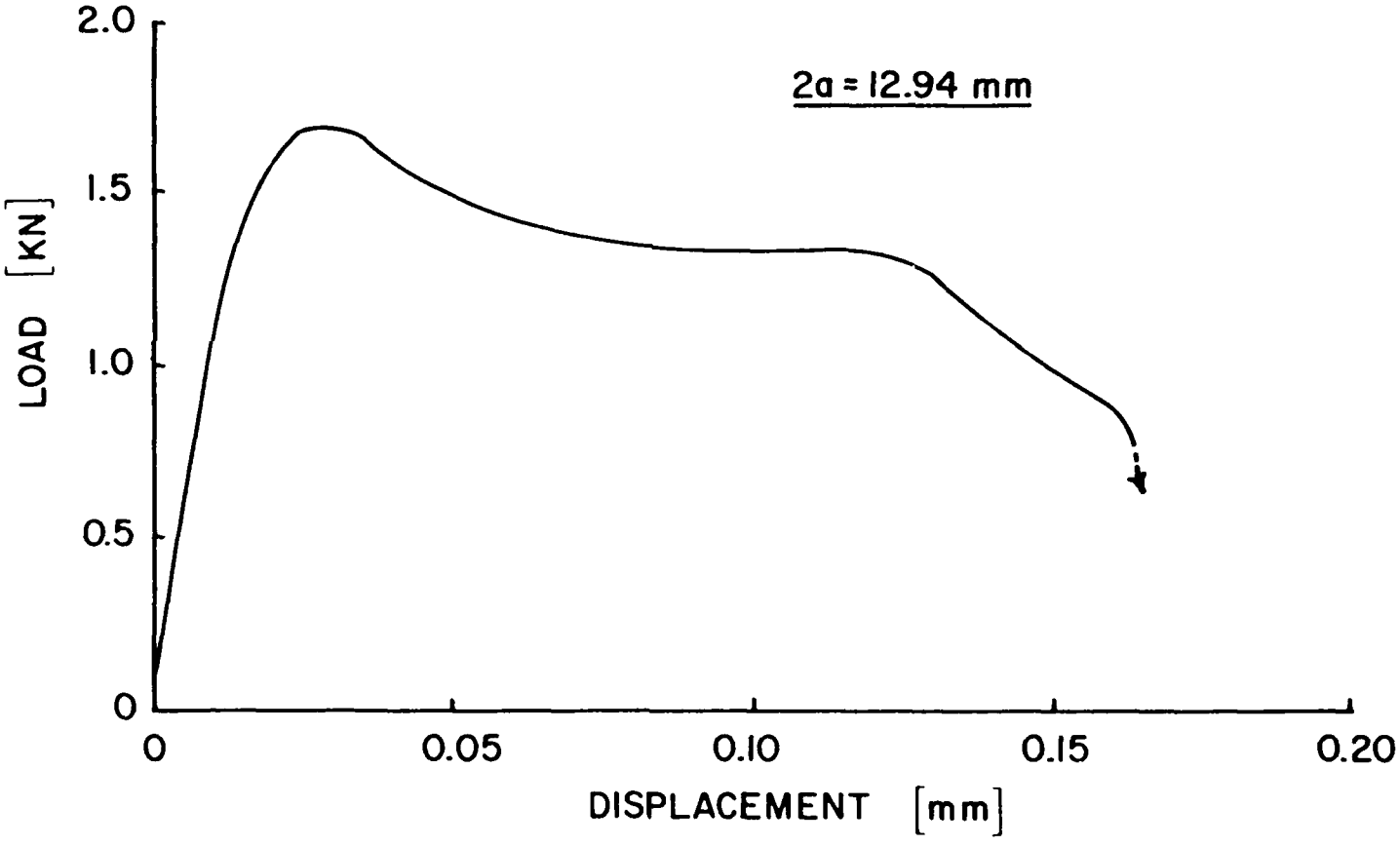


Figure 14. Detail of far-field load-displacement curve for $[90]_8$ 5.6 mil B/Al-6061F obtained with the compliance gage (crack length = 12.94 mm).

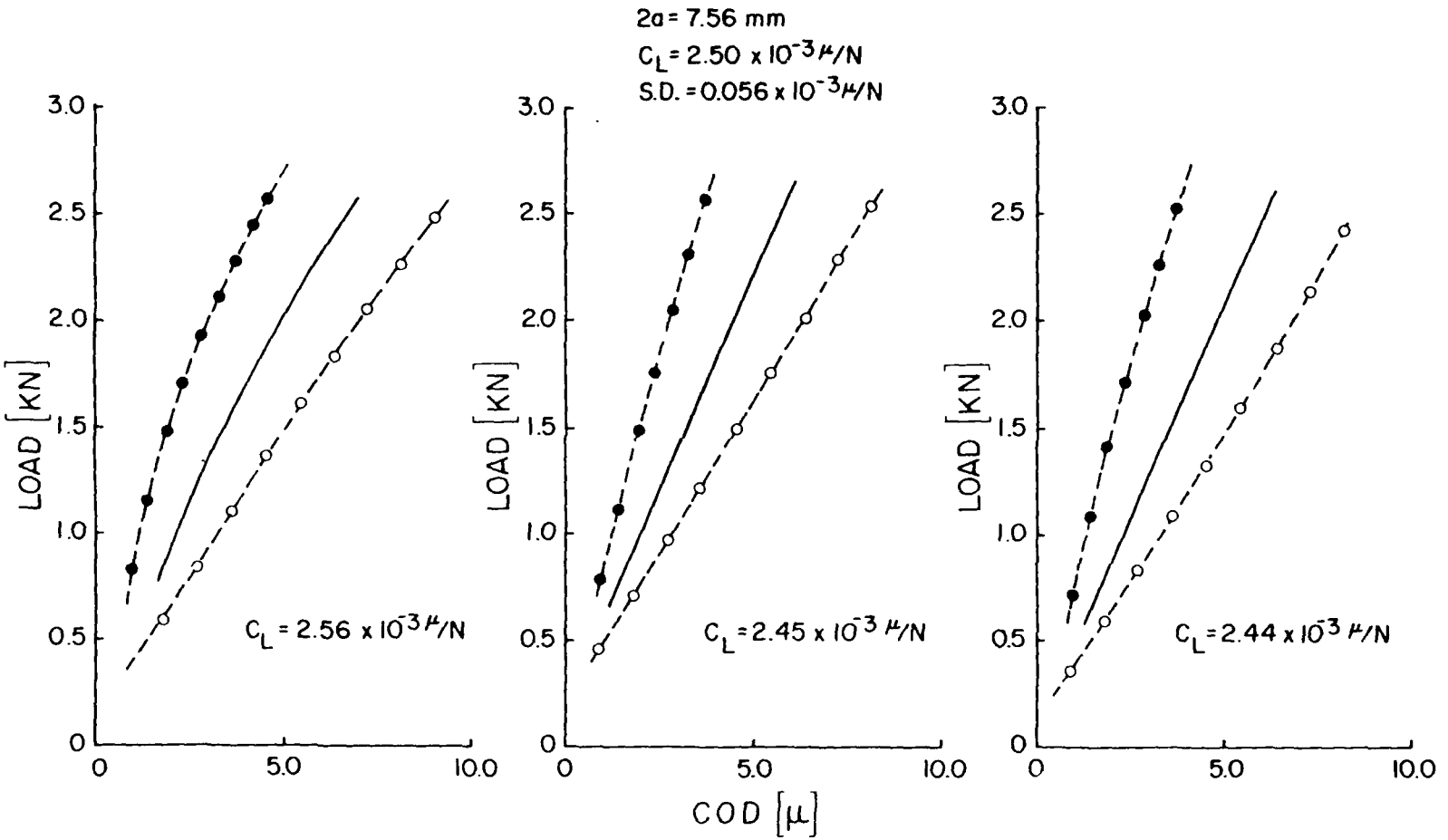


Figure 15. Example of three load-COD curves at initial loading for unidirectional 5.6 mil B/Al-6061F specimens obtained with the IDG (crack length = 7.56 mm).

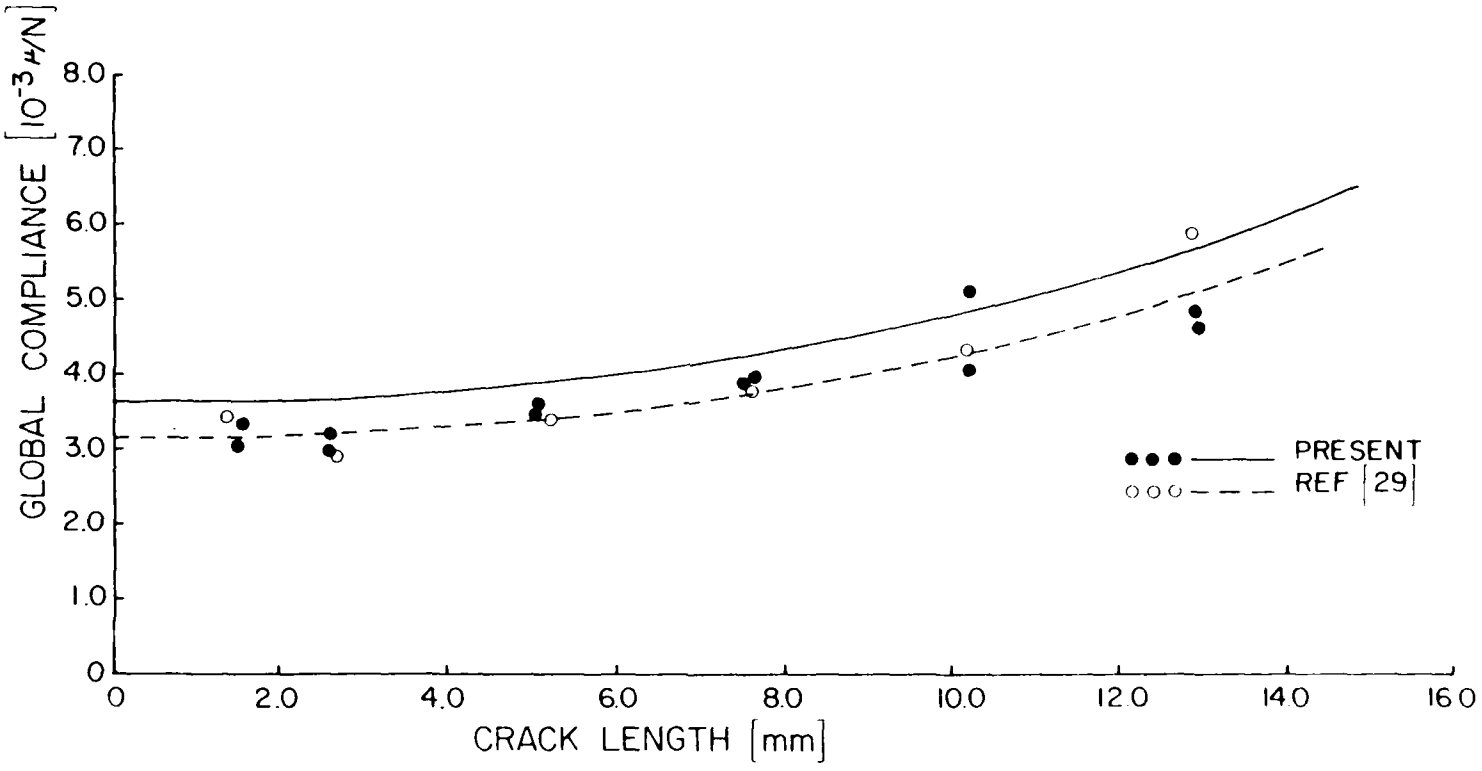


Figure 16. Global compliance versus crack length for unidirectional 5.6 mil B/Al-6061F.

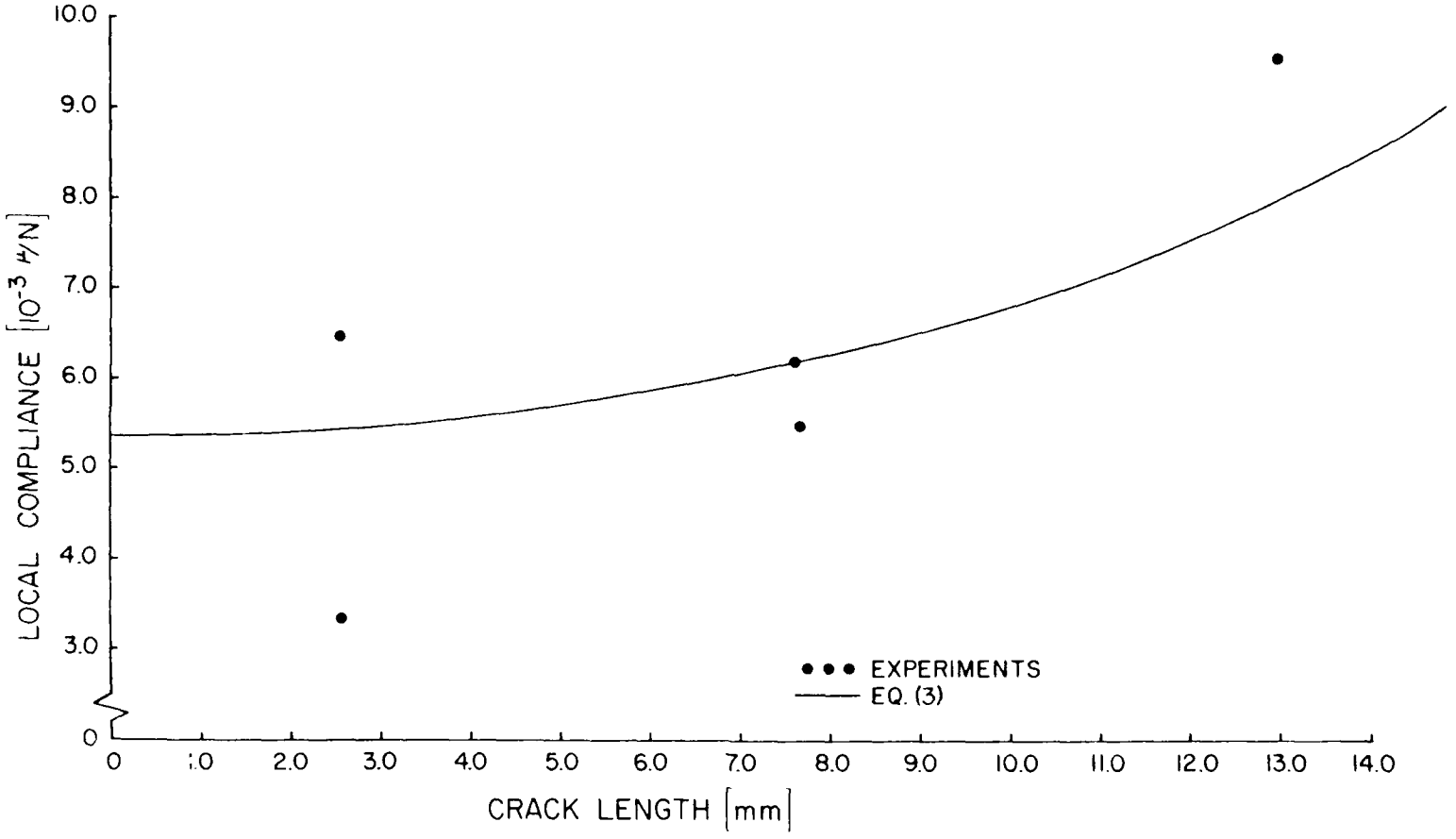


Figure 17. Global compliance versus crack length for $[90]_8$ 5.6 mil B/Al-6061F.

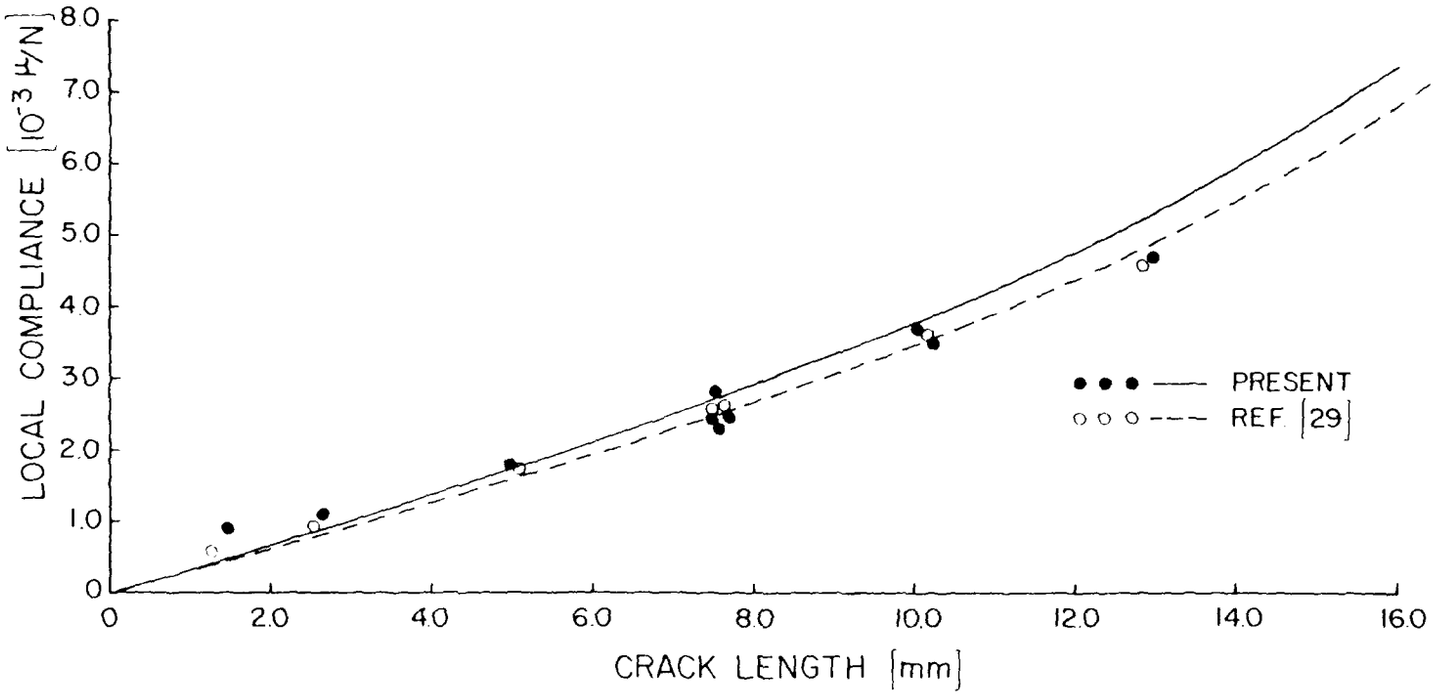


Figure 18. Local compliance versus crack length for unidirectional 5.6 mil B/Al-6061F.

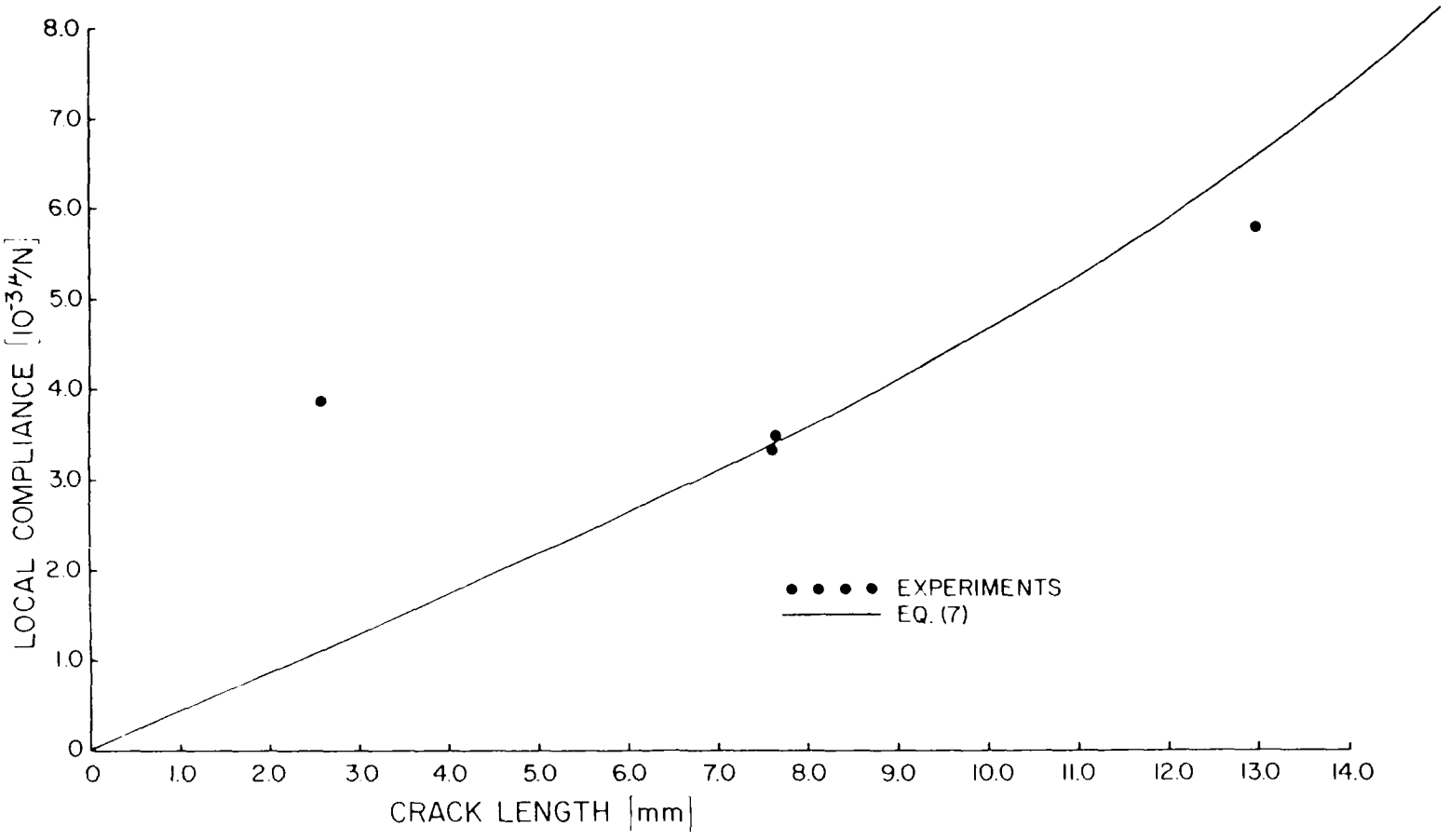


Figure 19. Local compliance versus crack length for $[90]_8$ 5.6 mil B/Al-6061F.

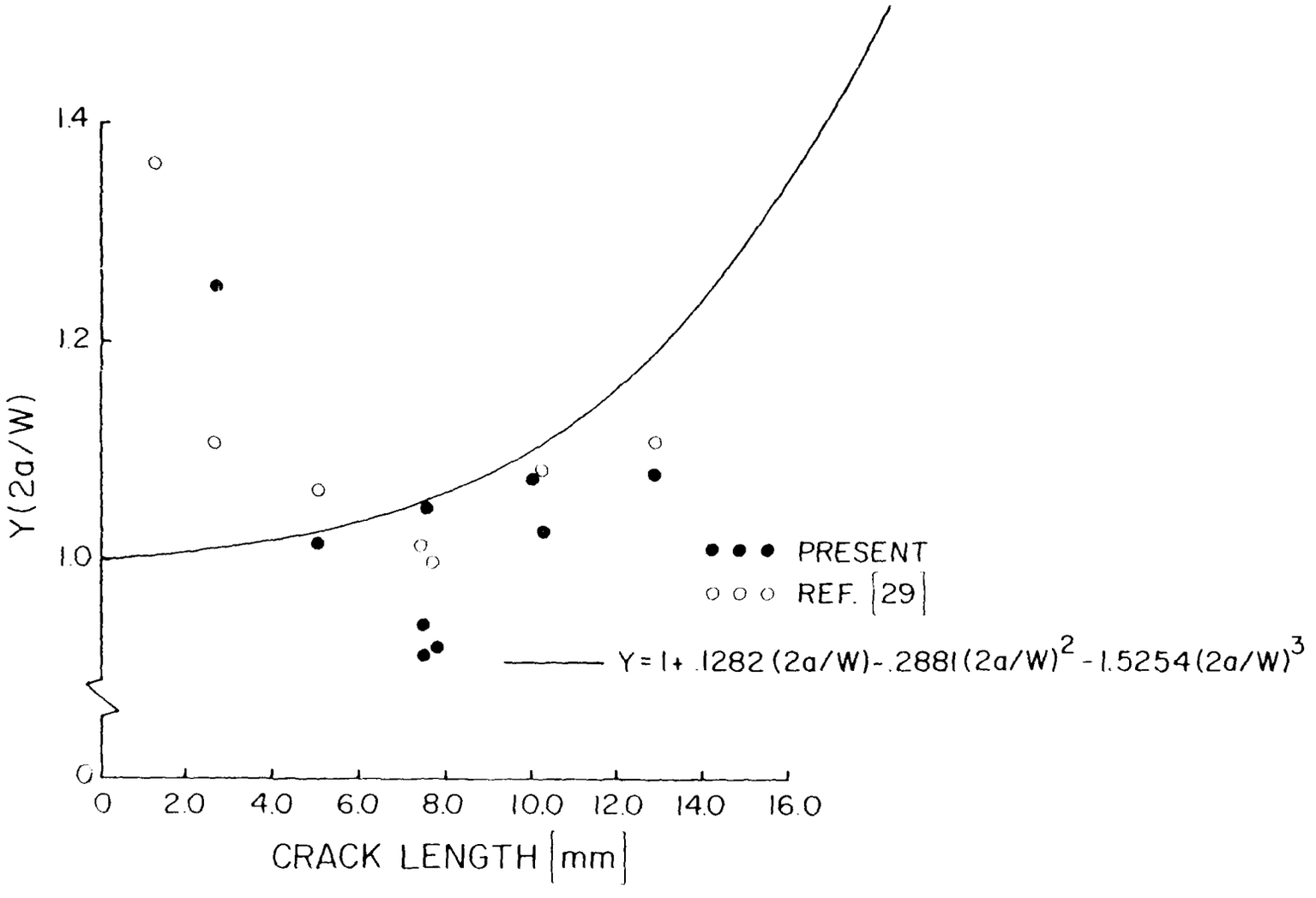


Figure 20. Comparison of experimental K-calibration factors with theoretical isotropic curve for unidirectional 5.6 mil B/Al-6061F.

AD-A111 006 DREXEL UNIV PHILADELPHIA PA DEPT OF MECHANICAL ENGIN--ETC F/G 11/4
FRACTURE BEHAVIOR OF BORON ALUMINUM COMPOSITES AT ROOM AND ELEV--ETC(U)
SEP 80 J AWERBUCH AFOSR-79-0079

UNCLASSIFIED AFOSR-TR-82-0038 NL

2 OF 2
AD A
111006

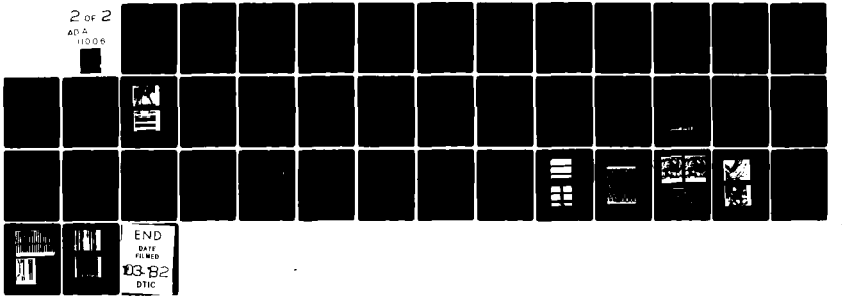

END
DATE FILMED
03-82
DTIC

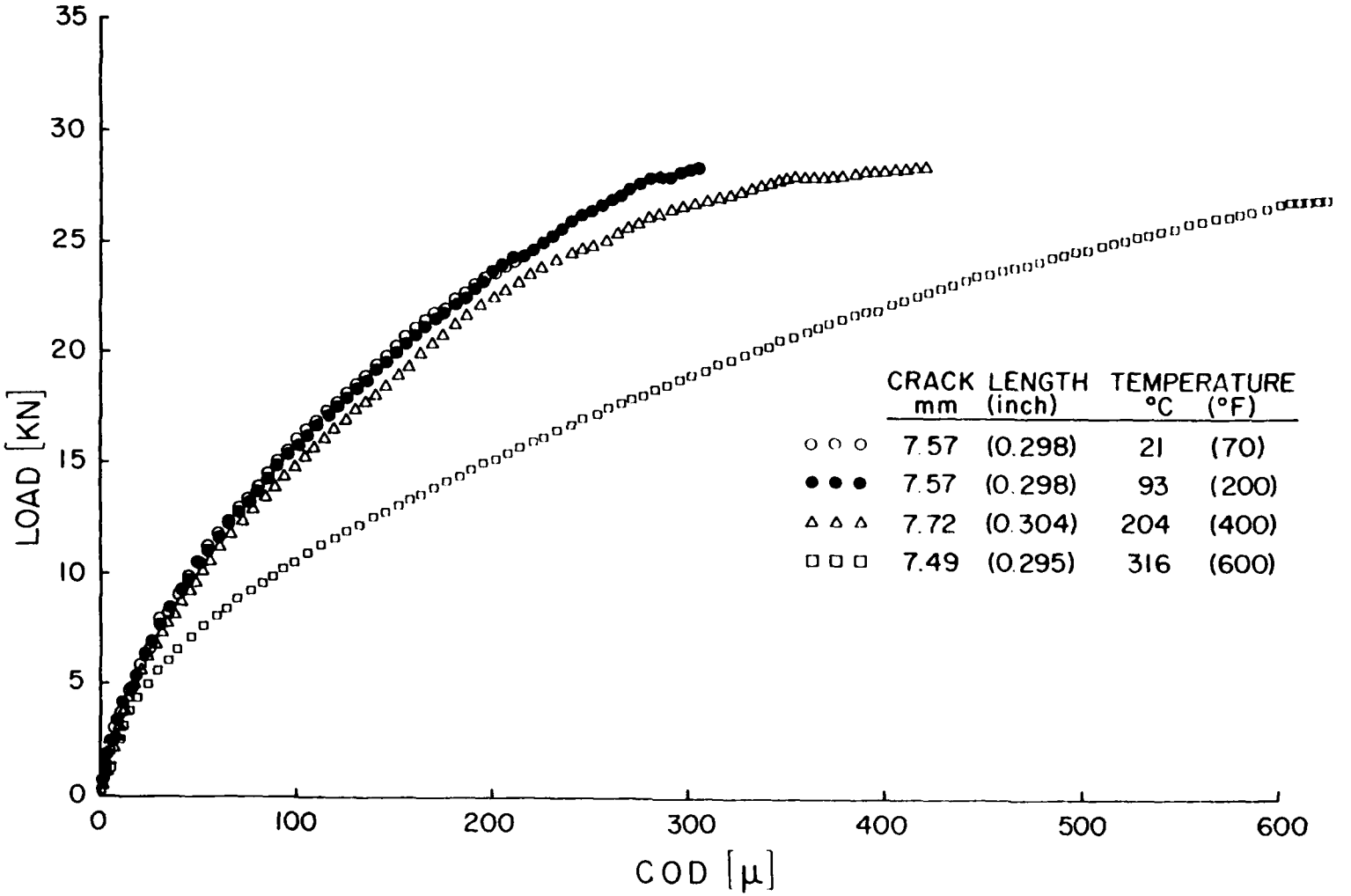


Figure 21. Load-COD curves for unidirectional 5.6 mil B/Al-6061F at various temperatures, obtained with the IDG (crack length ≅ 7.60 mm).

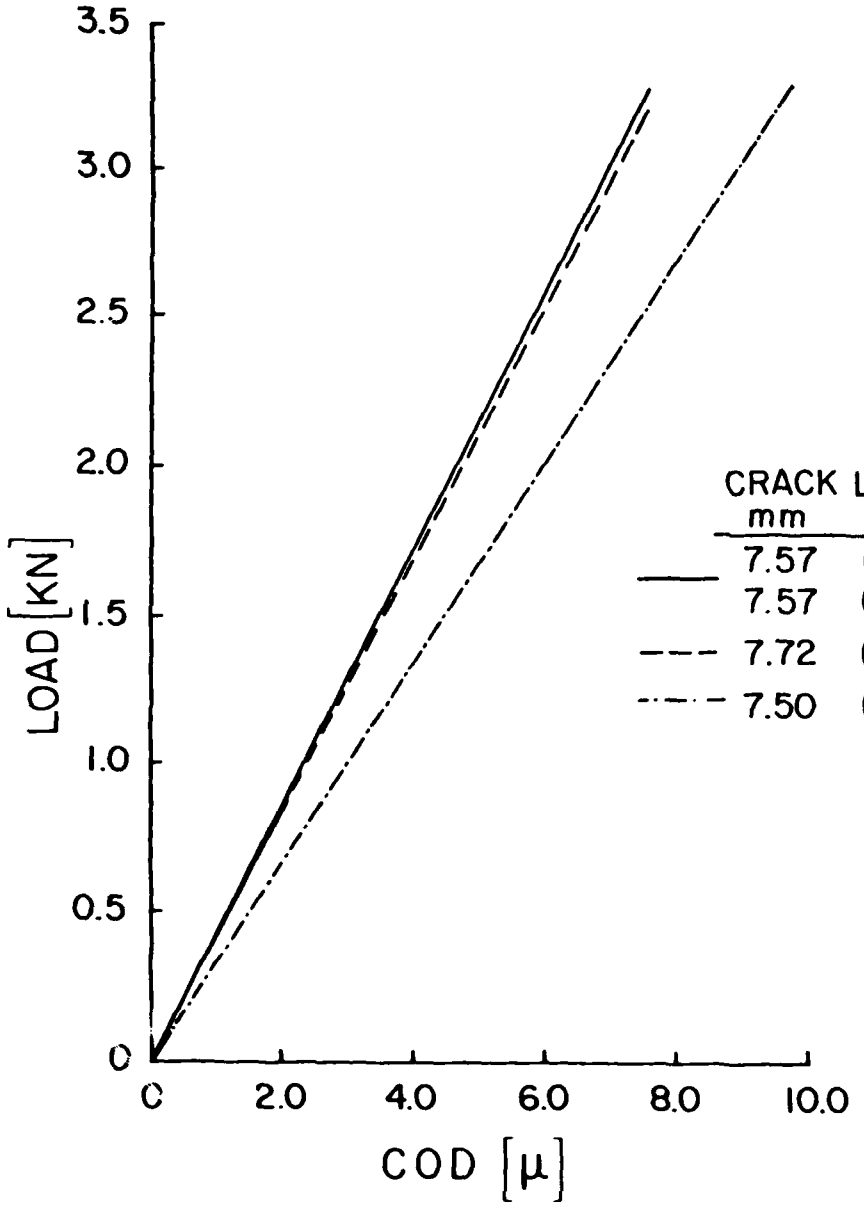


| CRACK LENGTH mm | (inch) | TEMPERATURE °C | (°F) | COMPLIANCE (μ/N)x10$^{-3}$ |
|---|---|---|---|---|
| 7.57 | (0.298) | 21 | (70) | 2.34 |
| 7.57 | (0.298) | 93 | (200) | 2.31 |
| 7.72 | (0.304) | 204 | (400) | 2.36 |
| 7.50 | (0.295) | 316 | (600) | 2.97 |

Figure 22. Initial load-COD curves for unidirectional 5.6 mil B/Al-6061F at various temperatures, obtained with the IDG (crack length ≈ 7.60 mm).

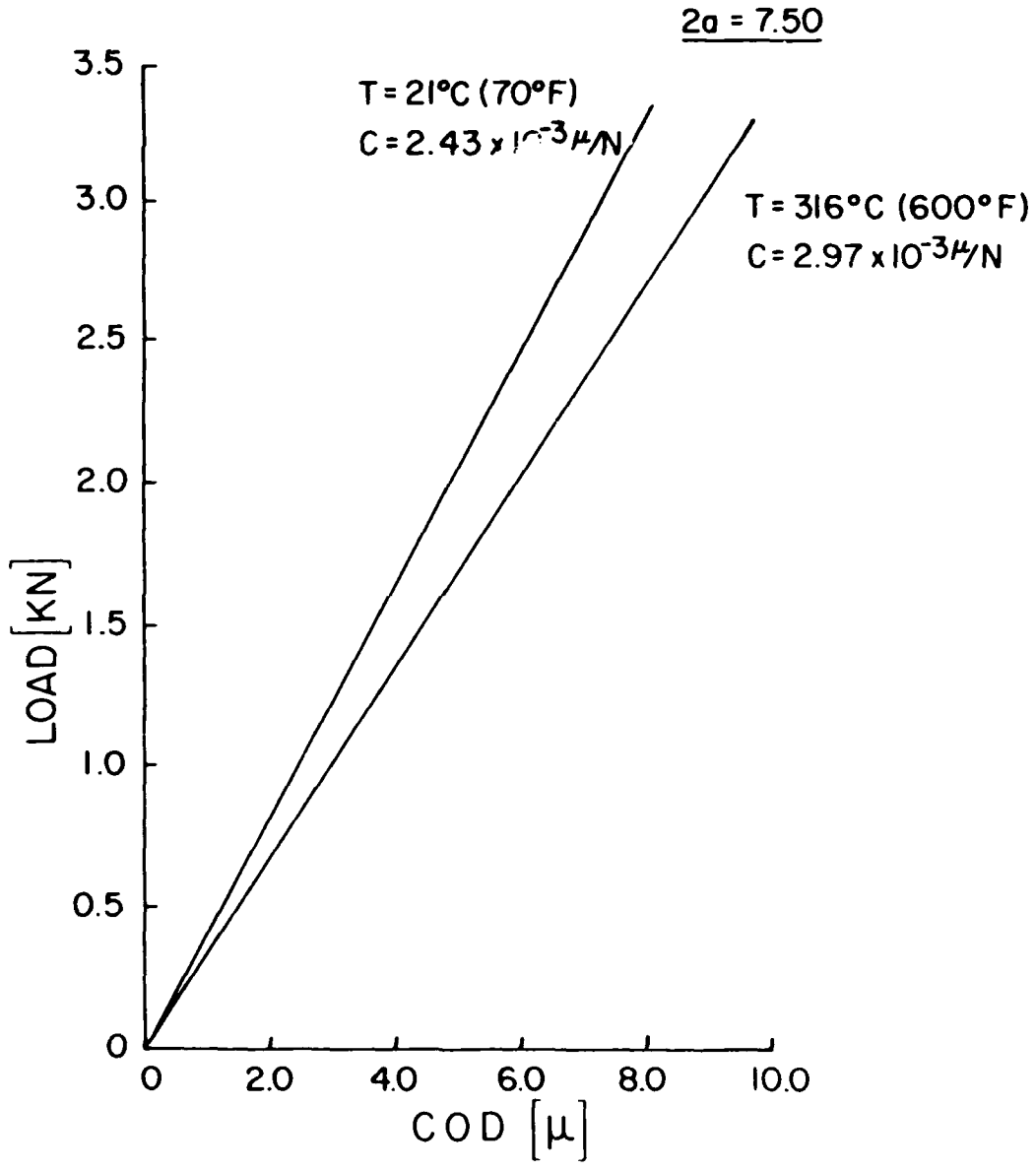


Figure 23. Comparison of initial load-COD curves for unidirectional 5.6 mil B/Al-6061F at 21°C and 316°C, obtained with the IDG (crack length = 7.50 mm).

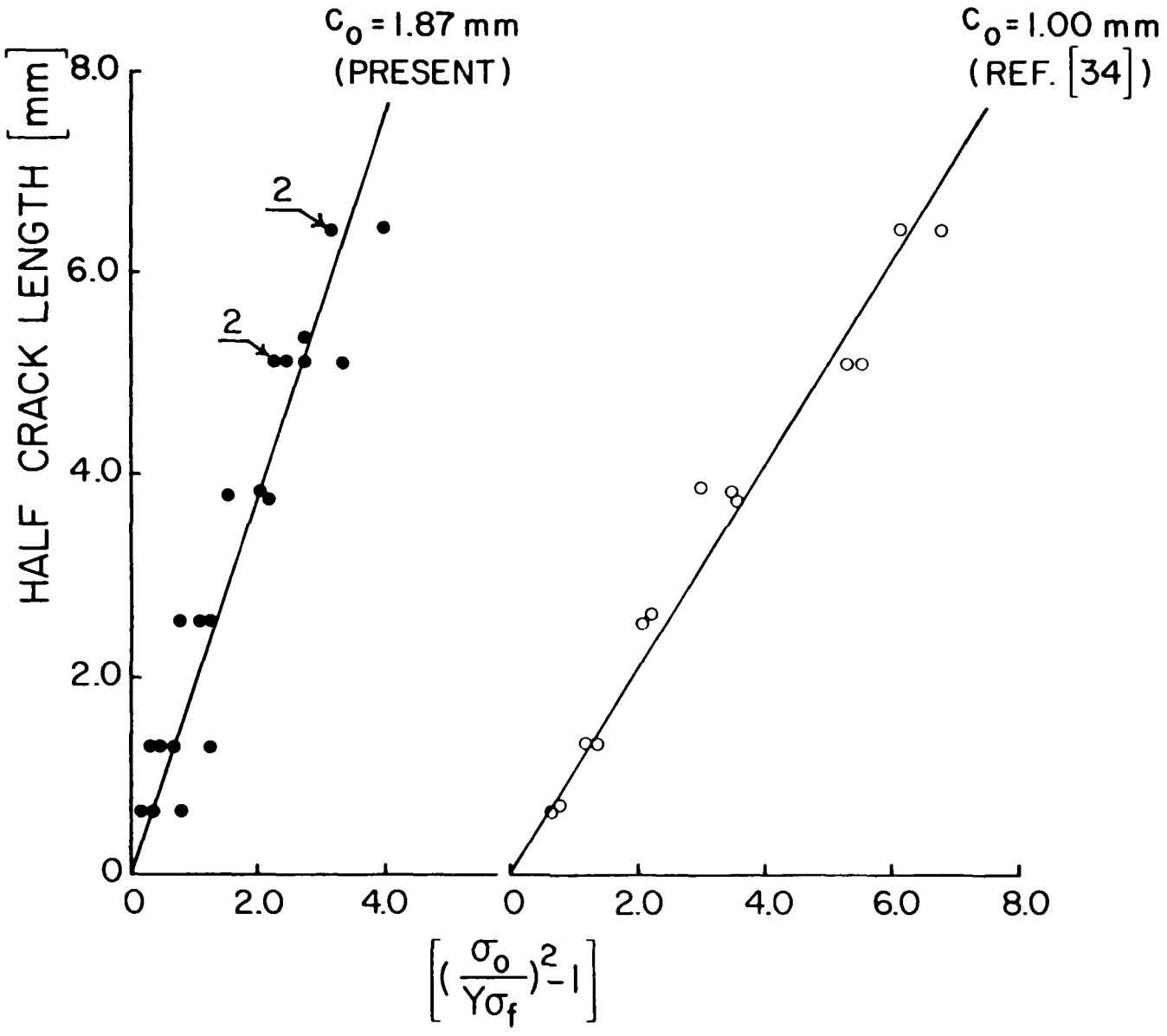


Figure 24. Least squares fit for $c_o$ for unidirectional 5.6 mil B/Al-6061F.

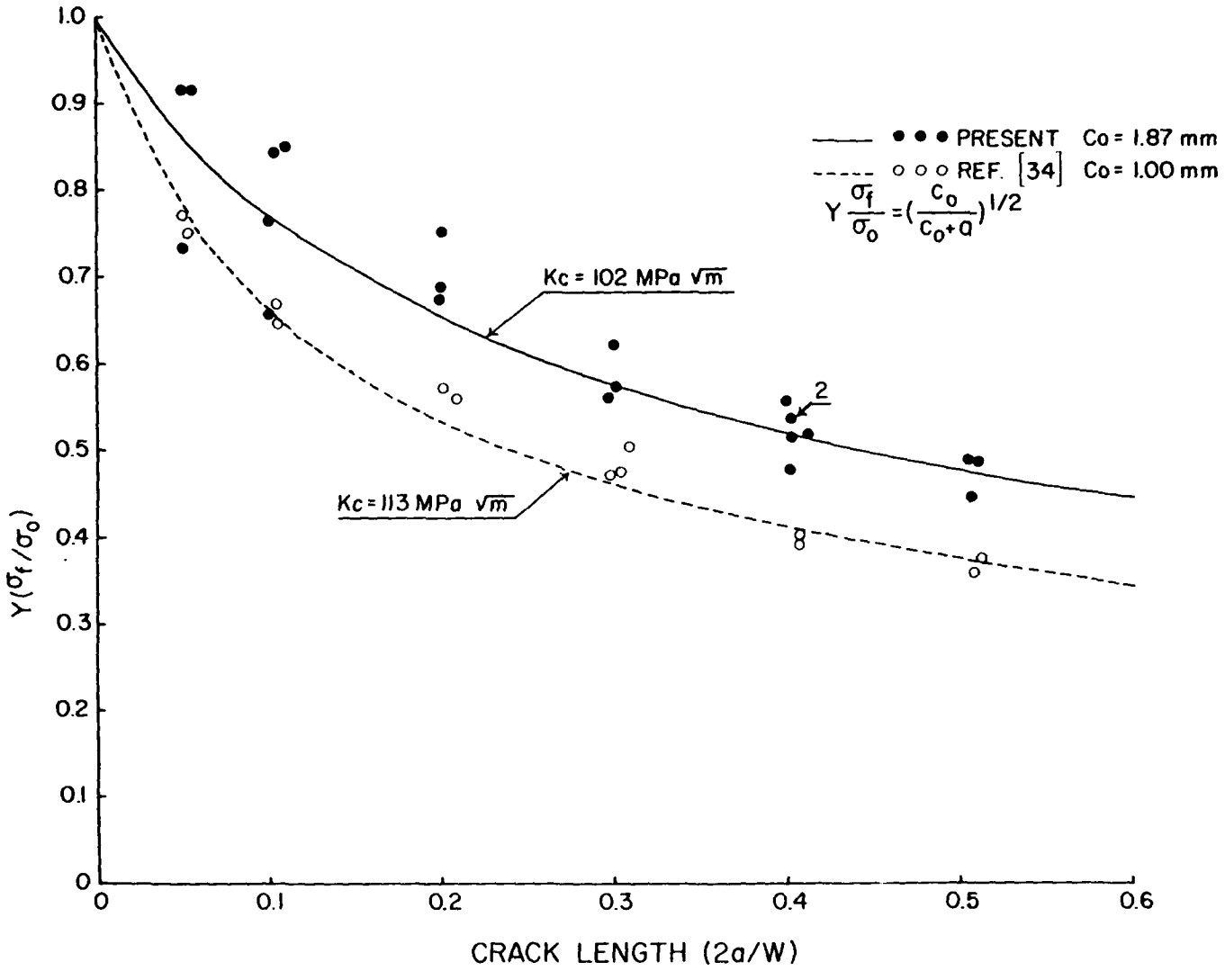


Figure 25. Comparison of analytical (WEK model) and experimental results on notched strength for unidirectional 5.6 mil B/Al-6061F.

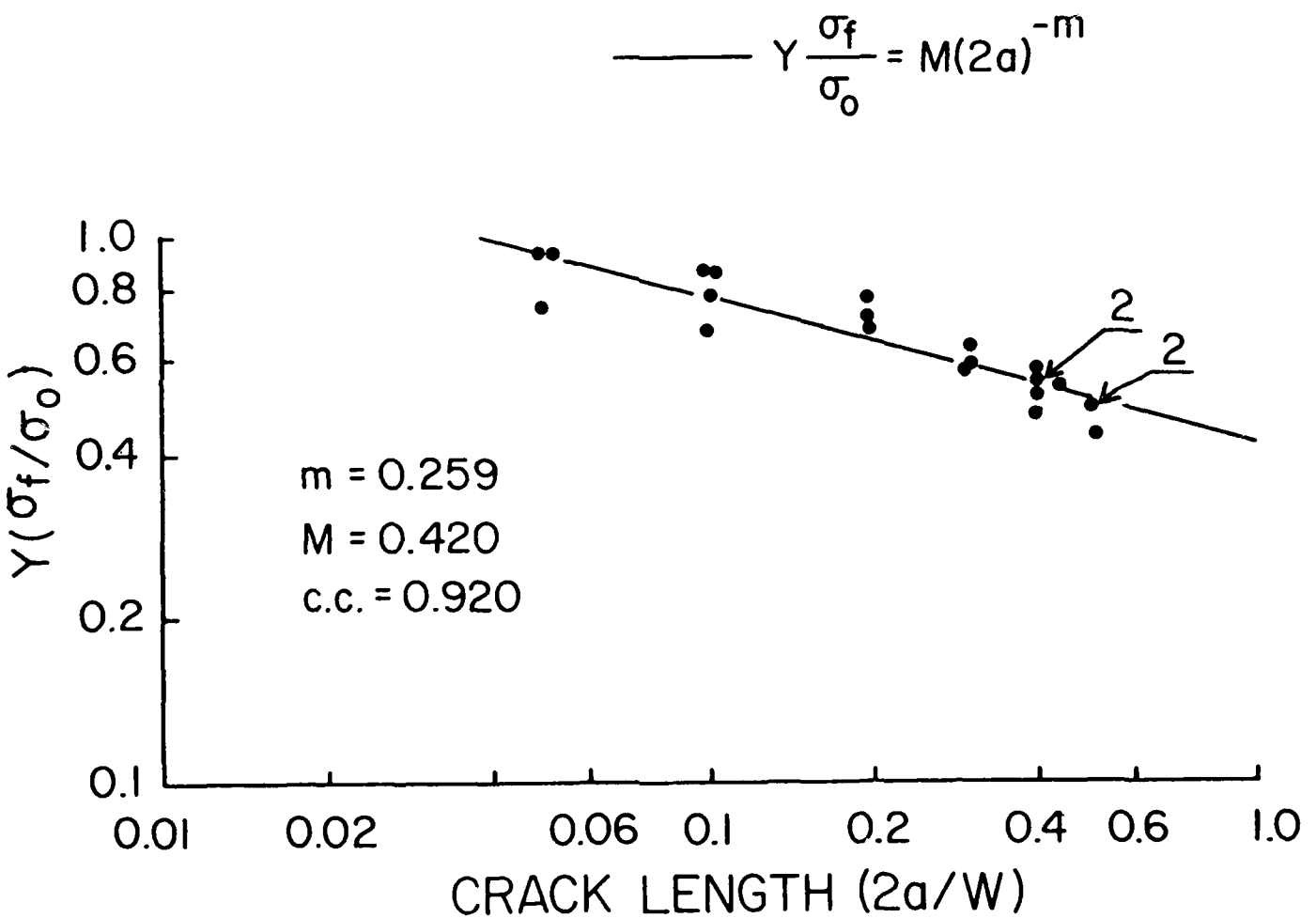


Figure 26. Notched strength versus crack length: comparison of ML model with experimental results for unidirectional 5.6 mil B/Al-6061F.

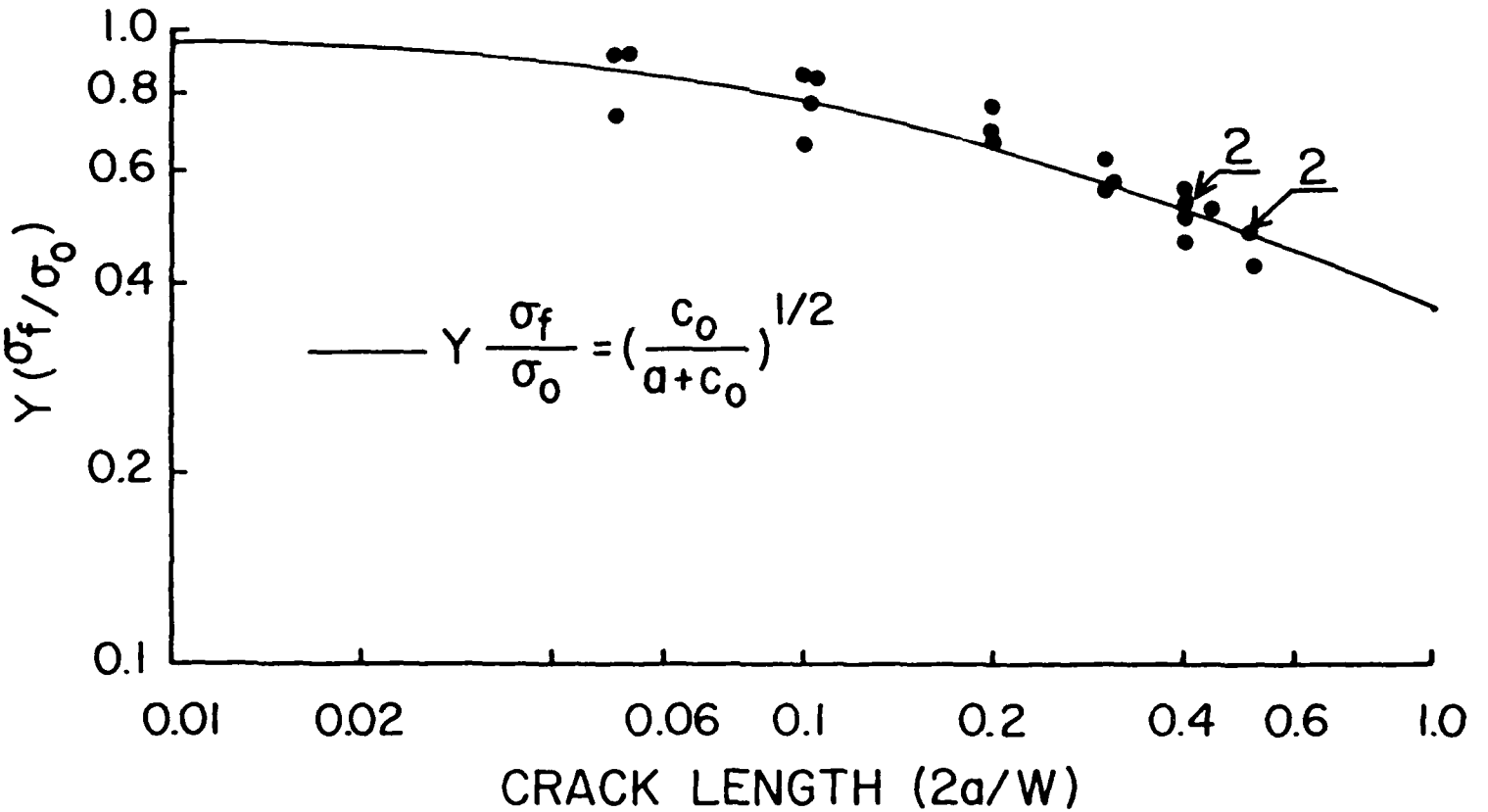


Figure 27. Notched strength versus crack length: comparison of WEK model with experimental results on logarithmic scale for unidirectional 5.6 mil B/Al-6061F.

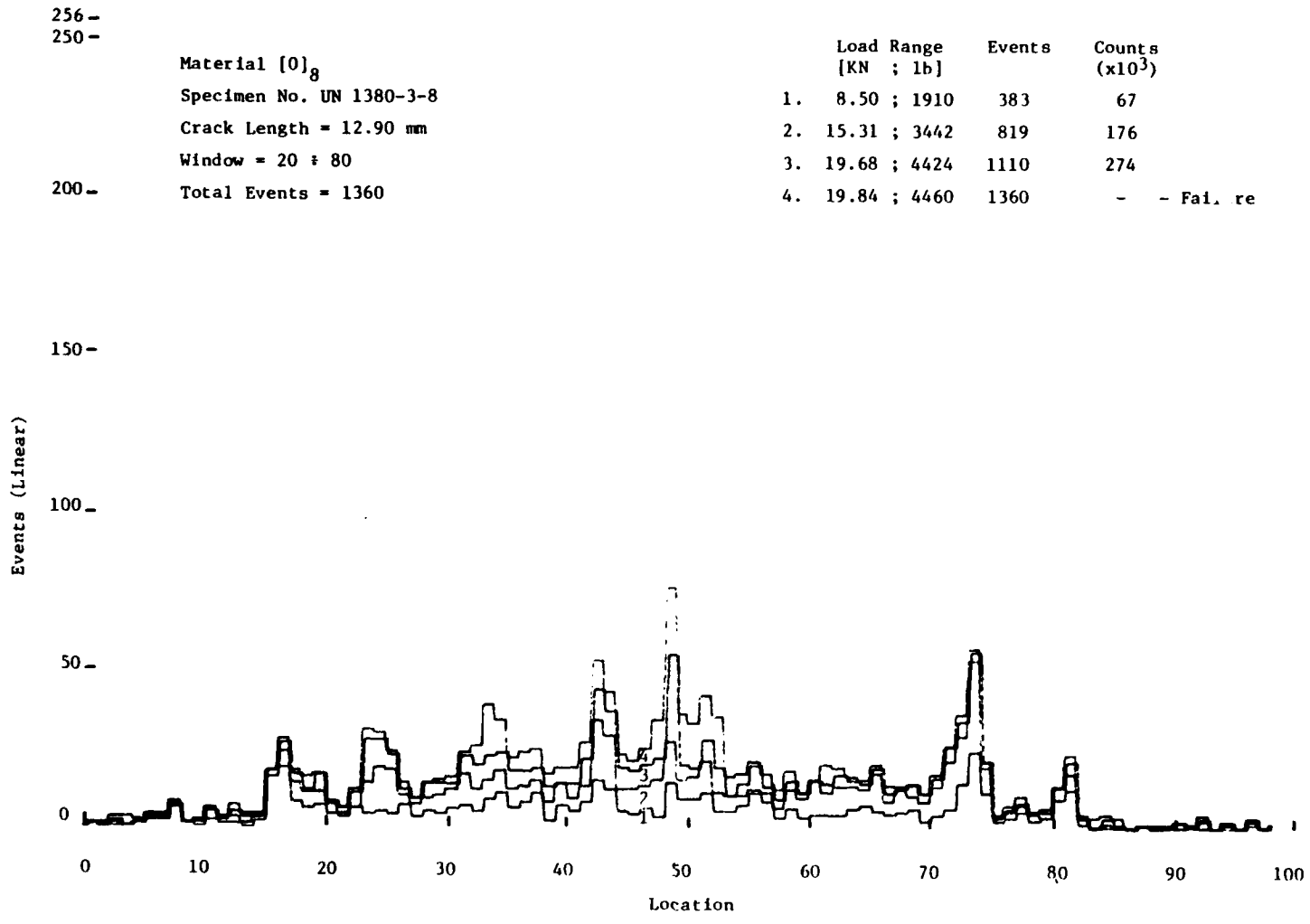


Figure 28. Location distribution histograms for notched unidirectional 5.6 mil B/Al-6061F specimen at various load levels (crack length = 12.90 mm).

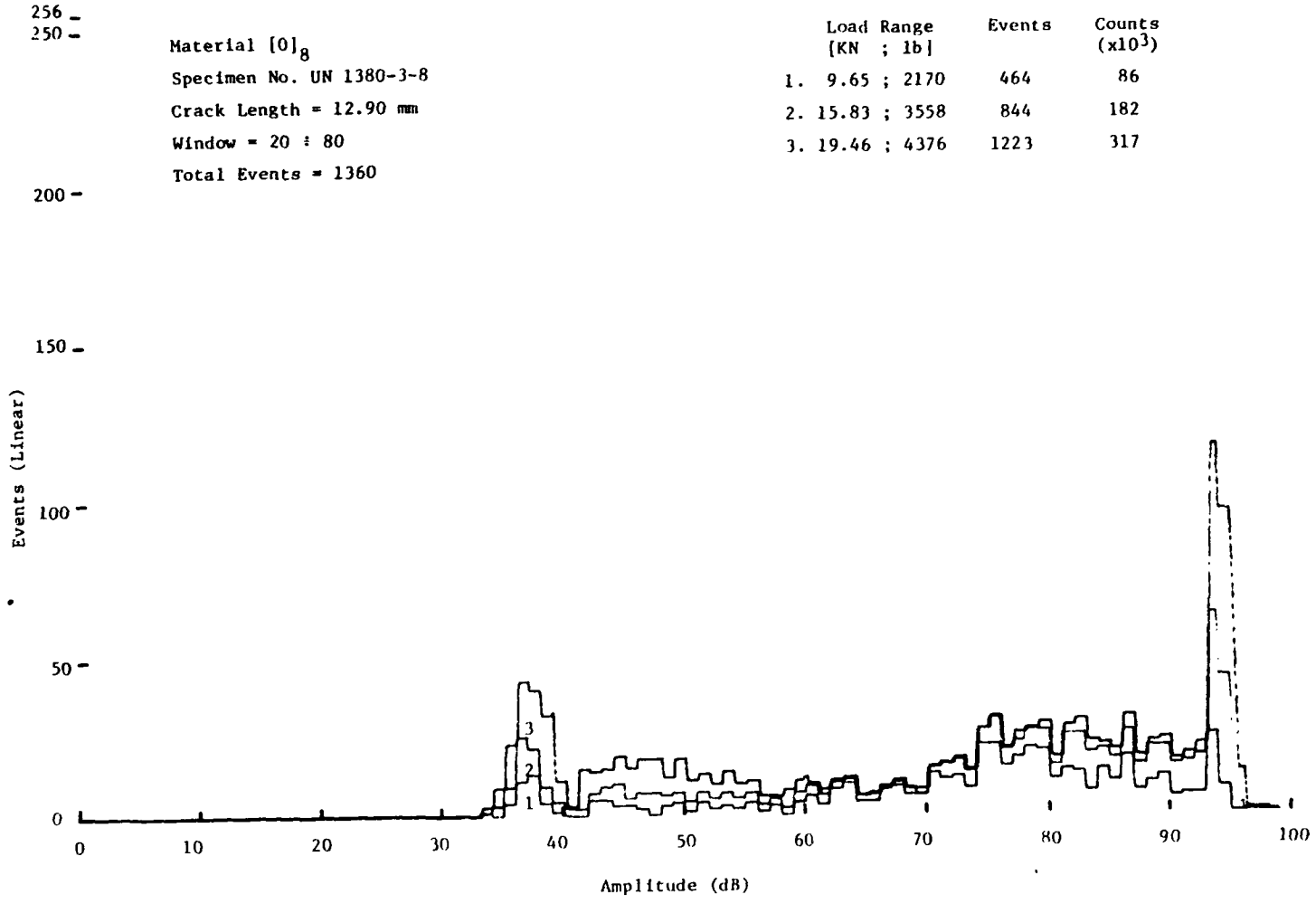


Figure 29. Amplitude distribution histograms for unnotched unidirectional 5.6 mil B/A1-6061F specimen at various load levels (crack length = 12.90 mm).

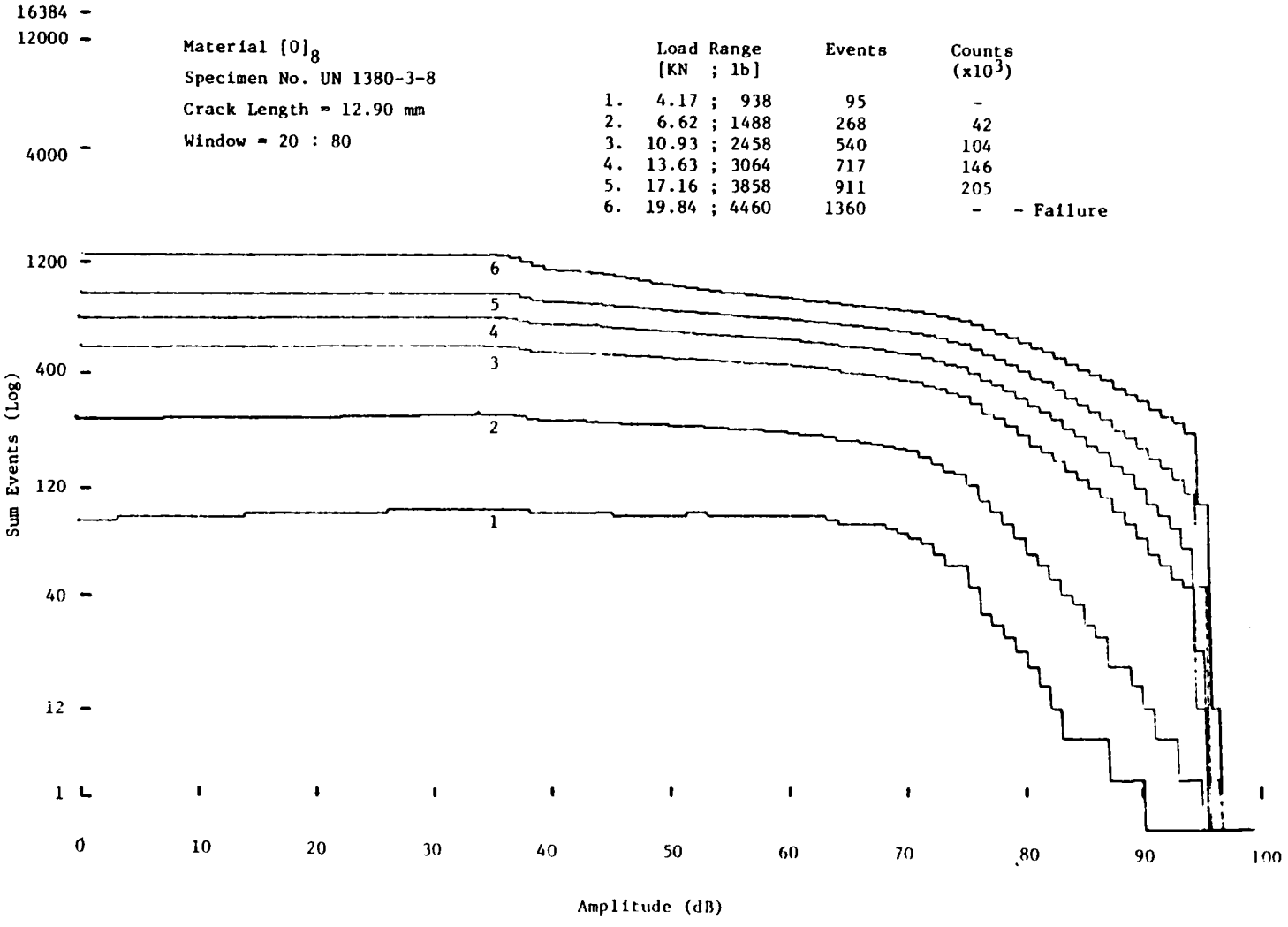


Figure 30. Cumulative Event Amplitude Distributions for notched unidirectional 5.6 mil B/Al-6061 specimen at various load levels (crack length = 12.90 mm).

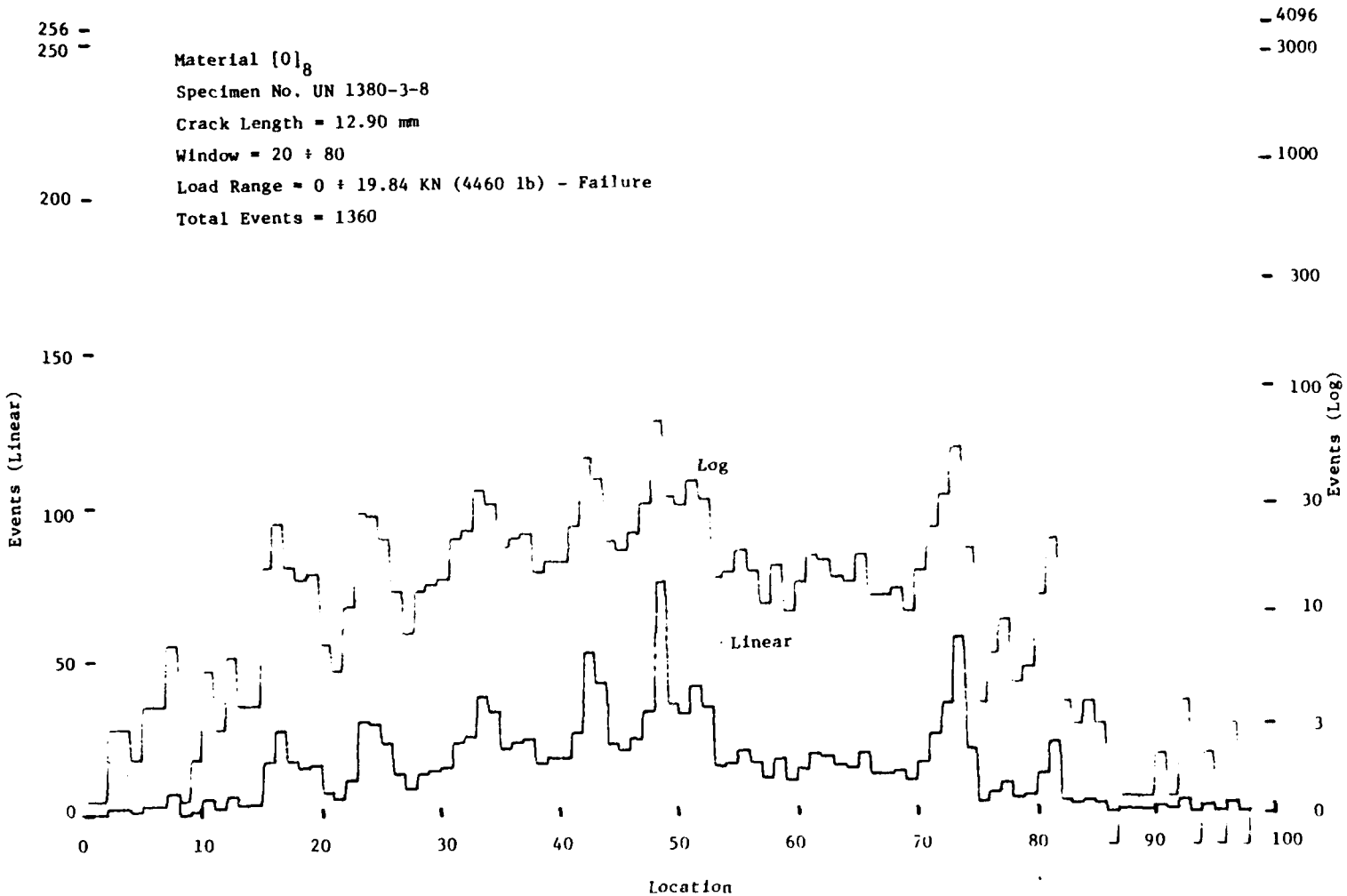


Figure 31. Location distribution histograms (in linear and logarithmic scales) for notched unidirectional 5.6 mil B/Al-6061F specimen after failure (crack length = 12.90 mm).

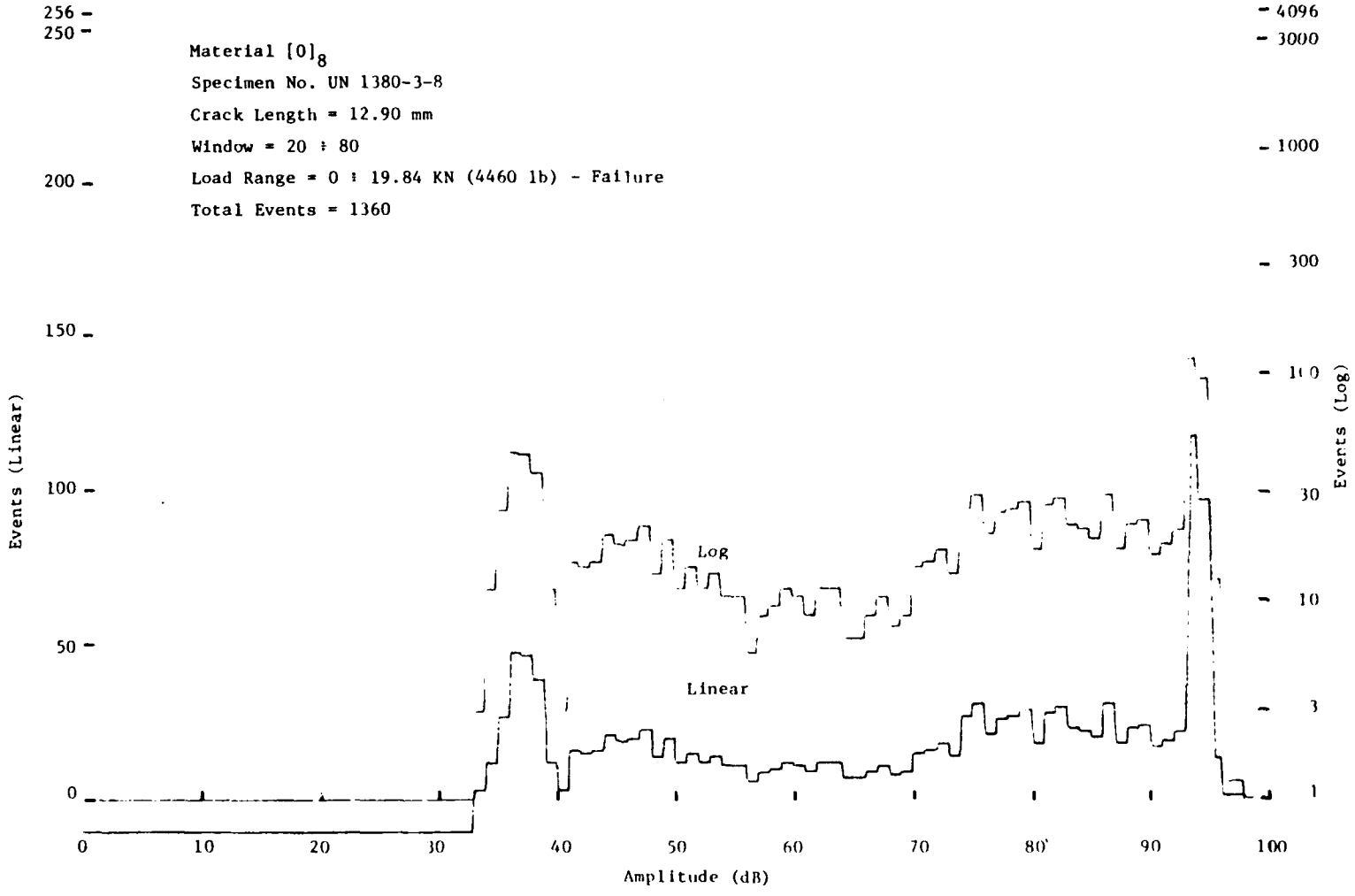


Figure 32. Amplitude distribution histograms (in linear and logarithmic scales) for notched unidirectional 5.6 mil B/Al-6061F specimen after failure (crack length = 12.90 mm).

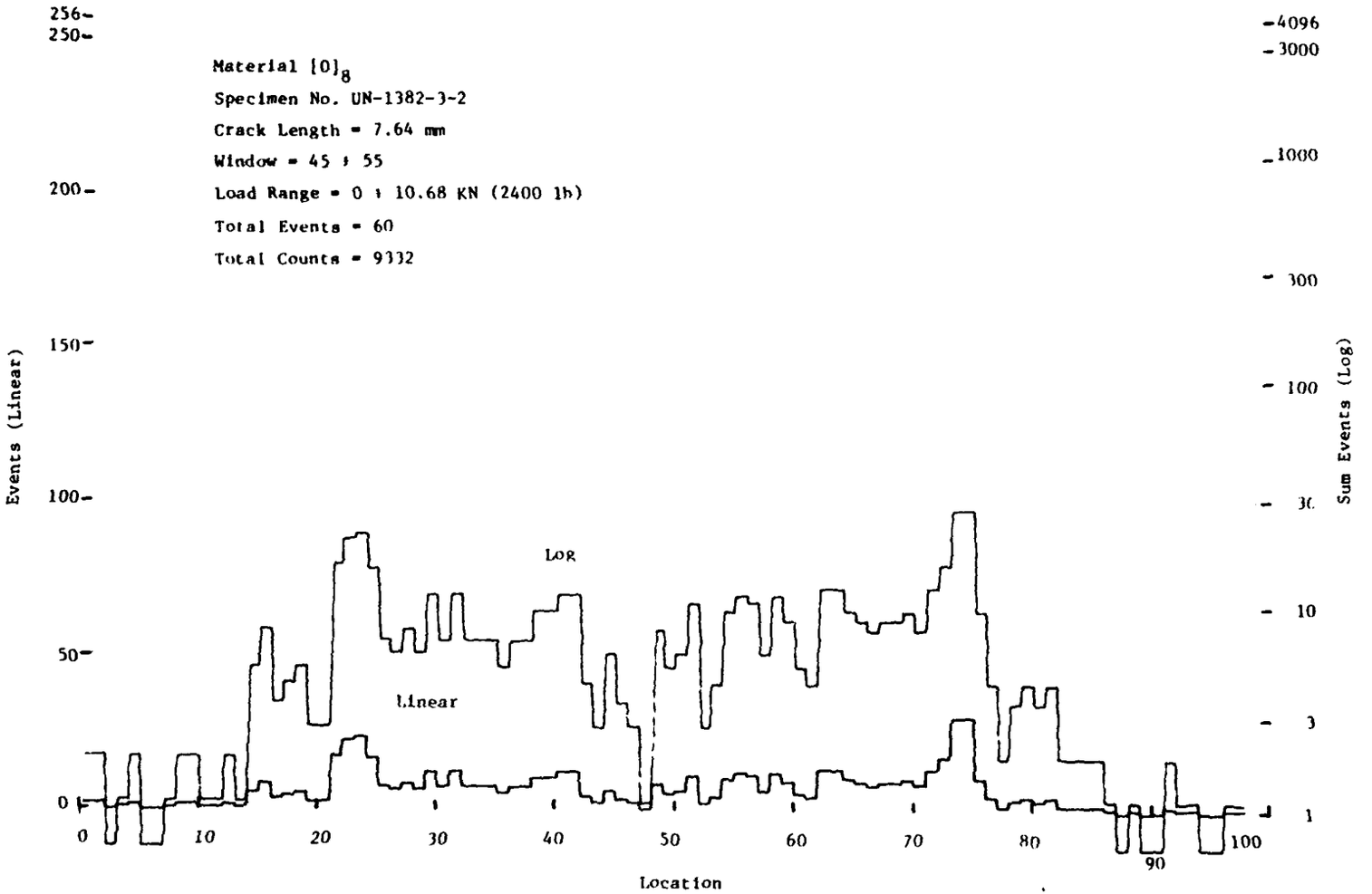


Figure 33. Location distribution histograms (in linear and logarithmic scales) for notched unidirectional 5.6 mil B/Al-6061F specimen loaded to 40% of expected ultimate load (crack length = 7.64 mm).

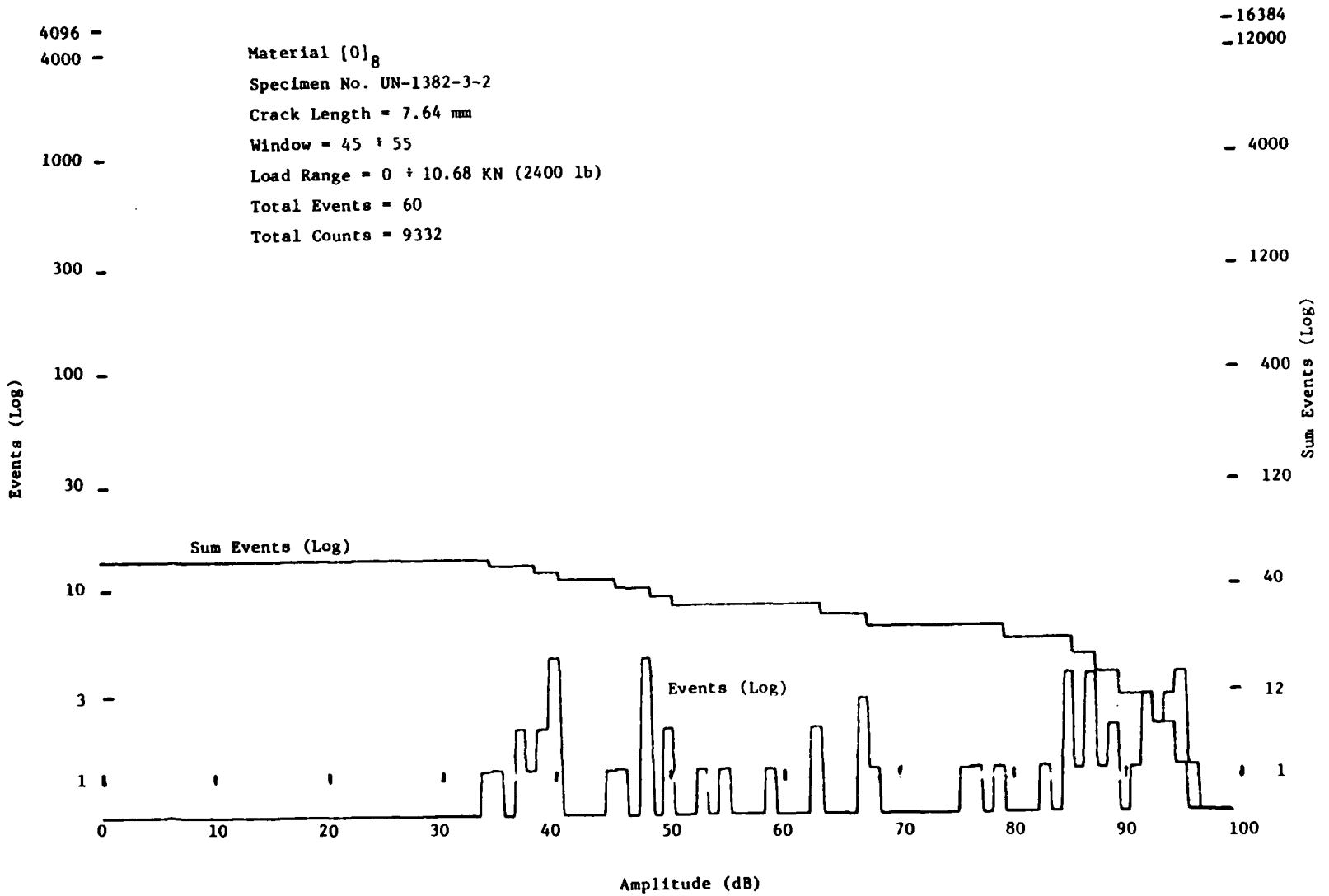


Figure 34. Amplitude distribution histogram and Cumulative Event Amplitude Distribution for notched unidirectional 5.6 mil B/Al-6061F specimen loaded to 40% of expected ultimate load (crack length = 7.64 mm).

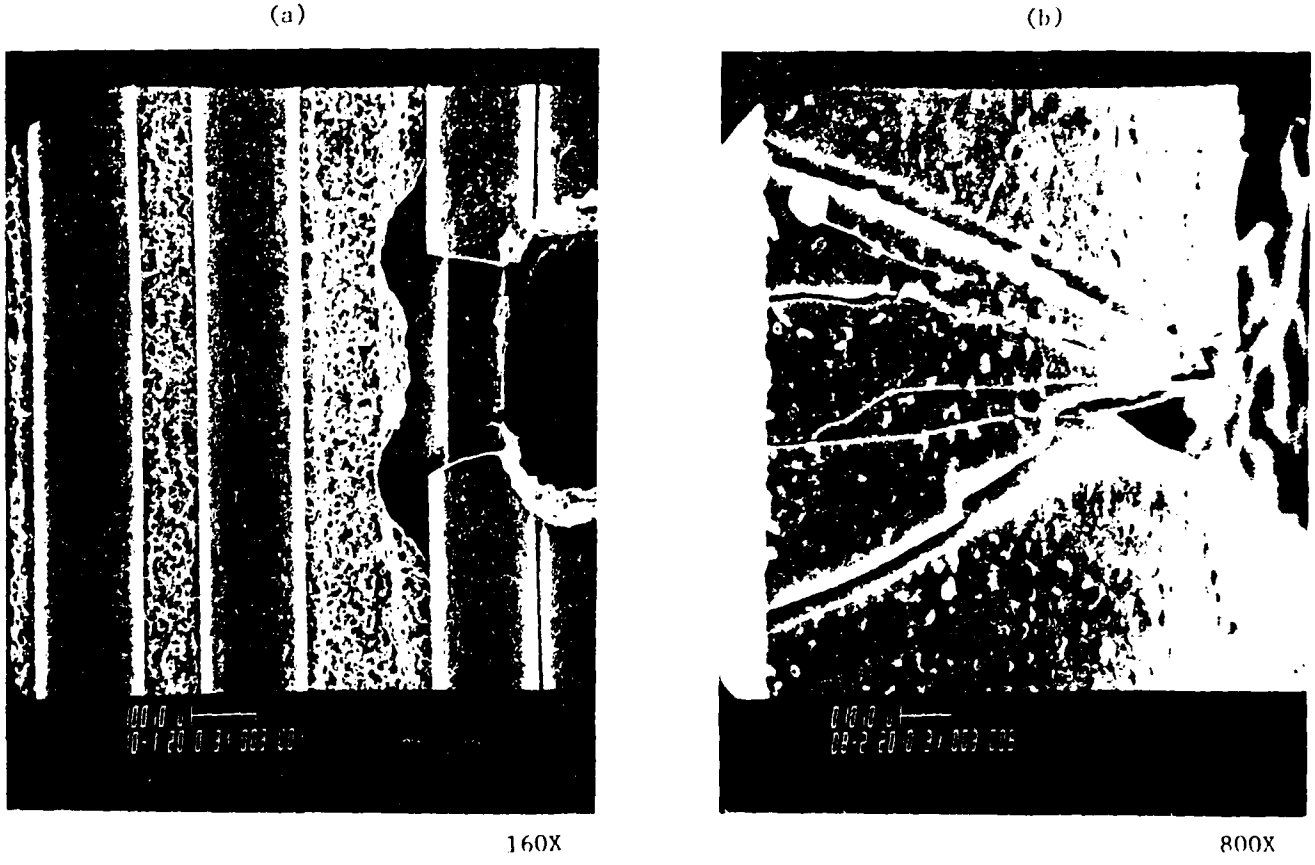


Figure 35. Scanning electron microscope photographs of broken fibers at crack tip (after dissolving aluminum matrix) for unidirectional 5.6 mil B/Al-6061F specimen loaded to 40% of expected ultimate load (crack length ~ 7.64 mm): a. crack tip damage, broken fiber seen in third layer; b. detail of broken fiber.

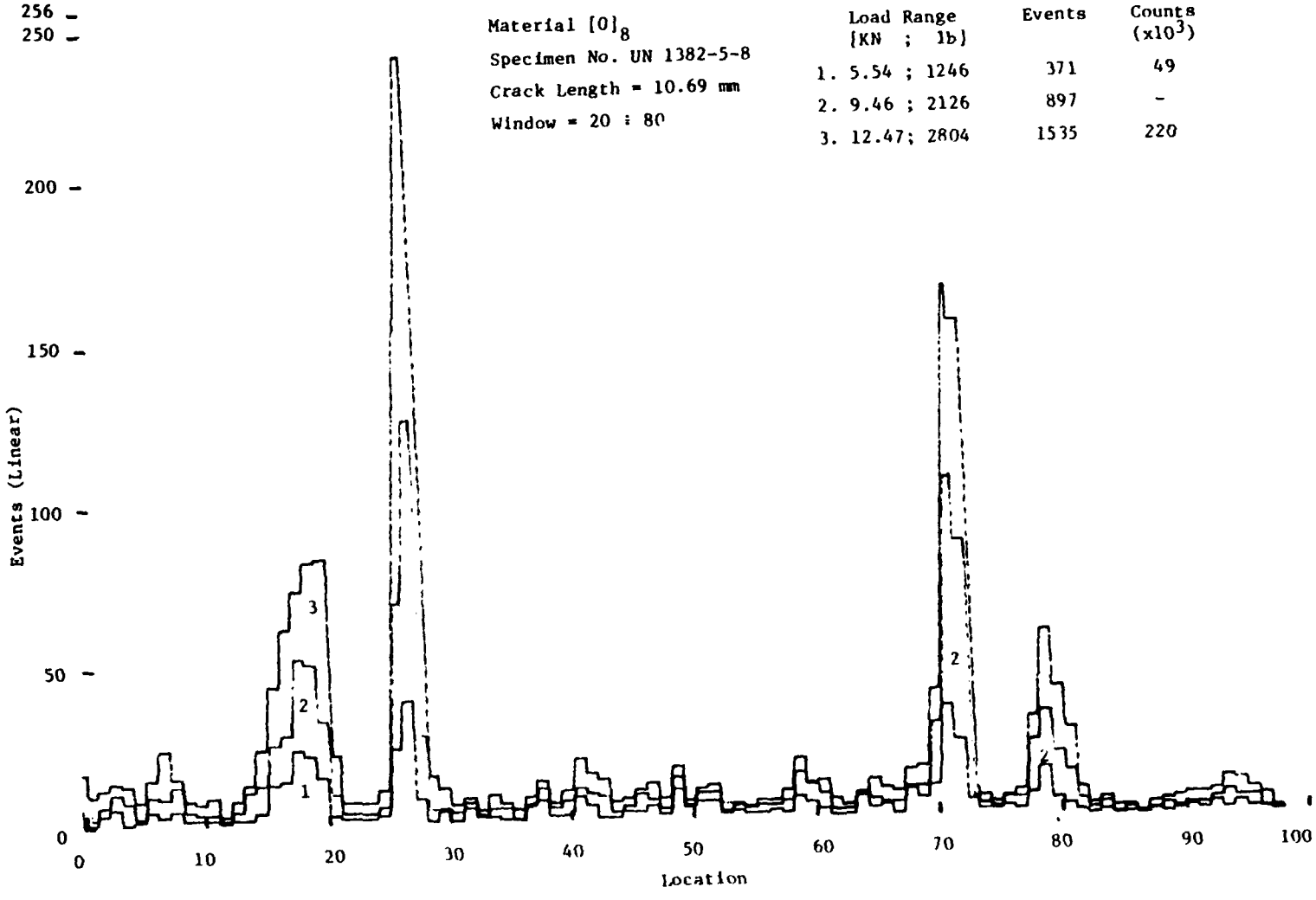


Figure 36. Location distribution histograms for notched unidirectional 5.6 mil B/Al-6061F specimen at various load levels, clamped with sanding paper (crack length = 10.69 mm).

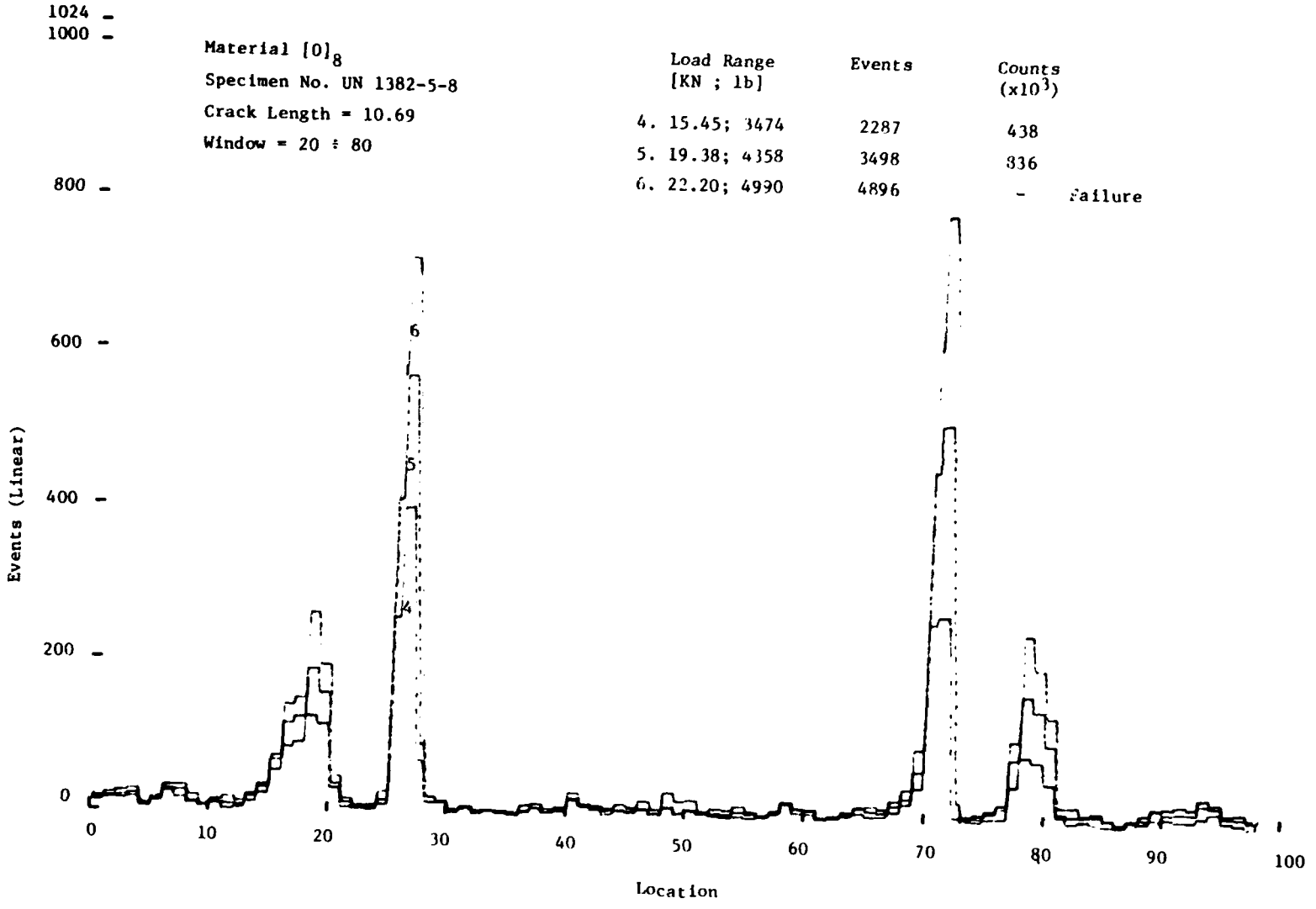


Figure 36. (Continued).

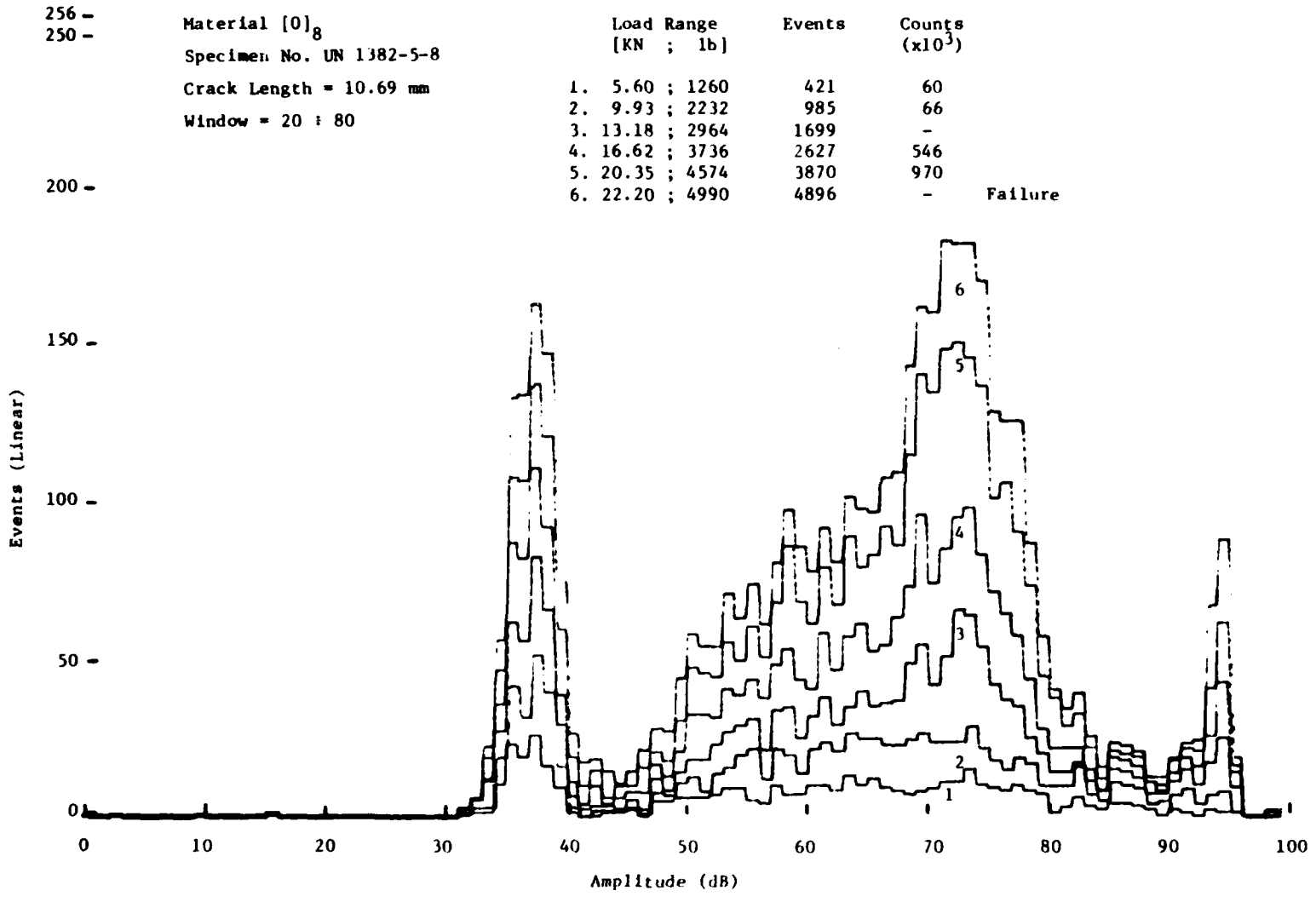


Figure 37. Amplitude distribution histograms for notched unidirectional 5.6 mil B/Al-6061F specimen at various load levels, clamped with sanding paper (crack length = 10.69 mm).

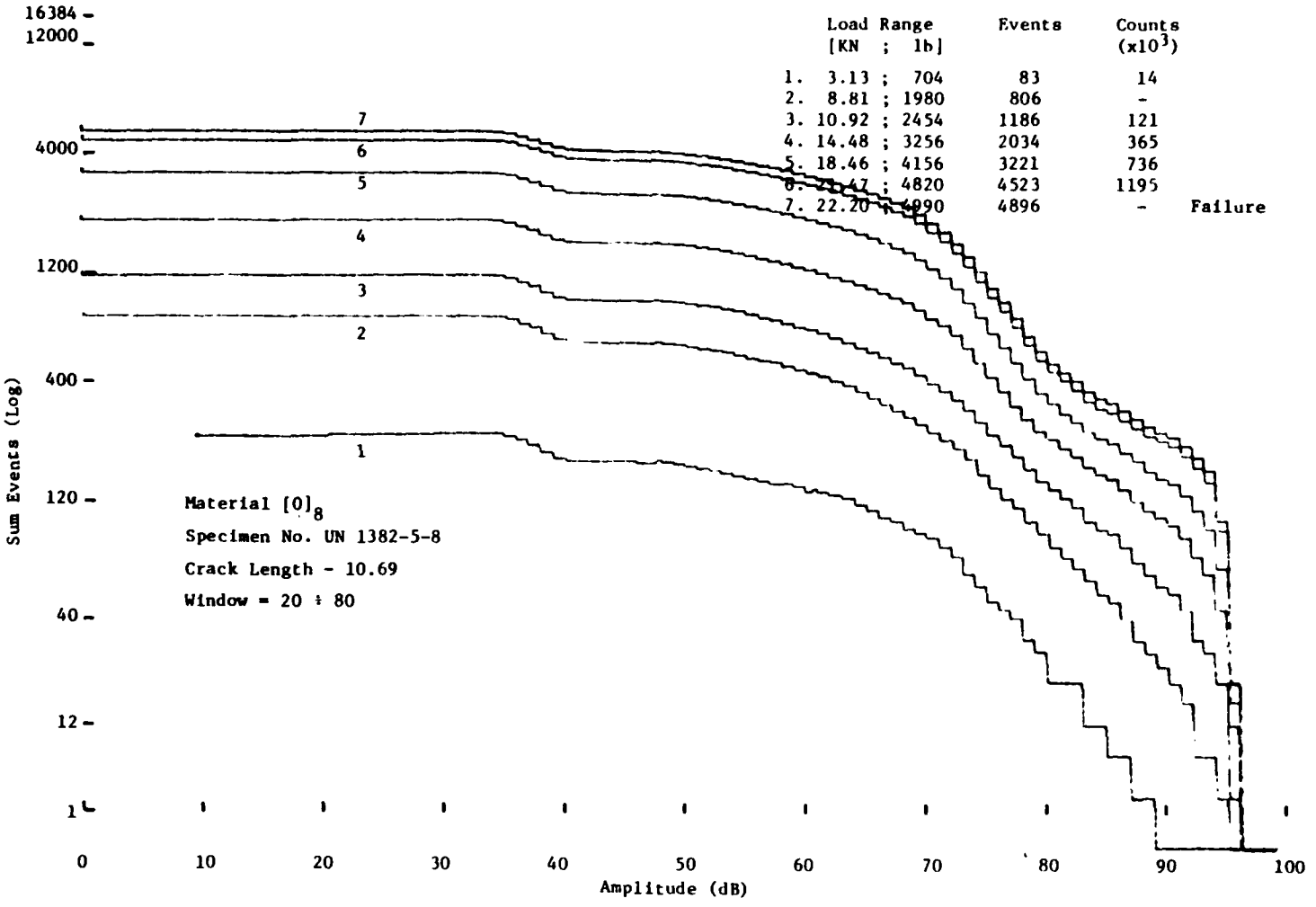


Figure 38. Cumulative Event Amplitude Distributions for notched unidirectional 5.6 mil B/Al-6061F specimen at various load-levels, clamped with sanding paper (crack length = 10.69 mm).

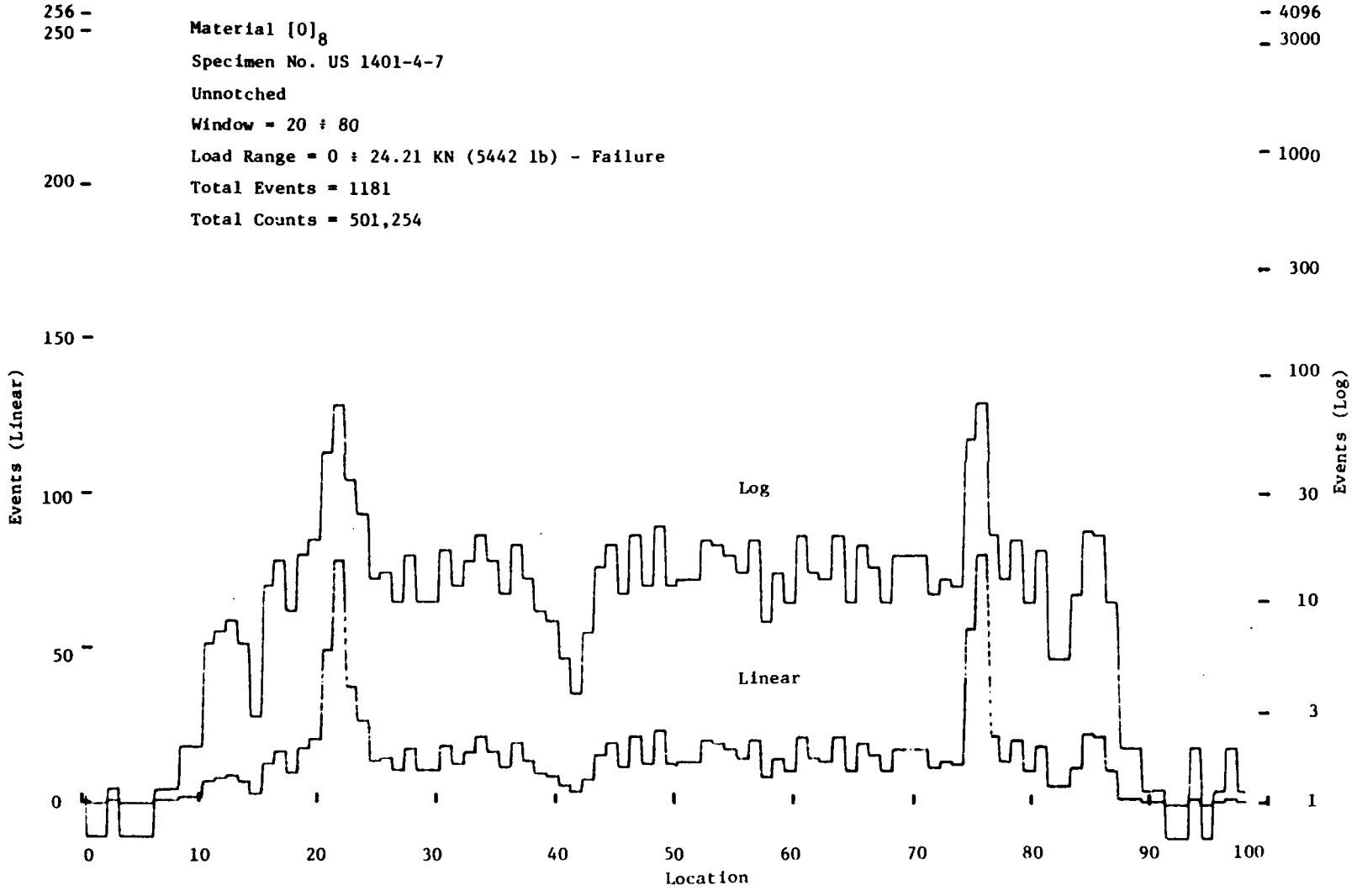


Figure 39. Location distribution histograms (in linear and logarithmic scales) for unnotched unidirectional 5.6 mil B/Al-6061F specimen after failure.

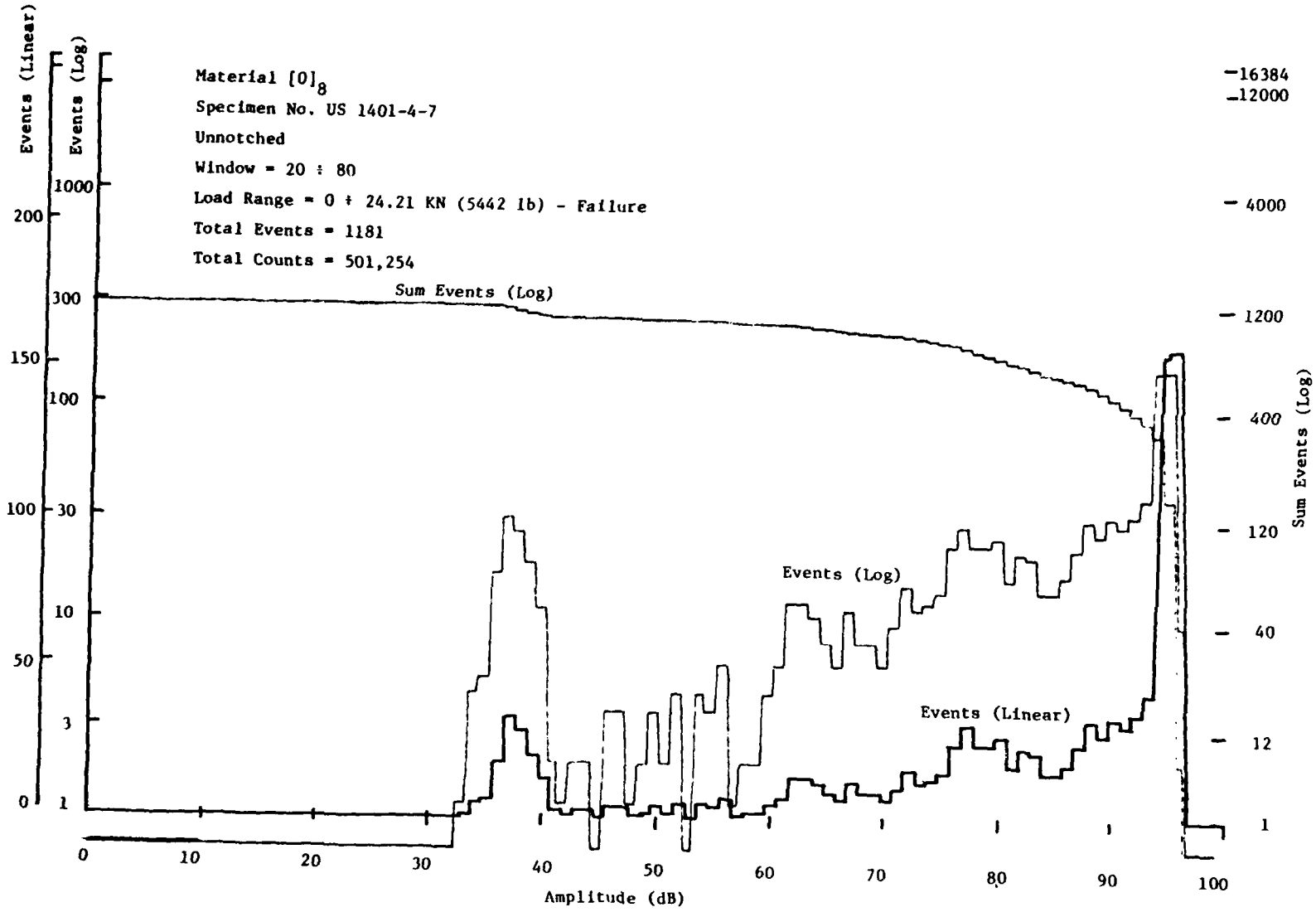


Figure 40. Amplitude distribution histograms (in linear and logarithmic scales) and Cumulative Event Amplitude Distribution for unnotched unidirectional 5.6 mil B/Al-6061F specimen after failure.

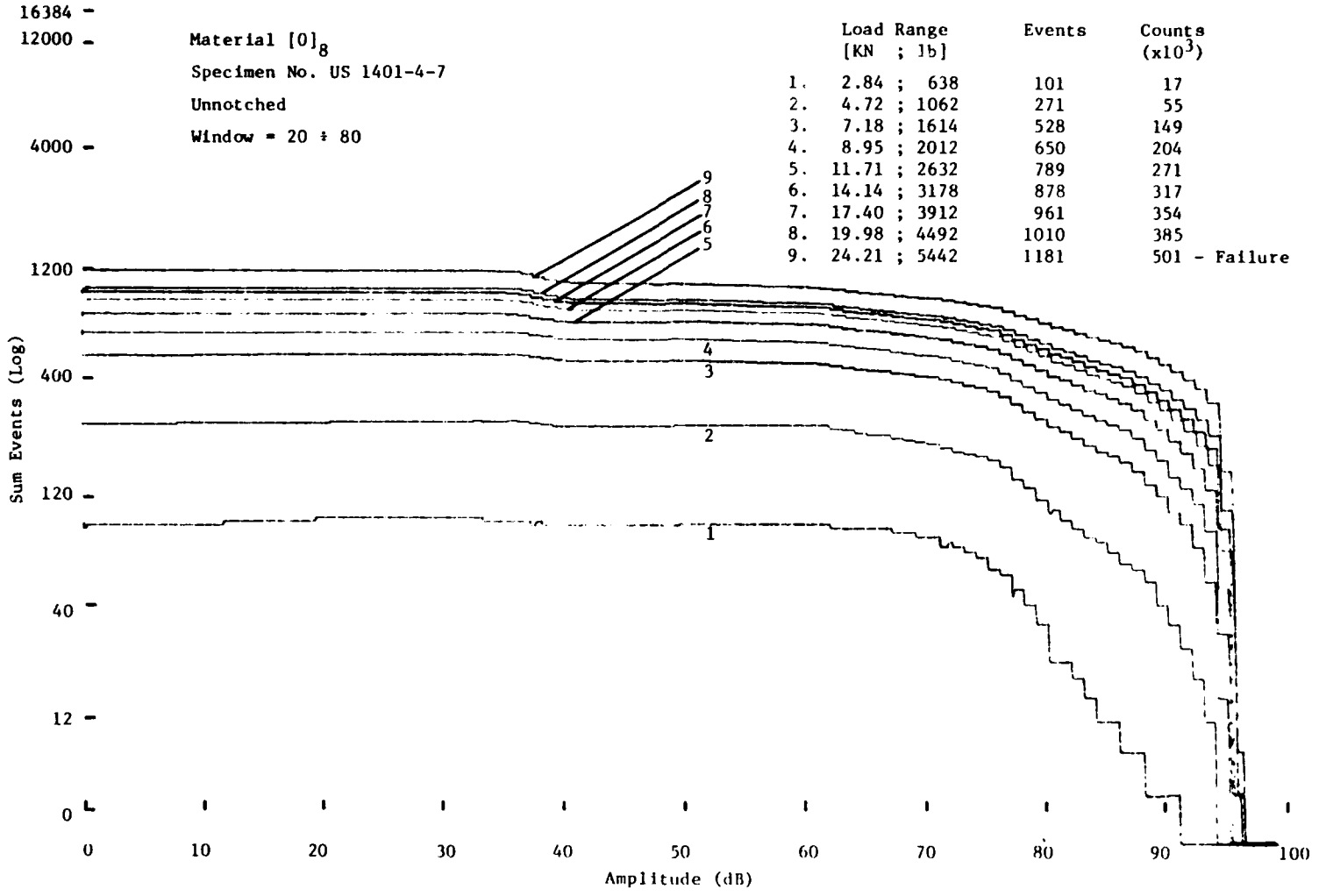


Figure 41. Cumulative Event Amplitude Distribution for unnotched unidirectional 5.6 mil B/Al-6061F specimen at various load levels.

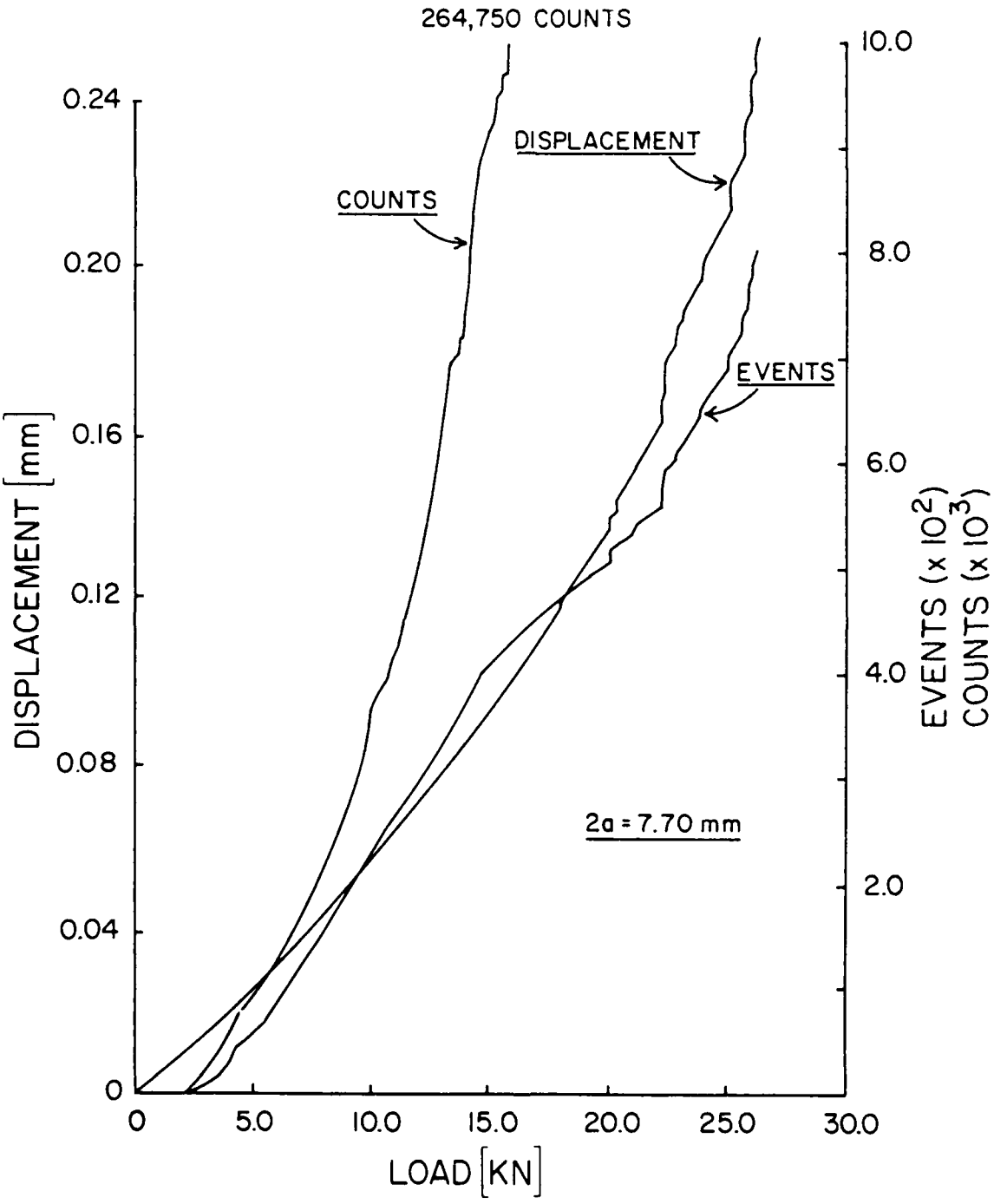


Figure 42. Far-field load-displacement curve and accumulative events and counts as a function of load for notched unidirectional 5.6 mil B/Al-6061F specimen (crack length = 7.70 mm).

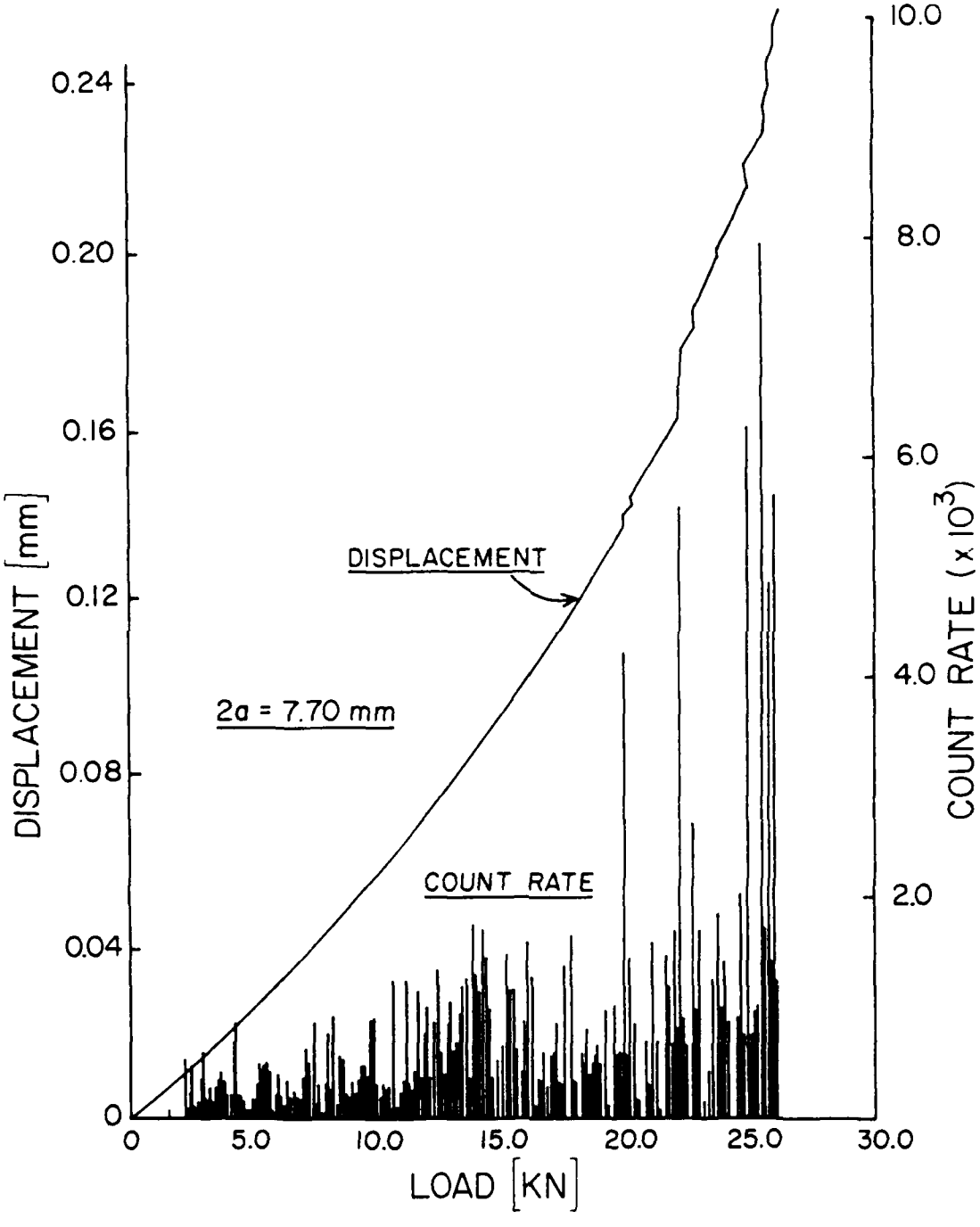


Figure 43. Far-field load-displacement curve and count rate (per 1.0 second) as a function of load for notched unidirectional B/Al-6061F specimen (crack length = 7.70 mm).

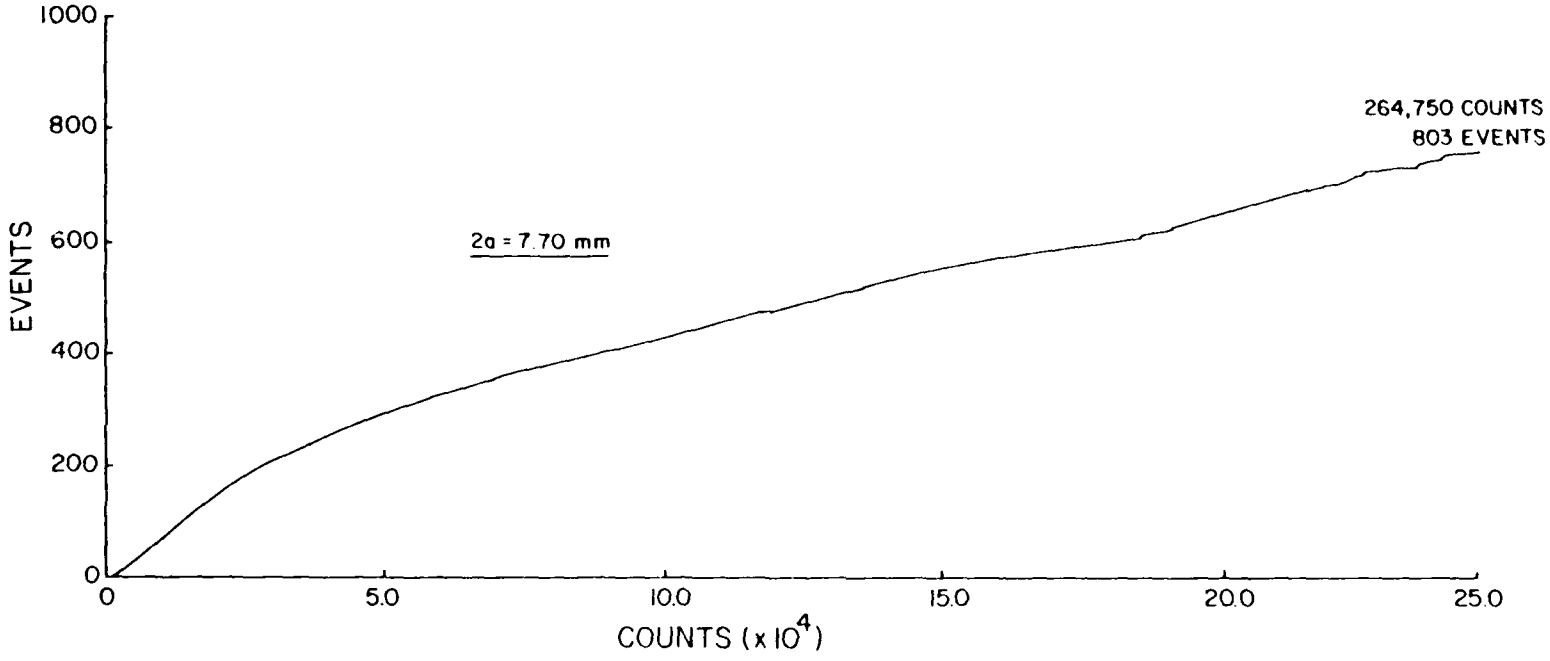


Figure 44. Accumulative counts per events for notched unidirectional 5.6 mil B/Al-6061F (crack length = 7.70 mm).

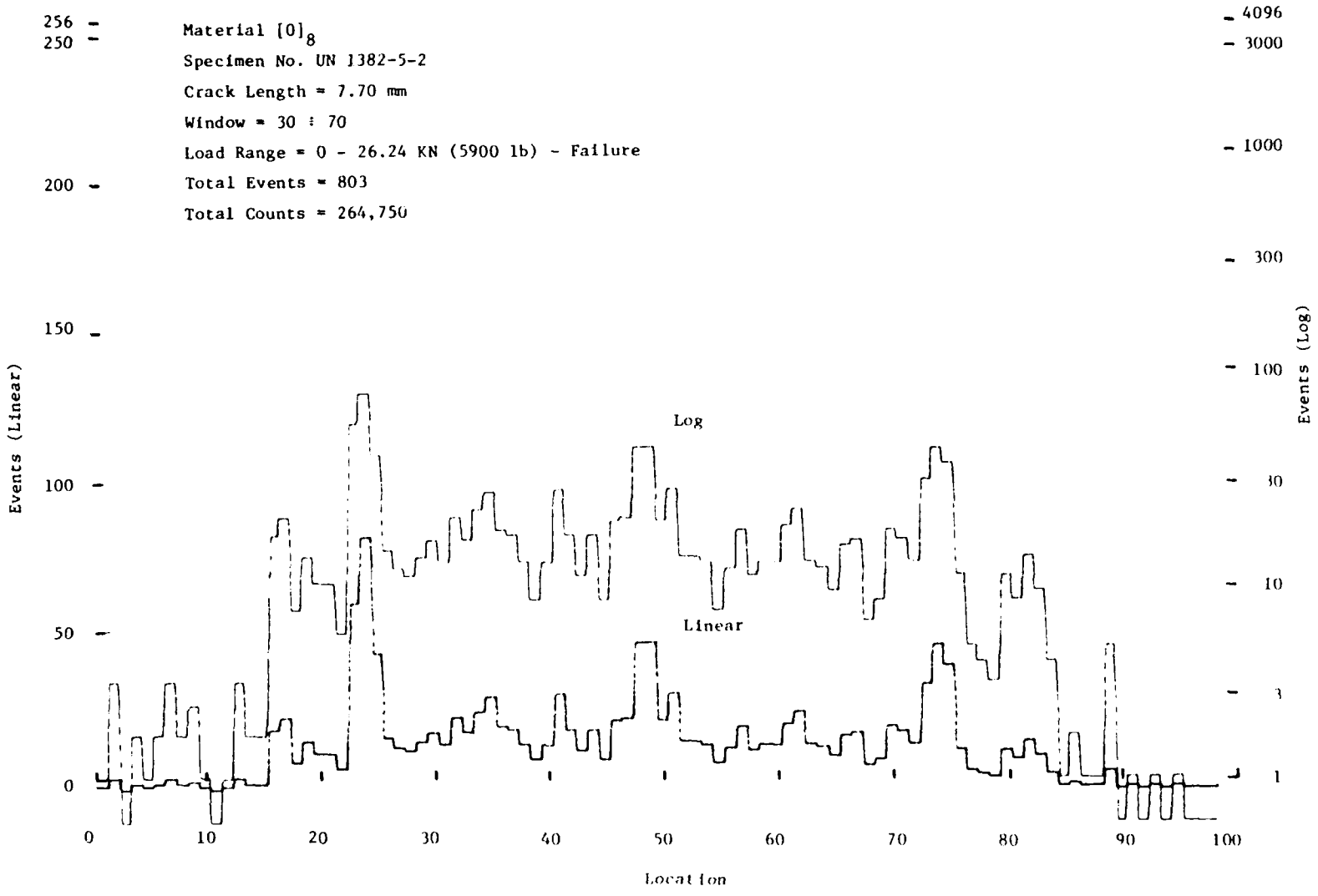


Figure 45. Location distribution histograms (in linear and logarithmic scales) for notched unidirectional 5.6 mil B/Al-6061F specimen after failure (crack length = 7.70 mm).

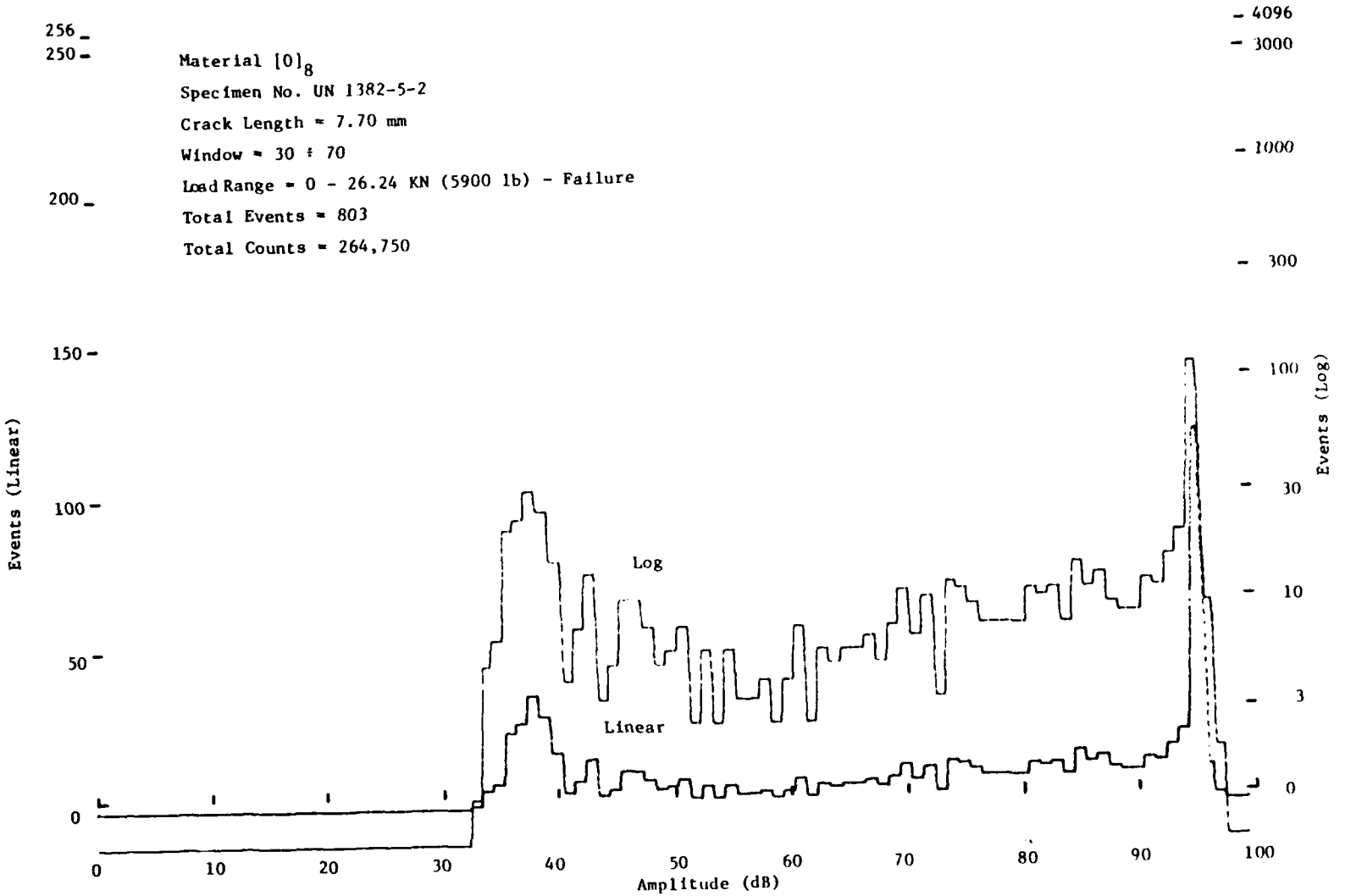


Figure 46. Amplitude distribution histograms (in linear and logarithmic scales) for notched unidirectional 5.6 mil B/Al-6061F specimen after failure (crack length = 7.70 mm).

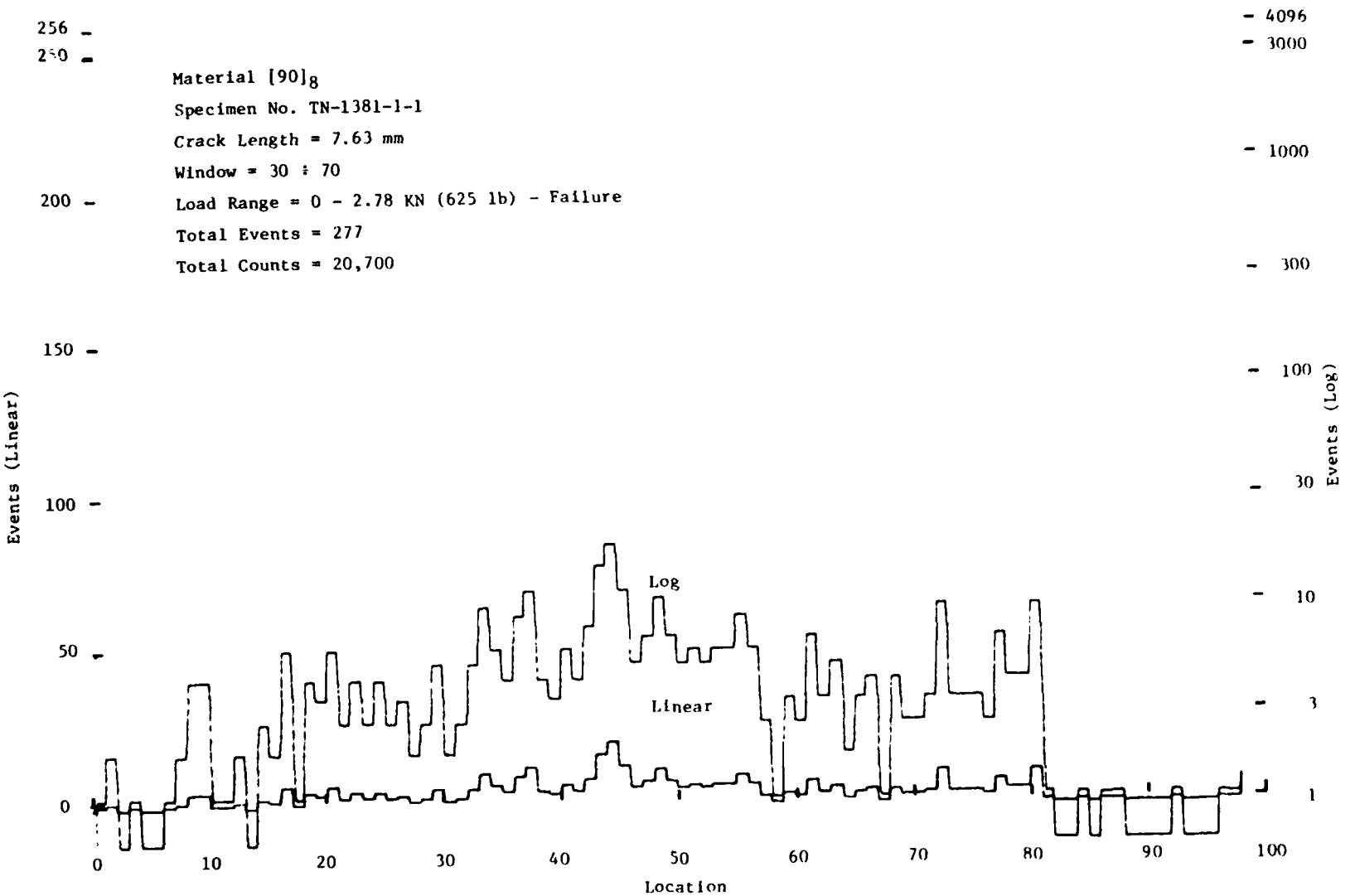


Figure 47. Location distribution histograms (in linear and logarithmic scales) for notched $[90]_8$ 5.6 mil B/Al-6061F specimens after failure (crack length = 7.63 mm).

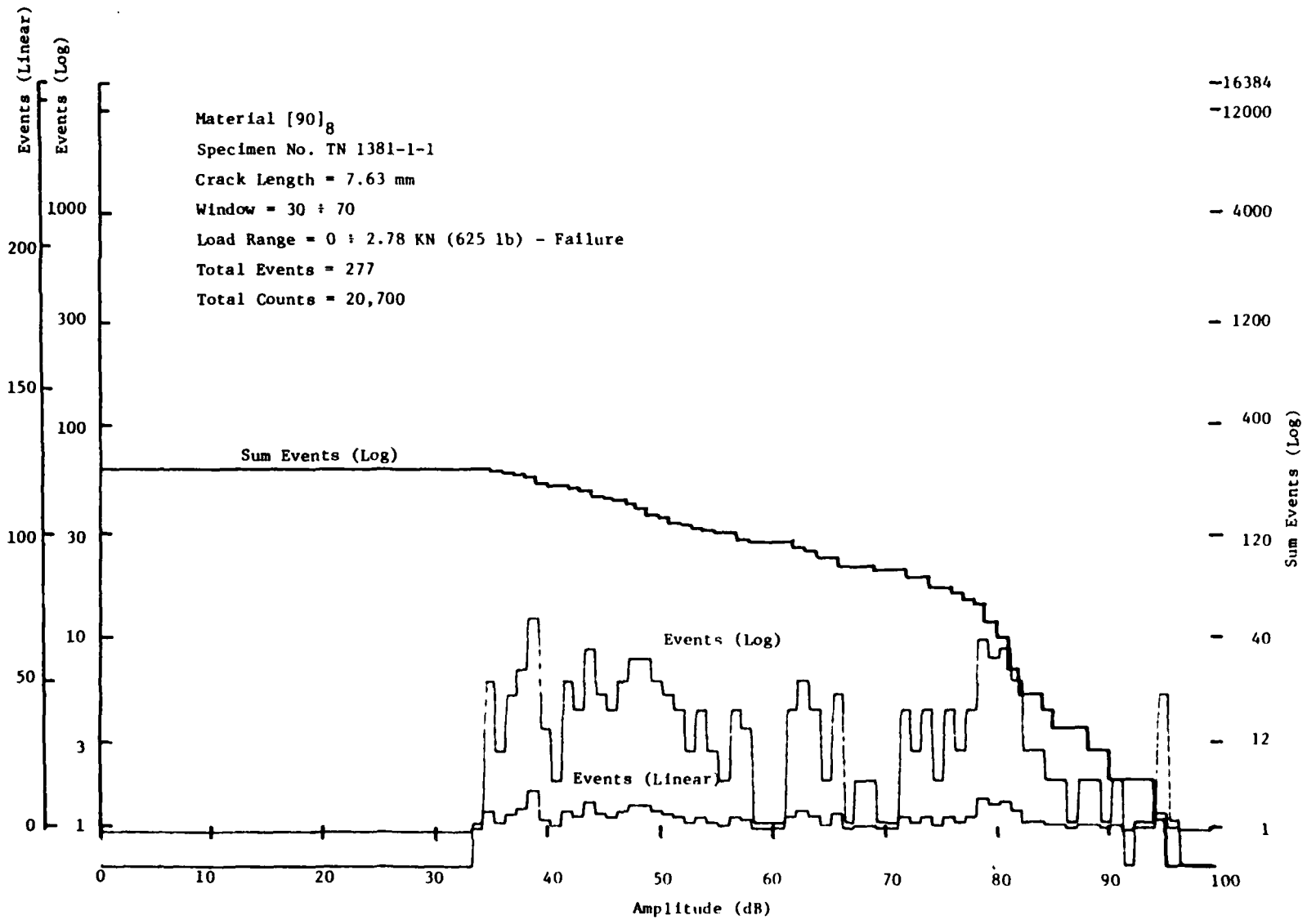


Figure 48. Amplitude distribution histograms (in linear and logarithmic scales) and Cumulative Event Amplitude Distribution for notched [90]8 5.6 mil B/Al-6061F specimens after failure (crack length = 7.63 mm).

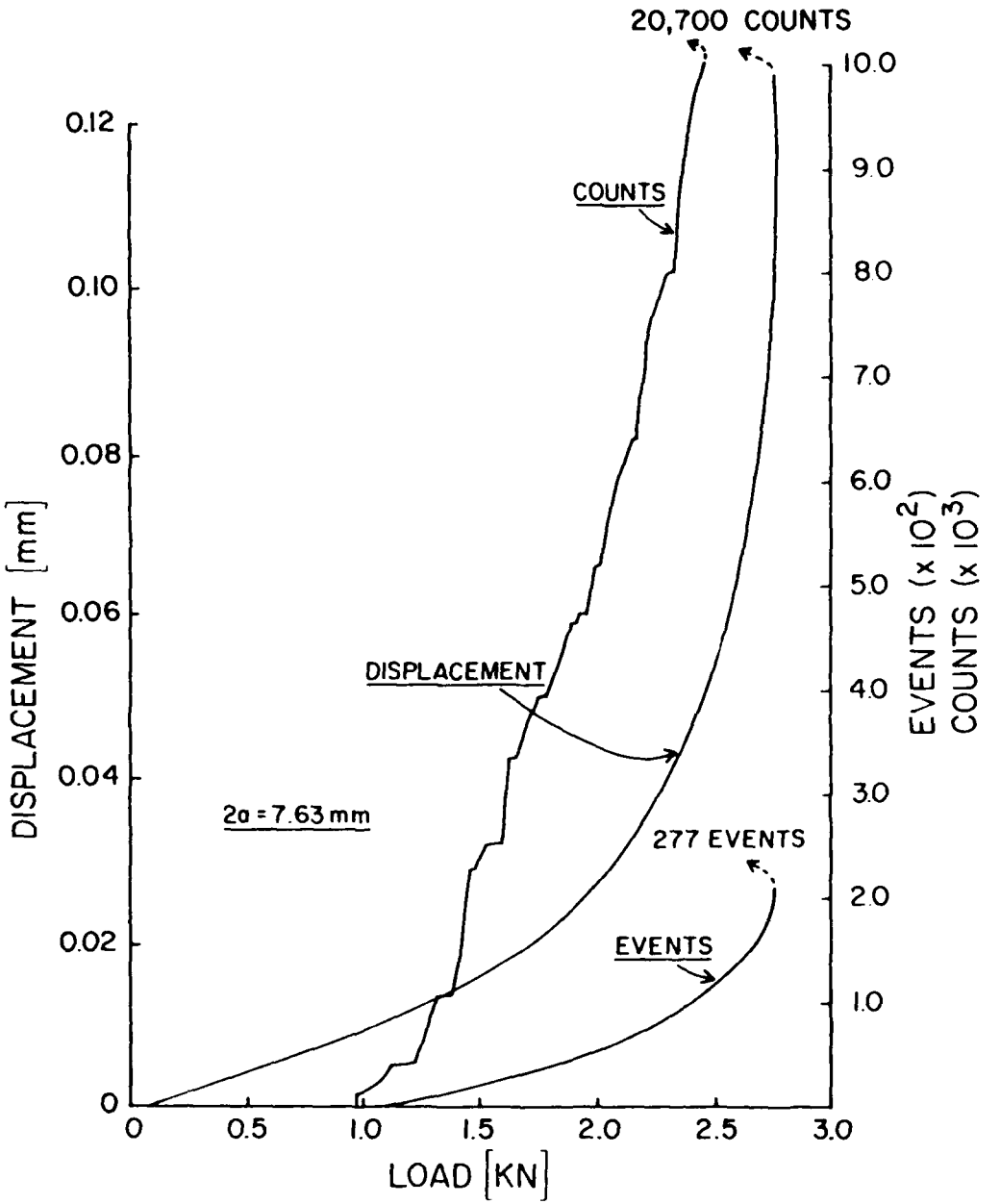


Figure 49. Far-field load-displacement curve and accumulative events and counts as a function of load for notched $[90]_8$ 5.6 mil B/Al-6061F specimen (crack length = 7.63 mm).

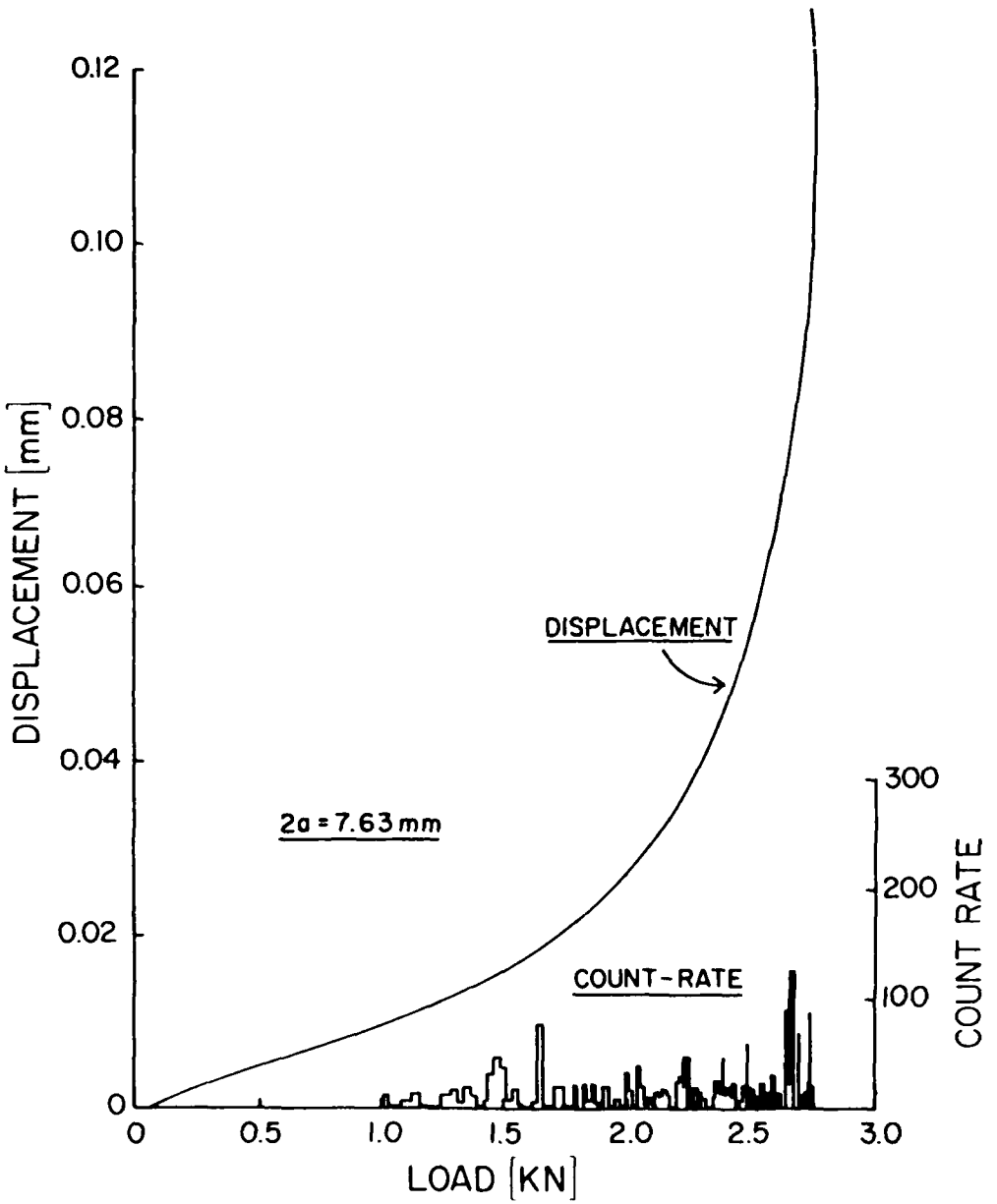


Figure 50. Far-field load-displacement curve and count rate (per 1.0 second) as a function of load for notched $[90]_8$ 5.6 mil B/Al-6061F specimen (crack length = 7.63 mm).

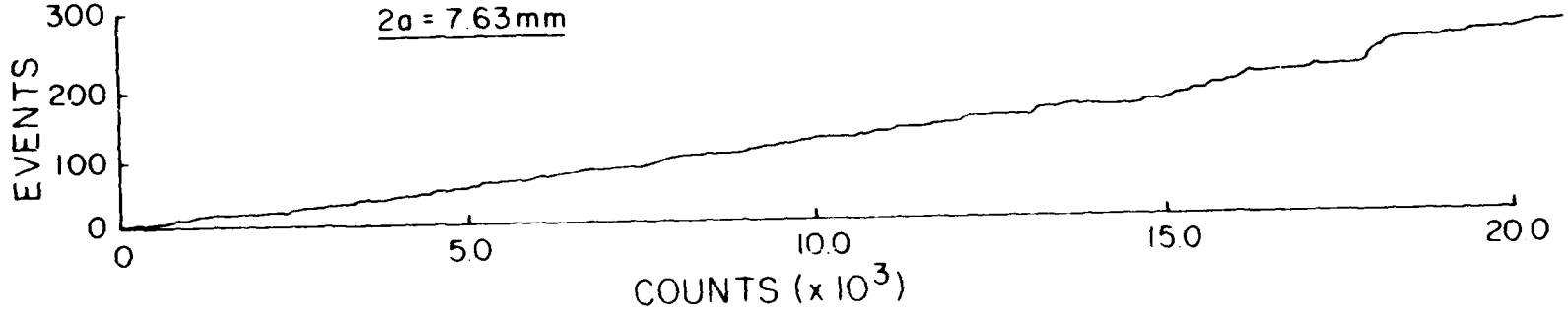


Figure 51. Accumulative counts per events for notched $[90]_8$ 5.6 mil B/Al-6061F specimen (crack length = 7.63 mm).

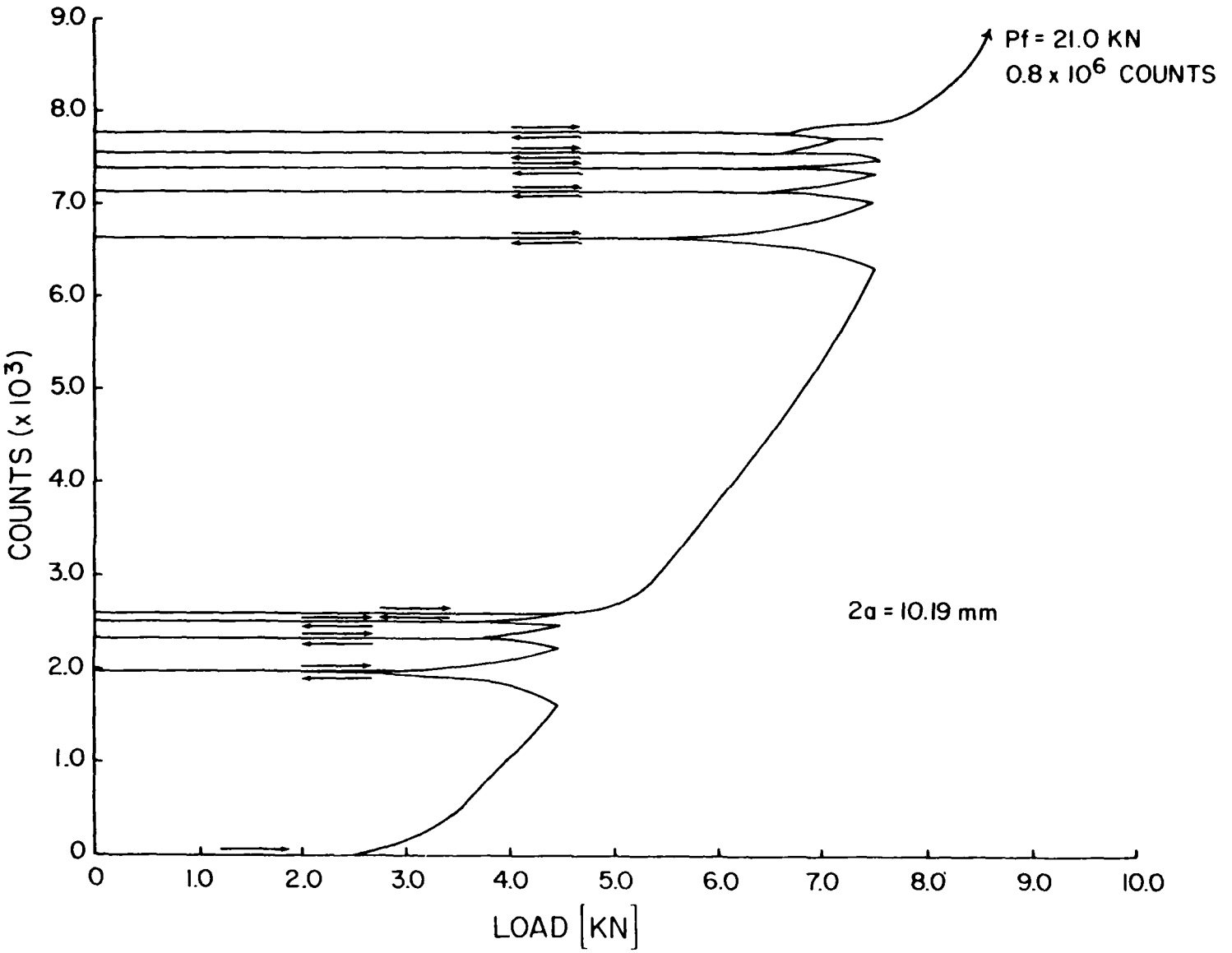


Figure 52. Accumulative counts as a function of load during loading/unloading cycles for unidirectional 5.6 mil B/Al-6061F (crack length =10.19 mm).

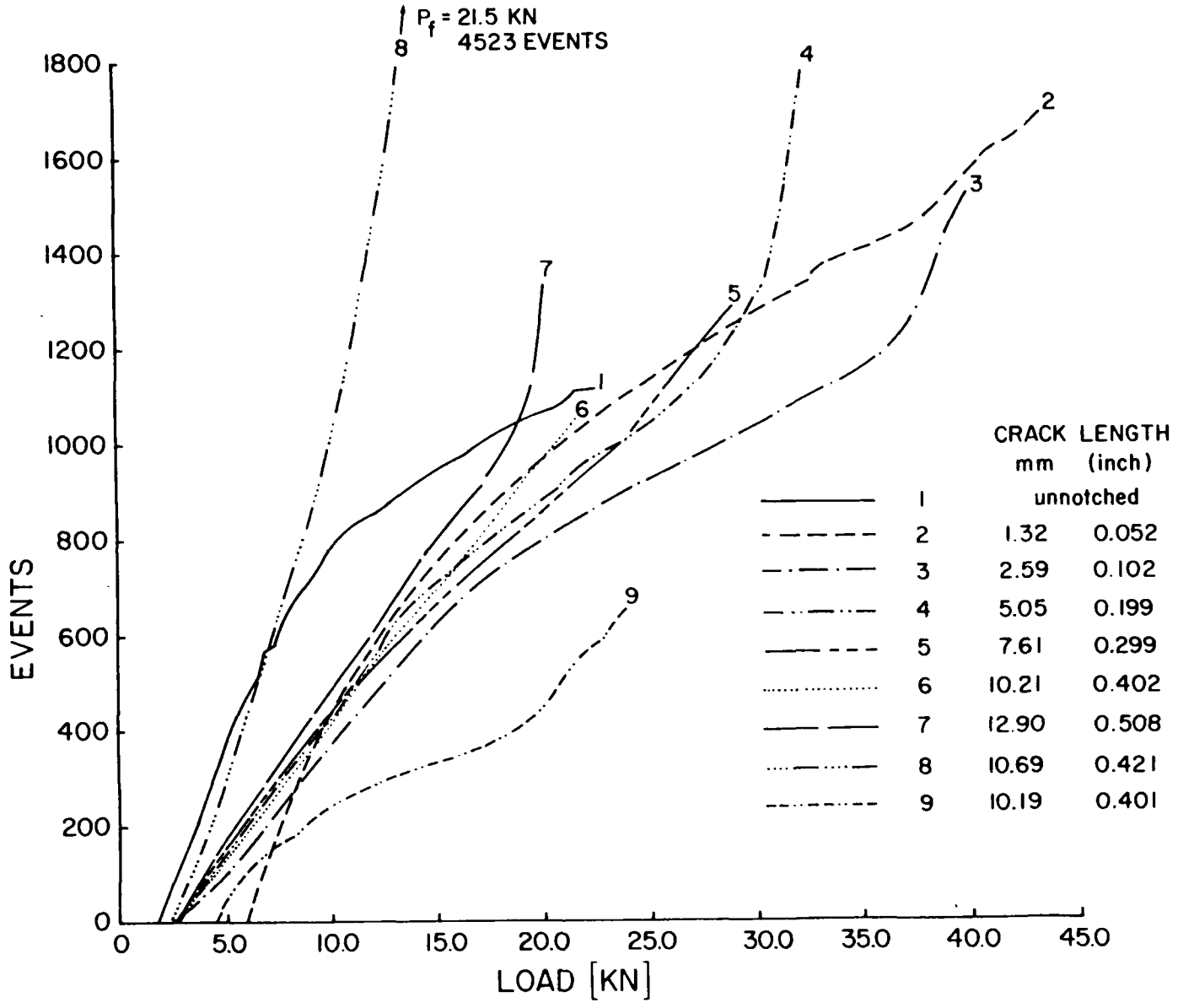


Figure 53. Accumulative number of events as a function of load for unnotched and notched unidirectional 5.6 mil B/Al-6061F specimens. Effect of clamping method and length of pre-set "window" is also shown.

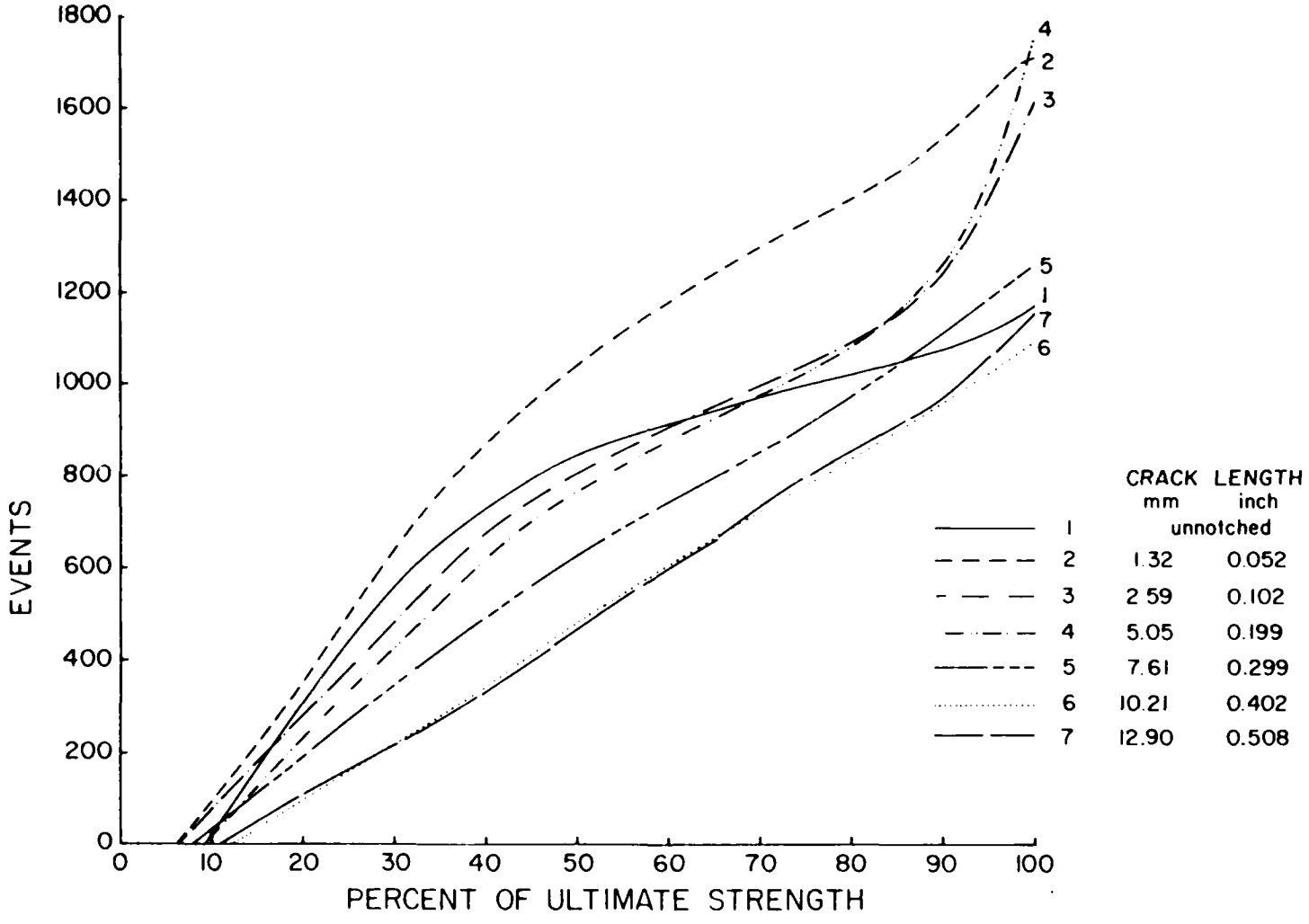


Figure 54. Accumulative number of events as a function of percent of ultimate strength for notched and unnotched unidirectional 5.6 mil B/Al-6061F specimens.

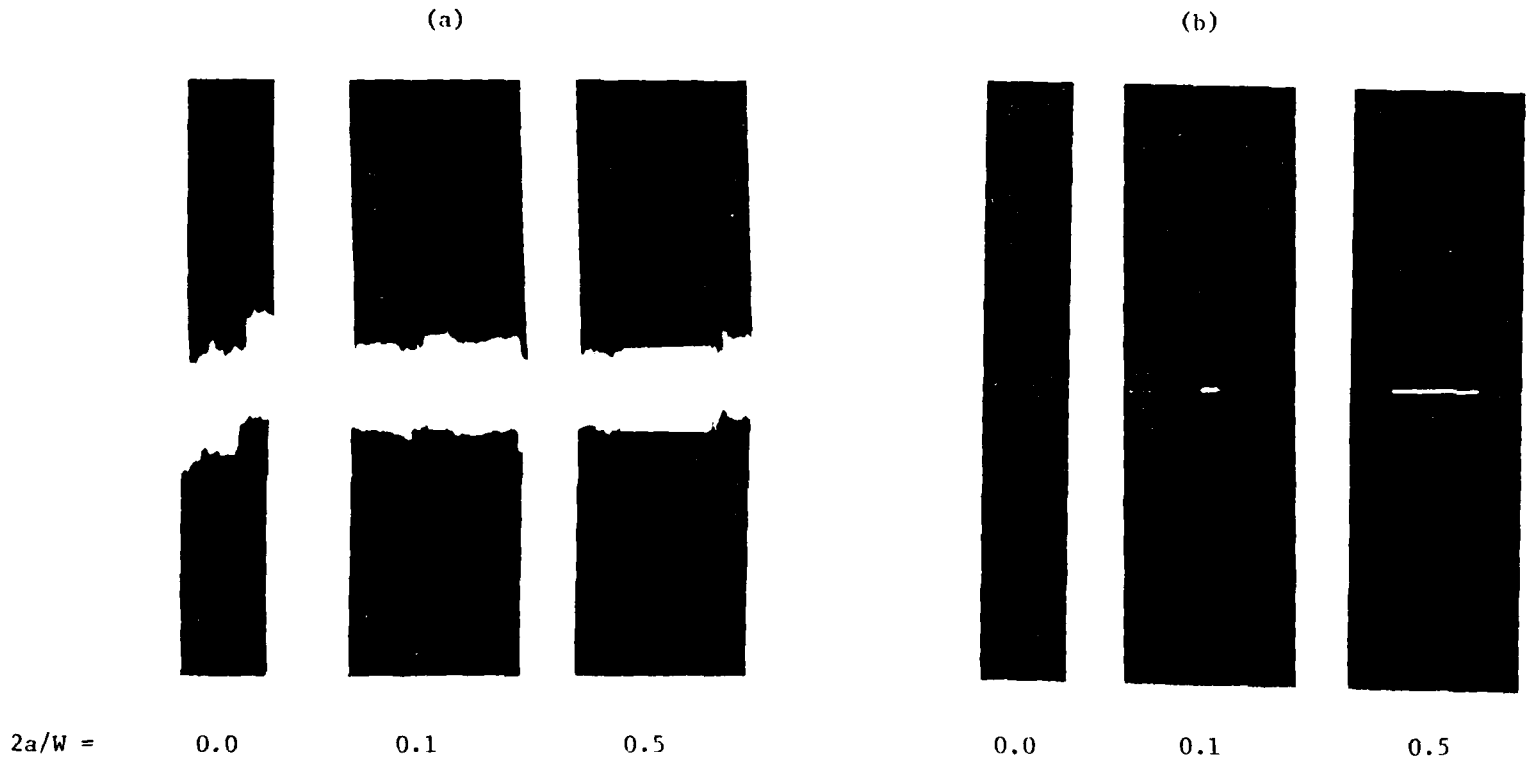


Figure 55. Photographs of fracture specimens for: a. $[0]_8$ and b. $[90]_8$ notched and unnotched specimens.

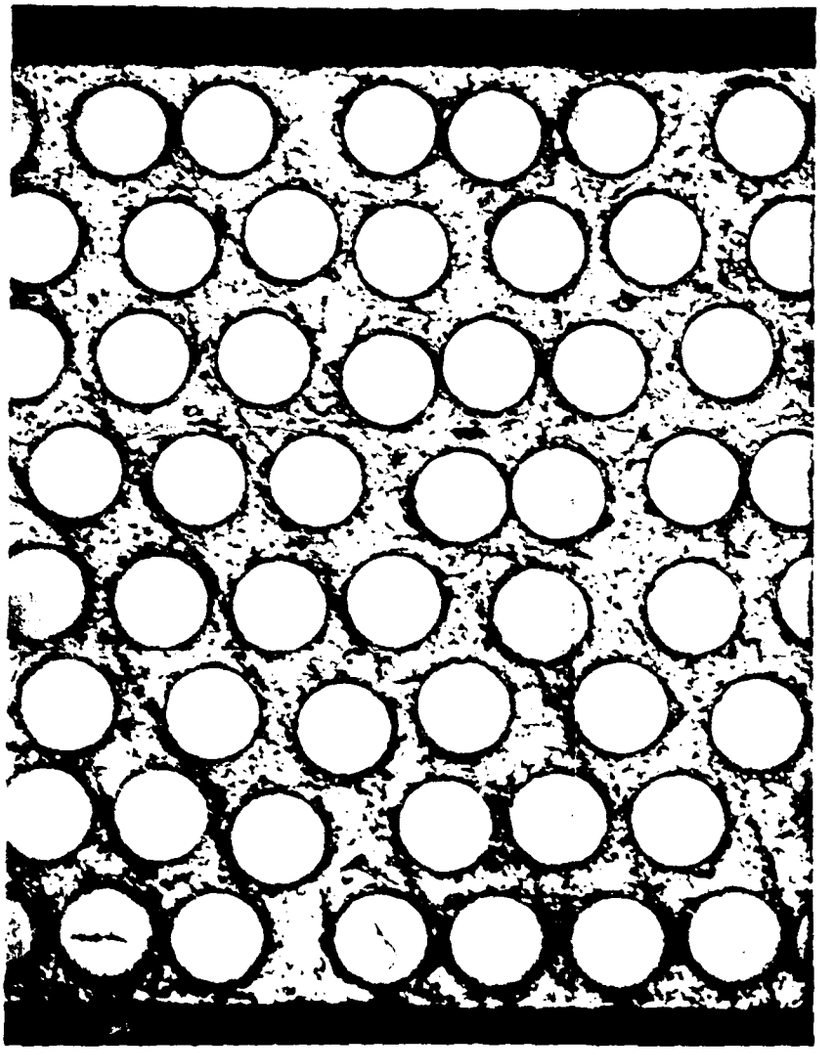

100X

Figure 56. Photomicrographs of unidirectional 5.6 mil B/Al-6061F specimen.

(a)

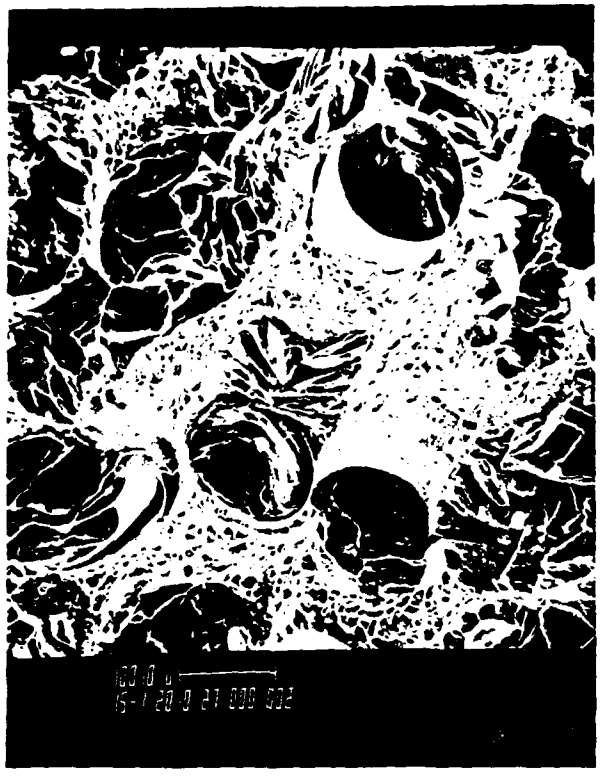

LEFT 150X

RIGHT 150X

(b)

30X

Figure 57. Scanning electron microscope micrographs of fracture surface. a. A stereo pair; b. General view of part of the fracture surface. (Ultimate strength = 1303 MPa.)

(a)

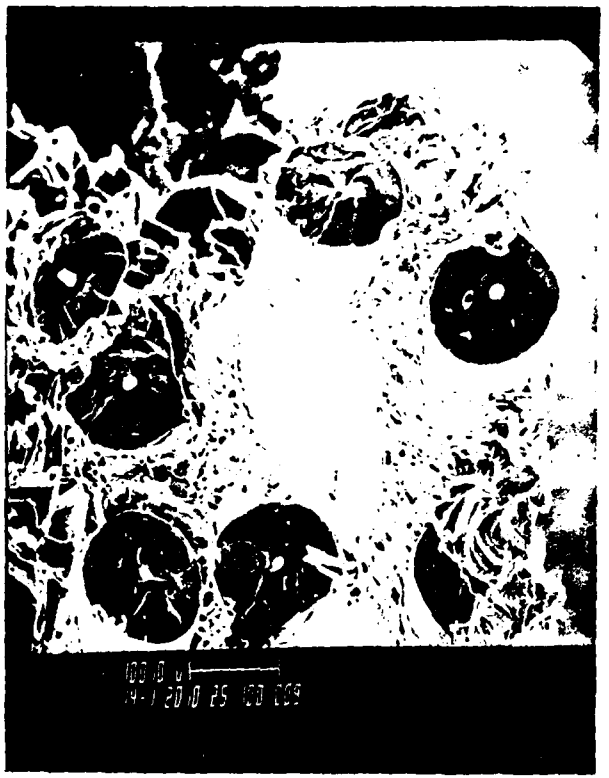

140X

(b)

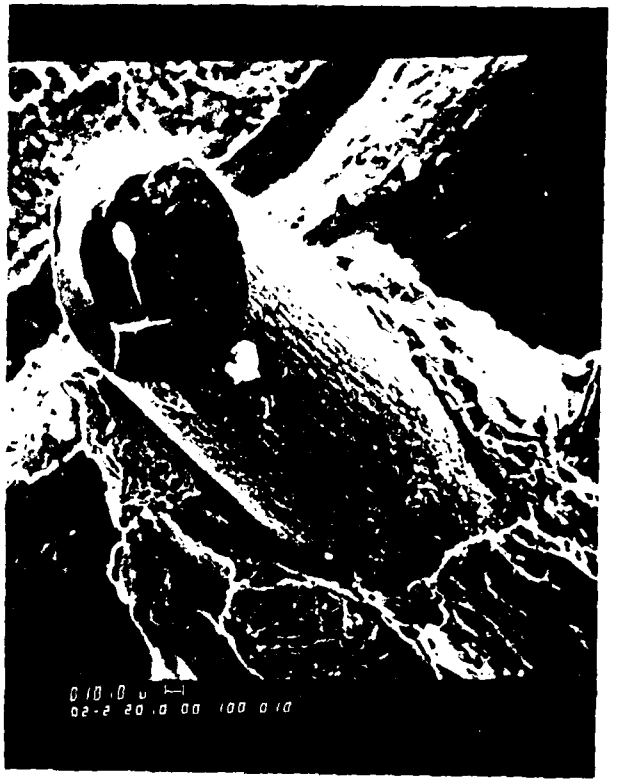

200X

Figure 58. Scanning electron microscope micrographs of fracture surface: a. General View; b. Individual fiber for X-ray examination of fiber surface. (Ultimate strength = 1469 MPa.)

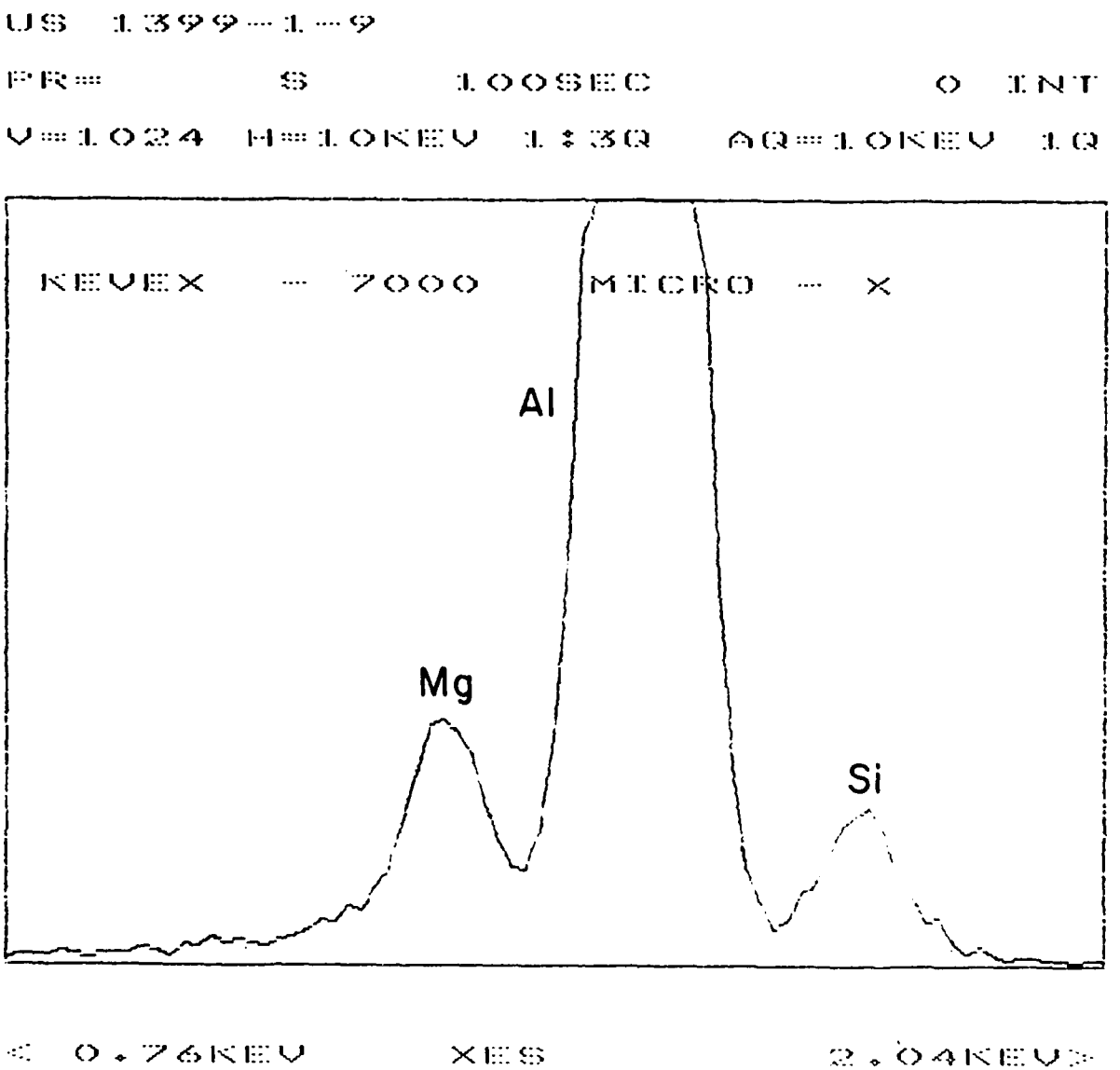


Figure 59. X-ray examination of fiber surface shown in Figure 58b using an energy dispersive X-ray analyzer on the SEM.

(a)

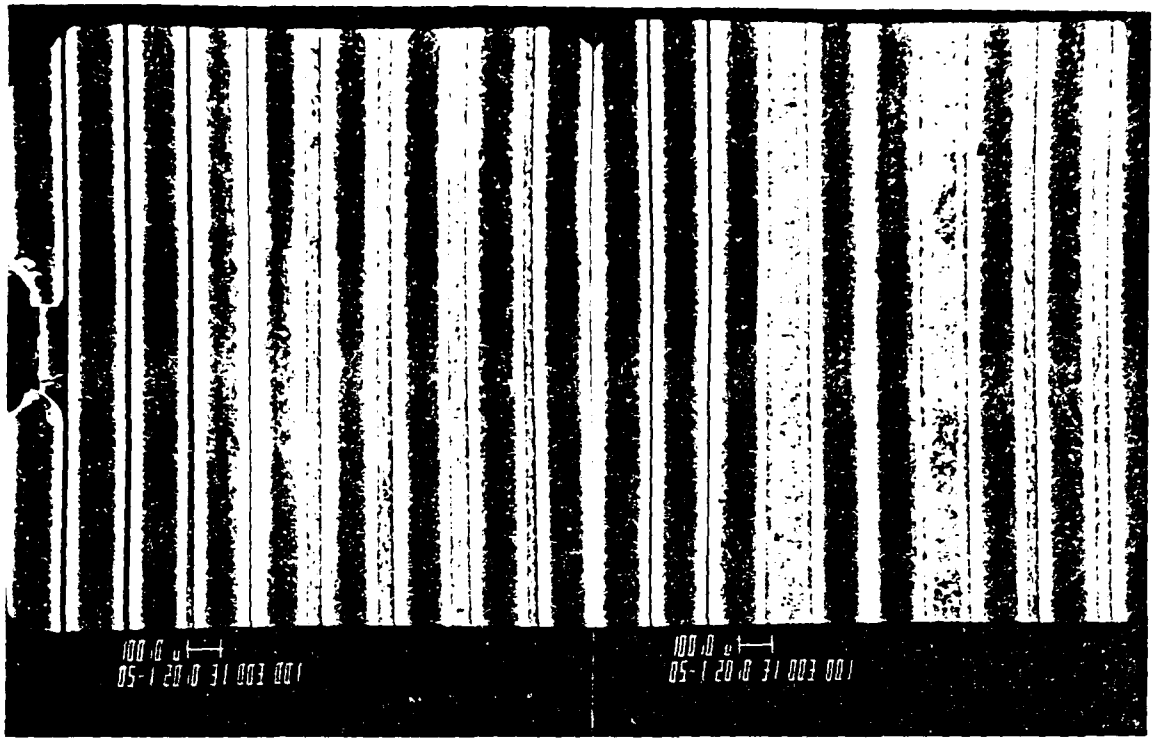

50X

(b)

200X

Figure 60. Crack tip damage in unnotched unidirectional 5.6 mil B/Al-6061F specimen after loading to 40% of expected ultimate load (crack length = 7.64 mm). a. General view; b. Detail of crack tip damage.

(a)

100X

(b)

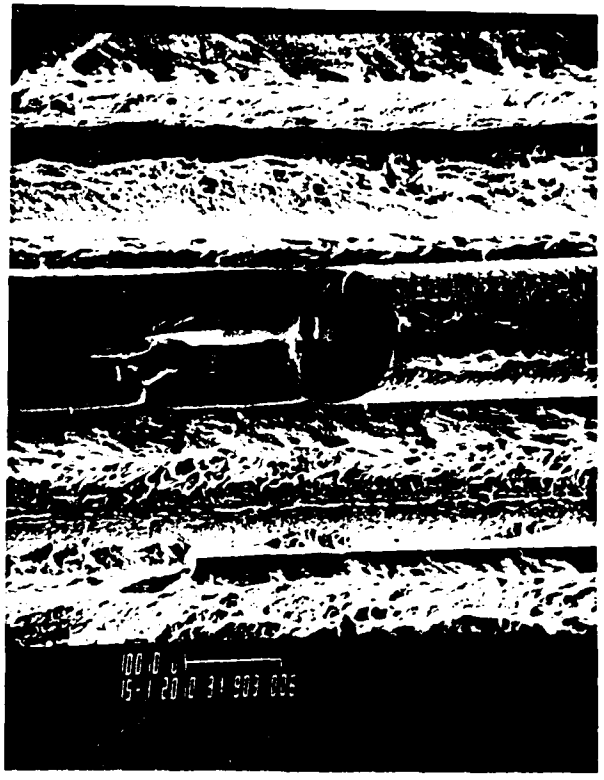

150X

Figure 61. Scanning electron microscope micrographs of fracture surface of $[90]_8$ 5.6 mil B/Al-6061F. a. Unnotched specimen; b. Notched specimen (crack length = 7.62 mm).

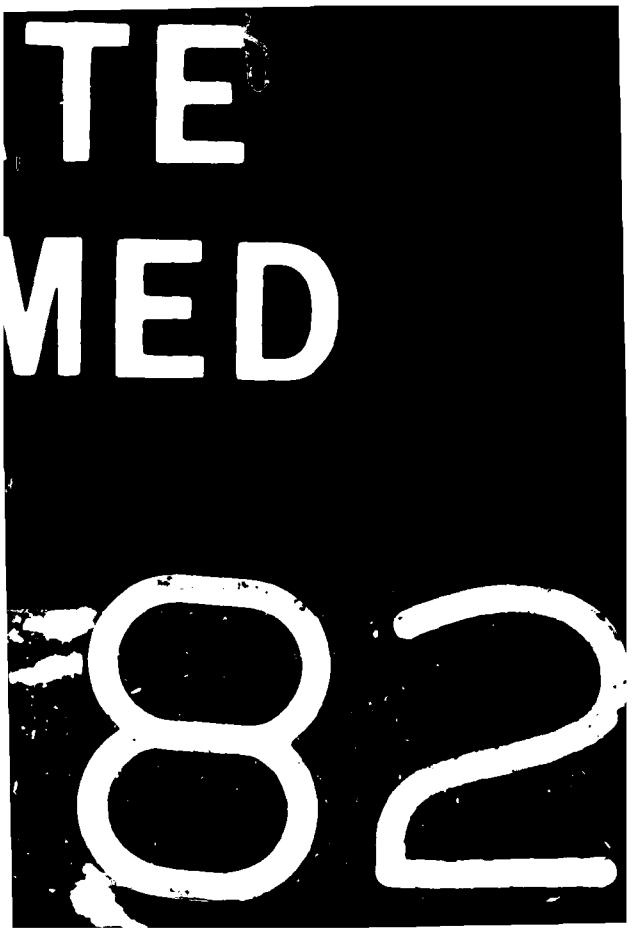
TE
MED
82